The Nature and Variability of Eddy Kinetic Energy in an Ocean General Circulation Model

With a Focus on the South Pacific Subtropical Gyre and the Labrador Sea

Dissertation
zur Erlangung des Doktorgrades
der Mathematisch-Naturwissenschaftlichen Fakultät
der Christian-Albrechts-Universität zu Kiel

vorgelegt von

Jan Klaus Rieck

Kiel, 2019

Referent: Prof. Dr. Claus W. Böning

Koreferent: Prof. Dr. Peter Brandt

Tag der mündlichen Prüfung: 05.03.2019

Zum Druck genehmigt: 05.03.2019

gez. Prof. Dr. Frank Kempken, Dekan

Abstract

This thesis focuses on the nature of oceanic Eddy Kinetic Energy (EKE), its generation and temporal variability. For case studies, two regions of the world's oceans are selected based on their importance for the global ocean circulation, the local occurrence of mesoscale variability, and the level of atmospherically driven oceanic variations. The first region is located in the subtropical gyre in the South Pacific, and the second region is focused on the Labrador Sea (LS) in the western subpolar North Atlantic. An Ocean General Circulation Model (OGCM) based on the NEMO code builds the foundation for these investigations. The model's ability to simulate the oceanic mesoscale in a configuration with $1/4^\circ$ horizontal resolution is tested by reducing the horizontal diffusion of momentum. The reduction substantially improves the representation of EKE and its variations in the South Pacific subtropical gyre without exhibiting excessive amounts of grid-scale numerical noise.

For a first case study, several simulations of the $1/4^\circ$ configuration with varying atmospheric forcing are used to investigate the temporal variability of EKE in the South Pacific Subtropical Countercurrent (STCC). Decadal changes in wind stress curl associated with positive (negative) phases of the Interdecadal Pacific Oscillation (IPO) lead to upwelling (downwelling) south of the STCC and downwelling (upwelling) in the STCC, strengthening (weakening) the meridional density gradient and thereby increasing (decreasing) STCC strength, baroclinic instability and the resulting EKE. An additional 30 to 40% of the local density anomalies can be explained by long baroclinic Rossby waves propagating into the region, modulating the decadal signal of the IPO's influence in the STCC on interannual time scales.

In a second case study, the model's horizontal resolution is regionally increased to $1/20^\circ$ in the North Atlantic to investigate different types of mesoscale eddies in the Labrador Sea. Irminger Rings (IR), Convective Eddies (CE) and Boundary Current Eddies (BCE), their generation mechanisms, and their impact on the central LS are successfully simulated. On decadal time scales, the temporal variability of EKE in the LS is driven by the large-scale atmospheric circulation. In the case of CE, local winter heat loss leads to deep convection, a baroclinically unstable rim-current is established along the edge of the convection area and generates EKE at mid-depth. The variations of EKE associated with the surface intensified IR and BCE are driven by the large-scale changes of the currents of the subpolar gyre. While IR play a vital role in stratifying large parts of the LS and thus suppressing deep convection, CE are the major driver of rapid restratification during and after deep convection.

Overall, the thesis shows that, with a suitable choice of parameters, the OGCM offers the required temporal and spatial resolution and extent to investigate the long-term variations of the mesoscale beyond intrinsic time scales, successfully simulating EKE, its generation, impacts and temporal variability.

Zusammenfassung

Diese Arbeit untersucht die kinetische Energie von mesoskaligen, ozeanischen Strömungen (EKE), ihre Entstehung, und zeitliche Variabilität. Basierend auf ihrer Relevanz für die globale Ozeanzirkulation, das lokale Auftreten von mesoskaliger Variabilität, und der Stärke von atmosphärisch angetriebenen Veränderungen im Ozean werden zwei Regionen der ausgewählt. Eine Region liegt im subtropischen Wirbel im Südpazifik, die zweite in der Labradorsee (LS) im westlichen subpolaren Nordatlantik. Ein Ozeanzirkulationsmodell basierend auf dem NEMO-Code bildet den Grundstein für die Studie. Die Fähigkeit des Modells die ozeanische Mesoskala in einer Konfiguration mit 1/4° horizontaler Auflösung zu simulieren wird durch eine Reduktion der horizontalen Diffusion von Momentum überprüft. Die Reduktion verbessert die Darstellung der EKE und ihrer Veränderungen im südpazifischen subtropischen Wirbel, ohne dabei übermäßig viel numerisches Rauschen auf der Gitterskala zu produzieren.

Für eine erste Fallstudie werden verschiedene Simulationen der 1/4°-Konfiguration mit unterschiedlichem atmosphärischem Antrieb genutzt, um die zeitliche Variabilität der EKE im südpazifischen subtropischen Gegenstrom (STCC) zu untersuchen. Dekadische Schwankungen der Rotation der Windschubspannung, hervorgerufen durch positive (negative) Phasen der Interdekadischen Pazifischen Oszillation (IPO), führen zu Auftrieb (Absinken) südlich des STCC und Absinken (Auftrieb) im STCC und einer Stärkung (Abschwächung) des meridionalen Dichtegradienten. Dadurch erhöhen (reduzieren) sie die Stärke des STCC, barokline Instabilität, und die resultierende EKE. Zusätzlich können 30 bis 40% der lokalen Dichteanomalien durch lange, barokline Rossbywellen erklärt werden, die in der Region eintreffen und das dekadische Signal des Einflusses der IPO auf interannualen Zeitskalen modulieren.

In einer zweiten Fallstudie wird die horizontale Auflösung des Modells im Nordatlantik auf 1/20° erhöht um die verschiedenen Arten von mesoskaligen Strömungswirbeln in der Labradorsee zu untersuchen. Irminger Ringe (IR), Konvektive Wirbel (CE) und Randstromwirbel (BCE), ihre Entstehungsmechanismen und ihr Einfluss auf die zentrale LS werden erfolgreich simuliert. Auf dekadischen Zeitskalen wird die zeitliche Variabilität der EKE in der LS von der großskaligen Zirkulation der Atmosphäre angetrieben. Im Falle der CE führt lokaler Wärmeverlust im Winter zu Tiefenkonvektion, eine baroklin instabile Strömung entlang des Randes der Konvektionsregion entsteht und produziert EKE in mittleren Tiefen. Die Veränderungen der EKE, die den oberflächenintensivierten IR und BCE zuzuordnen ist, werden durch großskalige Schwankungen der Strömungen im subpolaren Wirbel verursacht. Während die IR eine essentielle Rolle in der Stärkung der Schichtung von großen Teilen der LS spielen und somit die Tiefenkonvektion erschweren, sind die CE der hauptsächliche Grund für die schnelle Wiederherstellung der Schichtung während und nach der Tiefenkonvektion.

Insgesamt zeigt diese Arbeit, dass das Ozeanzirkulationsmodell in Verbindung mit einer angemessenen Wahl der Parameter die erforderliche zeitliche und räumliche Auflösung und Ausdehnung bietet, um die langzeitlichen Schwankungen der ozeanischen Mesoskala über intrinsische Zeitskalen hinaus zu untersuchen und die EKE, ihre Entstehung, ihren Einfluss und ihre zeitliche Variabilität erfolgreich zu simulieren.

Contents

1 Introduction

1.1 The Nature of Eddy Kinetic Energy

Historic descriptions of the oceans' circulation assumed the flow to be rather laminar. Currents and their velocities were estimated based on the geostrophic relationship due to the limited availability of direct current measurements. With the introduction of more sophisticated measurement techniques it became clear however, that most regions of the ocean exhibit an abundance of smaller scale circulation features (cf. Fig. 1.1). These mesoscale currents have spatial scales of tens to hundreds of kilometers and temporal scales of weeks to months (Stammer and Böning 1996). While the traditional ship-based observations of temperature, salinity and velocities revealed more and more details of the mesoscale (e.g. MODE Group 1978), it was hardly possible to quantitatively describe its spatial and temporal distribution in all ocean basins. Only the advance of satellite altimetry made it feasible to directly observe and describe the mesoscale in detail on a global scale (Fu 1983; Le Traon and Morrow 2001).

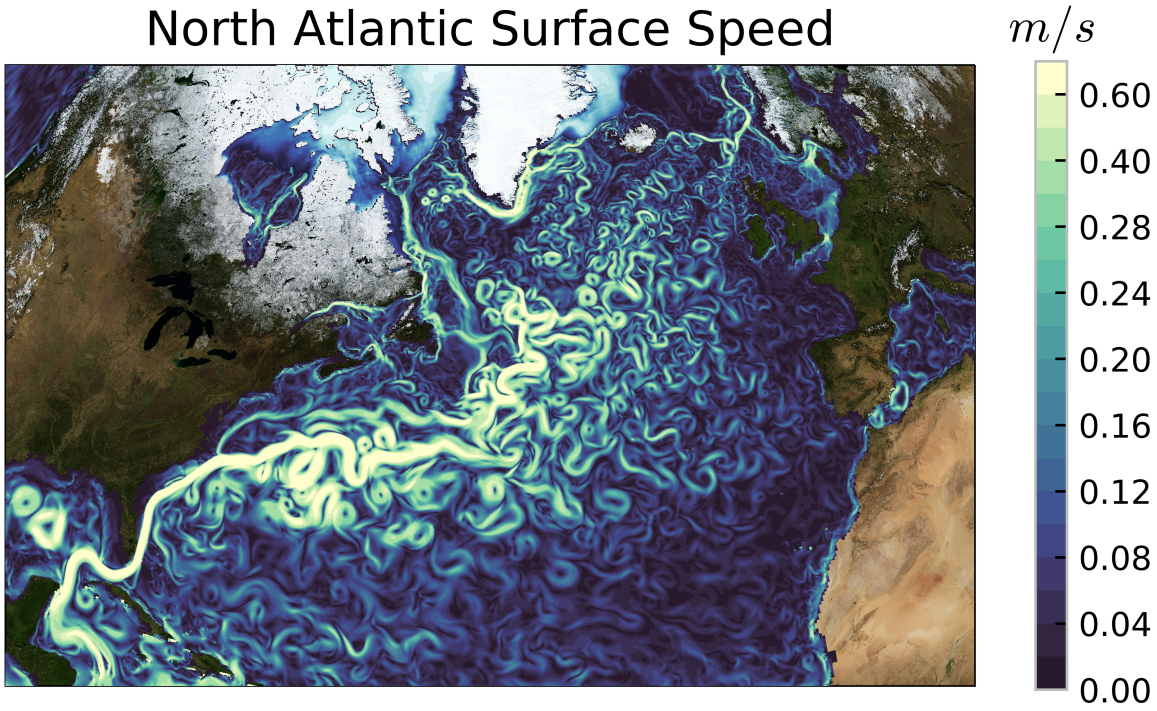

Figure 1.1: Snapshot (5-day mean field) of horizontal current speed at the sea surface in the North Atlantic from a 1/20° Ocean General Circulation Model (VIKING20X). Light blue to white shading in the northern regions indicates sea ice cover. The land surface image is obtained from NASA Earth Observatory (https://visibleearth.nasa.gov/view.php?id=73884).

Analogously to the observing systems, numerical modeling of the ocean significantly progressed in the second half of the 20th century. Due to improved numerical techniques and increased computational power, ocean simulations could be run at higher resolutions, effectively simulating the mesoscale (Holland and Lin 1975; Cox 1985; Smith et al. 2000). Until today, numerical models remain the most important tool to study the oceanic mesoscale. The information gleaned from satellite-borne observing techniques is limited to the ocean surface and although the number of observing platforms in the water column, ship-based and autonomous, has drastically increased, synoptic pictures of whole ocean basins are impossible to obtain at depth. This gap of knowledge is tried to be filled with the help of ocean general circulation models (OGCMs) in configurations that aim at simulating the oceans' circulation as realistically as possible. High resolution simulations (e.g. von Storch et al. 2012) and theoretical interpretations of observations (e.g. Scott and Wang 2005) reveal that baroclinic instability is the major generation mechanism of mesoscale variability. Baroclinic instability emerges when the horizontal density gradients in the ocean are large, thereby creating strong vertical gradients of the horizontal velocities through the thermal wind relation. The flow becomes unstable and a lateral exchange of properties reduces the horizontal gradients of density, essentially transferring energy from the reservoir of Available Potential Energy to Eddy Kinetic Energy (EKE). Another contribution to the generation of mesoscale currents, especially in strong large-scale current systems, is made by barotropic instability (e.g. Yang et al. 2017; Schubert et al. 2018) that arises when the horizontal gradients of velocity are large, and transfers kinetic energy from the mean flow (MKE) to the mesoscale EKE.

As the generation of mesoscale currents is closely associated with the transfer of energy to the reservoir of Eddy Kinetic Energy, EKE is the most commonly investigated property to study the temporal and spatial distributions of the oceanic mesoscale. Eddy Kinetic Energy describes the velocity manifestations of different mesoscale phenomena such as filamenting and meandering of currents and various forms of vortices and current rings. In general, EKE is large in the vicinity of strong currents such as the western boundary currents or the Antarctic Circumpolar Current, where the velocity gradients are strong (Scharffenberg and Stammer 2010; Xu et al. 2011). Nevertheless, EKE is present in all regions, as baroclinic instability can emerge from relatively weak velocity gradients (Beckmann et al. 1994; Arbic 2000; Spall 2000) and EKE in the form of waves or eddies propagates from its location of generation and could thus reach areas where instabilities are weak or not present (Fu 2009). In the vertical, EKE is most

often surface intensified, reflecting the dominance of the first baroclinic mode in wide areas of the ocean (Wunsch 1997). However, there are various instances where EKE has a maximum at depth, such as in Mode Water eddies (e.g. Schütte et al. 2016), Deep Western Boundary Current eddies (Dengler et al. 2004) or Convective Eddies (Lilly et al. 2003).

Studies of mesoscale variability and EKE not only help to dynamically understand how water flows in the ocean. Mesoscale eddies and EKE in general do also impact larger scale hydrographic and dynamic properties and are important for the whole climate system and its changes (Delworth et al. 2012; Kirtman et al. 2012). Kinetic energy is fed back to the reservoir of MKE from EKE, strengthening currents and jets (Berloff et al. 2009; Radko 2016). Additionally, eddies effectively flatten isopycnal slopes due to their down-gradient flux of buoyancy (e.g. Gent and Mcwilliams 1990). Thus, EKE directly (dynamically) and indirectly (through changes of hydrographic properties) influences the location and strength of currents and fronts. The mean circulation and the associated distribution of sea surface temperature then is a crucial driver of atmospheric circulation, especially atmospheric convection and thus precipitation (Minobe et al. 2008; Frankignoul et al. 2011). Mesoscale features are also known to locally influence atmospheric winds, clouds and precipitation (Frenger et al. 2013; Small et al. 2014). The distribution and temporal variability of EKE is thus crucial to understand the whole climate system and its potential future changes.

In an ocean-only model, such as the one used in this thesis, an impact of EKE on the atmosphere is not simulated, as the atmospheric state is a prescribed boundary condition. While this inhibits an investigation of the whole feedback loop between atmosphere and ocean, it constitutes a simplified framework in which the influence of the atmospheric variability on EKE can be studied. One advantage of ocean-only models is the ability to perform hindcast simulations, where the ocean is driven by the observed atmosphere of the last decades and thus changes in the model's circulation can be compared to observed changes. However, variations of ocean currents, and especially the mesoscale, are not always easily connectible to certain changes in the atmosphere. Recent studies show the temporal variations of the oceanic mesoscale to be largely intrinsic or internal to the ocean (Combes and Di Lorenzo 2007; Penduff et al. 2011; Sérazin et al. 2015; Wilson et al. 2015). Even changes of the mesoscale on interannual to decadal time scales cannot be attributed to a certain large-scale atmospheric forcing in many regions. Thus, the number of areas in which investigations

of the atmosphere's influence on variations of EKE is expected to yield significant results is limited, and a need for long model simulations to successfully disentangle intrinsic and atmospherically forced variations arises.

1.2 Modeling the Mesoscale

The modeling of the oceanic mesoscale with OGCMs requires the configurations to have a sufficiently high horizontal resolution. A common measure for the ability of configurations to resolve the mesoscale is the ratio of the local grid cell size to the first baroclinic Rossby radius of deformation (e.g. Chelton 1998; Hallberg 2013). The Rossby radius decreases with increasing latitude and also depends on stratification and the ocean's depth. For the open-ocean regions studied in this thesis, the latitudinal dependence is the major factor to consider. The developments in ocean modeling of the recent decades make it possible to run high-resolution OGCMs that resolve the Rossby radius with at least 2 grid points at a wide range of latitudes (e.g. Smith et al. 2000; Maltrud and McClean 2005; Sasaki et al. 2008; Deshayes et al. 2013) and are thus capable of resolving mesoscale features. However, these configurations are still computational expensive and especially when the necessity of long simulations is taken into account, it seems desirable to rely on coarser-resolution, eddy-permitting configurations to investigate certain processes. An additional advantage of these less expensive configurations is the possibility to conduct a range of sensitivity studies regarding parameter choices and forcing strategies.

While resolutions of $1/10°$ and higher are inevitable to simulate the mesoscale at mid-latitudes and further poleward, eddy-permitting resolutions resolve, at least partly, the most energetic parts of the mesoscale spectrum in the tropics and subtropics. There, a realistic simulation of mesoscale features is often limited by the parameterized diffusion of momentum. In order to prohibit the accumulation of energy at the grid scale, a viscosity parameterization is implemented that removes this energy and mimics its small-scale dissipation. However, the most common forms of viscosity parameterizations also remove energy from scales close to the grid scale. In eddy-permitting simulations, these affected scales lie within the mesoscale range and the choice of viscosity thus directly affects the EKE by dissipating parts of it. To allow for a free evolution of the resolved dynamical scales, the viscosity parameter should be chosen as small as possible. Reducing the viscosity is known to improve the representation of EKE

(Böning et al. 1991) and large scale currents (Jochum et al. 2008) in eddy-permitting configurations. At the same time, the viscosity needs to be large enough to ensure numerical stability and suppress spurious diapycnal mixing (Megann 2018). Several constraints such as the viscous Courant-Friedrichs-Levy criterion (Jochum et al. 2008), the Grid-Reynolds number (Griffies and Hallberg 2000), and the Munk boundary layer (Munk 1950) limit the choice of an adequate viscosity parameter. However, these constraints still leave a range of possible values to explore within the specific configuration at hand and the region under investigation.

1.3 Case Studies

As outlined in section 1.1, EKE is of profound importance to the oceanic circulation and its interaction with the atmosphere. However, the intrinsic variability of the ocean hinders meaningful investigations of the atmospheric influence on the temporal variations of EKE in many parts of the world's oceans. Thus, the selection of regions to focus on in this thesis is not solely guided by their importance to the large scale ocean circulation and the urge to understand the generation as well as the impact of mesoscale variability, but also by the necessity to identify regions in which an attribution of an atmospheric driver to the temporal variations of the mesoscale is possible. Two of the regions to fulfill these requirements are introduced in the following.

1.3.1 The South Pacific Subtropical Gyre

The subtropical gyre in the South Pacific is a key region for Mode Water formation (e.g. Sato and Suga 2009; Li 2012; Liu and Wu 2012) and thus an important part of the subtropical cells that connect the subtropical and equatorial latitudes (e.g. Lübbecke et al. 2008; Farneti et al. 2014; Yamanaka et al. 2015). Through this connection, the variability of the subtropical South Pacific is communicated to the tropical circulation system and influences dynamic and hydrographic properties of the equatorial ocean, directly associated with El Niño and the Earth's climate system.

Formation regions of subtropical Mode Water are often located in the vicinity of the subtropical fronts. In the South Pacific, the meridional density gradient across this front drives a near-surface, eastward current (Merle et al. 1969; Morris et al.

1996), the Subtropical Countercurrent (STCC). At a mean zonal velocity of roughly 5 cm s^{-1} (Qiu and Chen 2004), it is located between 25° and 33°S above the westward (-2 cm s^{-1}) South Equatorial Current (SEC). The vertical shear of the horizontal velocities between the STCC and the SEC generates baroclinic instability (Qiu and Chen 2004), resulting in elevated mesoscale variability along the STCC. The EKE in the STCC exhibits temporal variability on seasonal to decadal time scales driven by changes in the meridional density gradient across the subtropical front (Travis and Qiu 2017). Due to its close proximity to the Mode Water formation regions, changes in the STCC could potentially impact Mode Water and thus the subtropical cells and the equatorial Pacific, especially when considering that mesoscale eddies are known to influence the formation process of Mode Water (Qiu et al. 2007; Nishikawa et al. 2010).

In contrast to other subtropical gyres, the intrinsic variability of the mesoscale in the South Pacific along the STCC is not dominant compared to the variability that can be attributed to an atmospheric forcing (Sérazin et al. 2015). It is thus possible to connect large scale atmospheric variations to the variability of the ocean circulation and its EKE. In this thesis, the focus is put on long-term, decadal changes, as understanding the mechanisms of these is crucial to predict how the ocean might respond to atmospheric conditions in a changing climate, and also helps to differentiate between trends induced by climate change and decadal-scale variations of the oceanic circulation.

1.3.2 The Labrador Sea

The Labrador Sea (LS) in the western subpolar North Atlantic is one of the key regions in the global-scale oceanic circulation. Due to large heat loss to the atmosphere in winter and favorable preconditioning in the form of a weak oceanic stratification, deep convection regularly occurs in the LS (e.g. Marshall and Schott 1999). The water mass formed during deep convection, the Labrador Sea Water, is one of the contributors to the lower branch of the Atlantic Meridional Overturning Circulation (AMOC). The AMOC, together with its temporal variability and connection to the atmosphere, is one of the most intensively studied oceanic phenomena. The relative role of deep convection in the LS in supplying water to the equatorward, deep flow of the AMOC, and also the connections and feedbacks between the AMOC and the atmosphere are highly debated, especially because different observations and simulations lead to dif-

ferent interpretations of how the AMOC will behave in a warmer future climate (e.g. Lozier et al. 2010; Srokosz et al. 2012).

Due to its role in the AMOC, the LS was extensively studied in the past two to three decades, and various studies found mesoscale, oceanic eddies to play a major role in determining both the location and strength of deep winter convection and the subsequent restratification of the convected water mass during spring and summer. Different types of eddies can be distinguished in the LS based on their origin, properties, vertical structure and size. The warm-core, anticyclonic Irminger Rings (IR) have diameters of 30-60 km (Lilly et al. 2003; Brandt et al. 2004) and propagate west and southwest (Katsman et al. 2004; Zhang and Yan 2018) from the West Greenland Current (WGC). In the northern central LS, they play a substantial role in stratifying the water column, thus suppressing deep convection (Chanut et al. 2008). Their role in restratifying the southern central LS (the area of observed deep convection), as well as their generation mechanisms are still debated. Additionally, smaller eddies with maximum velocities at mid-depth are found in the central LS around the edge of the convection area (Gascard and Clarke 1983; Send et al. 1995; Lilly et al. 2003). These so-called Convective Eddies (CE) are thought to effectively exchange water between within and outside the mixed patch, resulting in a restratification of the central LS. Another class of small eddies is the Boundary Current Eddies (BCE). In contrast to CE, they are shallow, surface-intensified and originate from the boundary currents along the shelf of the LS.

The EKE associated with these different types of eddies in the LS exhibits temporal variability on a variety of time scales from seasonal to decadal. The seasonal cycle of IR and BCE is closely linked to the strength of the WGC and Labrador Current (LS), respectively (Brandt et al. 2004; Chanut et al. 2008). The seasonal and interannual variability of CE is thought to be driven by the strength of deep convection (Lilly et al. 2003; Brandt et al. 2004). The interannual and longer-term variations of IR and EKE in the WGC are not well understood, possibly also due to the intrinsic variability of the ocean. There are no published investigations of the intrinsic variability of the WGC, however, inspecting Fig. 6 of Sérazin et al. (2015) shows the ratio of intrinsic to total variability of the mesoscale on long time scales to be comparably small, at least in parts of the LS. Various aspects and open questions regarding the generation of mesoscale variability and its impact on preconditioning and restratification in the LS are thus addressed in this thesis, again with a focus on long-term, decadal changes.

1.4 Objectives and Structure of the Thesis

The investigations of EKE in the STCC and the LS are based on an Ocean General Circulation Model using the NEMO code as described in section 2.1 along with the atmospheric forcing used to drive the ocean model (section 2.2). Section 2.3 is dedicated to an in-depth description and discussion of the calculation of EKE, as this is essential to the conclusions derived in the later sections. Section 3 then describes the influence of the choice of horizontal viscosity of momentum on EKE and other oceanic properties in a 1/4° configuration of the model. The aim is to improve the representation of the mesoscale, especially in the subtropical South Pacific, in preparation for section 4. In section 4 the advantage of a relatively low computational cost of the eddy-permitting configuration is exploited to study the EKE in the STCC region and its atmospherically driven variations with the help of several sensitivity simulations. In section 5, a different configuration with 1/20° resolution in the North Atlantic is used, as the investigation of EKE in the LS requires higher resolution compared to the investigation of EKE in the subtropics. The generation mechanisms, properties, and impacts on stratification and deep convection of several types of mesoscale eddies in the central LS are investigated with the help of the high-resolution simulation. Both, section 4 with a focus on EKE in the STCC and section 5 studying the EKE in the LS, feature a detailed introduction, a description of the model configuration and a summary and discussion along with the results. Section 6 then summarizes the results of this thesis and includes a discussion.

2 Model and Methods

This thesis is based on various configurations of an Ocean General Circulation Model based on the NEMO (Nucleus for European Modelling of the Ocean) code (Madec 2008) developed as part of the DRAKKAR collaboration. The details of the configurations used in each part of this thesis are described in the respective sections. In the following section 2.1 a general description of the model and common properties of the different configurations is given, accompanied by a description of the atmospheric forcing (section 2.2) used for most model simulations. Similarly to the model configurations, the methods used for the analyses are introduced in the specific chapters. However, the calculation of the essential oceanic property for all of this thesis, the Eddy Kinetic Energy, requires some in-depths considerations in section 2.3.

2.1 Model Description

NEMO is a framework for various models in the ocean. The component for ocean dynamics and thermodynamics is based on Océan PArallélisé (OPA) version 8 (Madec et al. 1998). The component for sea-ice dynamics and thermodynamics is the Louvain-la-Neuve Ice Model (LIM2; Fichefet and Maqueda 1997; Vancoppenolle et al. 2009). In some of the simulations presented in this thesis the Tracers in the Ocean Paradigm (TOP) component of NEMO has been used to simulate the distribution of passive tracers. However, none of the presented results were obtained using output from TOP.

The ocean component of NEMO is discretizing the primitive equations on a staggered Arakawa C-type grid where tracer points T are located in the middle of each grid box while the velocity points U,V and W are shifted eastward, northward, and upward to the boundary of the grid cell, respectively. This C-type grid is an effort to minimize the amount of averaging and interpolating needed to calculate the important terms of the primitive equations. The primitive equations are a combination of the simplified Navier-Stokes equations and a nonlinear equation of state. Besides some geometrical simplifications such as the spherical earth and thin-shell approximations, the important assumptions to derive the primitive equations are the well established Boussinesq, Hydrostatic, and Incompressibility hypotheses (e.g. Gill 1982), as well as the turbulent closure hypothesis which assumes that the small-scale turbulent fluxes can be expressed in terms of the large-scale circulation. This latter assumption is the basis for the

considerations regarding the lateral viscosity of momentum in section 3. Applying the simplifications above, the vector invariant forms of the primitive equations used in the model are (Madec 2008)

$$\frac{\partial \mathbf{U}_h}{\partial t} = -\left[(\nabla \times \mathbf{U}) \times \mathbf{U} + \frac{1}{2}\nabla(\mathbf{U}^2)\right]_h - f\mathbf{k} \times \mathbf{U}_h - \frac{1}{\rho_0}\nabla_h p + \mathbf{D}^{\mathbf{U}} + \mathbf{F}^{\mathbf{U}} \tag{2.1}$$

$$\frac{\partial p}{\partial z} = -\rho g \tag{2.2}$$

$$\nabla \cdot \mathbf{U} = 0 \tag{2.3}$$

$$\frac{\partial T}{\partial t} = -\nabla \cdot (T\mathbf{U}) + \mathbf{D}^T + \mathbf{F}^T \tag{2.4}$$

$$\frac{\partial S}{\partial t} = -\nabla \cdot (S\mathbf{U}) + \mathbf{D}^S + \mathbf{F}^S \tag{2.5}$$

$$\rho = \rho(T, S, p) \tag{2.6}$$

where $\mathbf{U}$ is the velocity vector (the subscript h denoting the vertical dimension is dropped), $\nabla = (\partial/\partial x, \partial/\partial y, \partial/\partial z)$, $f = 2\Omega\mathbf{k}$ is the Coriolis term (Ω is the angular velocity vector of the Earth), $\mathbf{k}$ is the locally upward unit vector, ρ is the density (ρ_0 is a reference density), p is the pressure, g the gravitational acceleration, T is temperature, and S is salinity. $\mathbf{D}$ and $\mathbf{F}$ denote parameterizations for small-scale physics and diffusion, and surface forcing terms, respectively. Here, the superscripts $\mathbf{U}$, T, and S denote momentum, temperature, and salinity, respectively. The diffusive terms for the lateral are described in more detail in section 3 and the atmospheric forcing contributing to $\mathbf{F}^{\mathbf{U}}$, $\mathbf{F}^T$, and $\mathbf{F}^S$ is described in the following section 2.2. The diffusive terms for the vertical are derived with a TKE turbulent closure scheme (Gaspar et al. 1990; Blanke and Delecluse 1993).

For the simulations used in this thesis, equations (2.1)-(2.6) are discretized. To evaluate the temporal tendencies of the quantities, a time-centered leap-frog finite differencing scheme (Mesinger and Arakawa 1976) is used for the non-diffusive terms and forward and backward differencing schemes are used for the horizontal and vertical diffusion terms, respectively. The advection of tracers is discretized using a combination of an upstream and a centered scheme, the Total Variance Dissipation (TVD) scheme (Zalesak 1979). The advection of momentum is accomplished by an energy

and enstrophy conserving second-order centered scheme adapted from Arakawa and Hsu (1990) and modified to suppress Symmetric Instability of the Computational Kind (Ducousso et al. 2017).

2.2 Atmospheric Forcing

The three forcing terms $\mathbf{F}^{\mathbf{U}}$, $\mathbf{F}^{T}$, and $\mathbf{F}^{S}$ in the primitive equations (2.1), (2.4), and (2.5) are derived from the data products comprised in the Coordinated Ocean-Ice Reference Experiments (CORE.v2; Griffies et al. 2009; Large and Yeager 2009). The associated bulk formulations described in Large and Yeager (2004) are used to transfer the atmospheric data to the ocean surface. The CORE.v2 dataset provides atmospheric variables to calculate air-sea heat, freshwater and momentum fluxes on a T62 atmospheric grid (roughly $2^{\circ}\times2^{\circ}$) for the period 1948-2009. The atmospheric state, as represented by near-surface wind, temperature, specific humidity and sea level pressure, is based on output from a global NCEP/NCAR reanalysis (Kalnay et al. 1996) and provided at a 6-hourly temporal resolution. Due to known errors and biases, the reanalysis data are adjusted with the help of observational datasets where possible. Near-surface winds are corrected by QSCAT scatterometer wind vectors (Chin et al. 1998), a lower limit for temperature is set at high latitudes, and the specific humidity is adjusted to the NOC1.1 climatology (Josey et al. 1998).

Radiation and precipitation are added from sources different to the NCEP/NCAR reanalysis. Daily mean ISCCP-FD data (Zhang 2004) are used, with some corrections, for radiation estimates, and a combination of CMAP (Climate Prediction Center Merged Analysis of Precipitation; Xie and Arkin 1996) and GPCP (Global Precipitation Climatology Project; Huffman et al. 1997) is used for monthly mean precipitation, together with S-H-Y (Serreze and Hurst 2000; Yang 1999) at very high latitudes. Note that the precipitation and radiation data are only available from 1979 and 1984, respectively. The forcing dataset contains monthly (precipitation) and daily (radiation) climatological mean values for the earlier years.

Additionally to the interannually varying dataset described above, CORE.v2 provides a Normal-Year-Forcing (NY). The NY consists of a single annual cycle that represents a climatological mean state but also includes synoptic variability. For this annual cycle, climatological averages over all available years of radiation (daily) and precipi-

tation (monthly) are used. The variables describing the atmospheric state (winds, temperature, and humidity) are treated in a more complex way, to ensure synoptic variability is present in the resulting annual cycle and the NY is not biased towards some specific climate state (see Large and Yeager 2004). The CORE.v2 atmospheric forcing is modified for the sensitivity studies in section 4 as described in detail in the corresponding section 4.2.

2.3 The Calculation of Eddy Kinetic Energy

The Eddy Kinetic Energy is defined to be the energy of the horizontal flow at the mesoscale, i.e. on time scales of weeks to several months and spatial scales on the order of tens to hundreds of kilometers (e.g. Stammer and Böning 1996). The mesoscale is separated from the larger and slower scales by a decomposition of the flow field in the time domain, as most commonly practiced when studying oceanic EKE. A separation from smaller and faster scales is not pursued in this study as the 1/4° configuration used in sections 3 and 4 does not spatially resolve features below the mesoscale. The 1/20° configuration used in section 5 could potentially resolve parts of the submesoscale, especially at low latitudes. However, the submesoscale, even when fully resolved, contains considerably less energy than the mesoscale (e.g. Callies and Ferrari 2013) and thus its contribution to the EKE is neglected here.

Following these considerations,

$$(u',\, v') = (u - \overline{u}^a,\, v - \overline{v}^a) \tag{2.7}$$

$$\mathrm{EKE} = \frac{1}{2}(\overline{u'^2 + v'^2}^b) \tag{2.8}$$

$$\mathrm{MKE} = \frac{1}{2}(\overline{\overline{u}^{a\,2} + \overline{v}^{a\,2}}^b) \tag{2.9}$$

$$\mathrm{KE} = \mathrm{MKE} + \mathrm{EKE} = \frac{1}{2}(\overline{u^2 + v^2}^b) \tag{2.10}$$

where u and v are the zonal and meridional horizontal velocities, respectively, and $\overline{\cdot}^a$ and $\overline{\cdot}^b$ denote a temporal average over the period of length a and b, respectively. MKE is the kinetic energy of the mean flow and KE denotes the total kinetic energy of the

flow. Equation (2.10) only holds for $a = b$, i.e. the averaging periods are the same (see Kang and Curchitser 2017). Although different averaging periods ($a \neq b$) introduce an additional term (RES) in (2.10) such that KE = MKE + EKE + RES, $a \neq b$ is often used to investigate specific aspects of the mesoscale EKE.

Two main aspects are considered when choosing the averaging periods a and b. First, a should be chosen in such a way that (u', v') and thus EKE represent the mesoscale, i.e. time scales on the order of weeks to a few months. Second, b needs to be suitable to investigate the processes under consideration. For example, an averaging period of $b = 1$ year is not suitable to study the seasonal cycle of EKE. At the same time, the error should be small when it is necessary to choose $a \neq b$.

• **Multi-year a and b** Especially when the mean spatial distribution of EKE is studied, a and b are often chosen to be the total length of the available dataset (e.g. Stammer et al. 2006). Even though $a = b$ is then satisfied, the first aspect mentioned above is not adhered to. For example in a case where $a = b = 30$ years, several features of the mean currents such as interannual and longer term variations are included in (u', v') and thus considered to be mesoscale EKE. As one of the aims of this thesis is to study interannual and decadal variations of EKE, it seems not advisable to follow this path.

• **1-year a and b** A more promising option to investigate interannual to decadal variations of the mesoscale is to choose $a = b = 1$ year. The changes of the mean currents at these time scales are not included in EKE and (2.10) holds. However, possible variations of the large scale circulation at seasonal time scales are still included in (u', v'). The error made with $a = b = 1$ year depends on the region of interest. In regions with a strong seasonal cycle of the circulation such as the tropical Indian Ocean this error can be large and affect the interannual variability of EKE (Fig. 2.1a and b). In other regions such as the subtropical South Pacific (Fig 2.1d and e) or the subpolar North Atlantic (Fig. 2.1g and h), the error is comparably small. Specifically, the mean EKE is affected by the inclusion of the seasonal cycle of the mean currents but the interannual and decadal variations of EKE remain of similar amplitude, relative to the respective mean. A detailed quantification of the error is not possible as all other methods described below impose errors as well, so that the discussion of the error

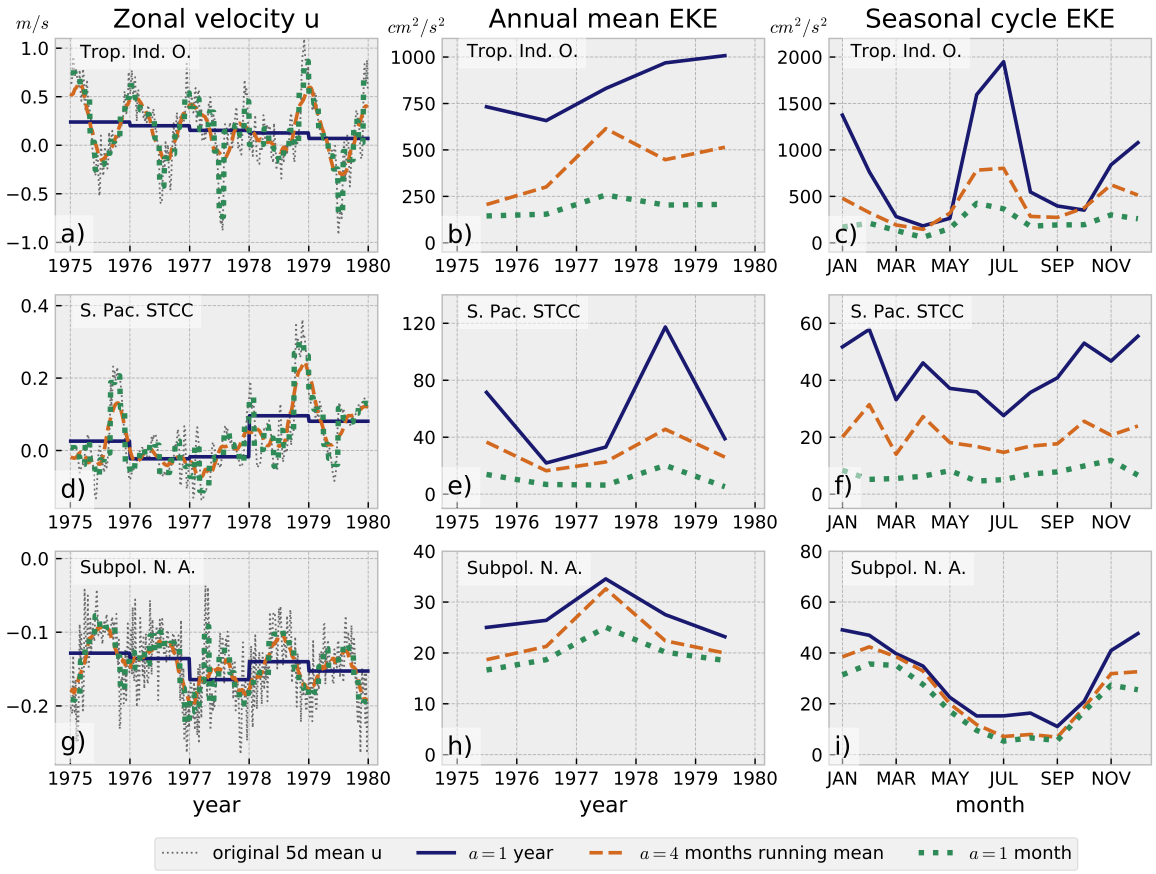

Figure 2.1: Different ways to calculate EKE as described in the text for three different regions: (a)-(c) The tropical Indian Ocean (50°E, 1°N) with a strong seasonal cycle of the mean current, (d)-(f) the subtropical South Pacific STCC (160°W, 27°S) with relatively low EKE, and (g)-(i) the subpolar North Atlantic WGC (44°W, 59°N) with strong EKE. The left column (a), (d), and (g) displays the original 5-day mean zonal velocity u (thin gray line), annual mean u (solid dark blue line), a 4-month running mean u (dashed orange line), and monthly mean u (dotted green line) for the arbitrary period 1 Jan. 1975 to 31 Dec. 1979. The center column (b), (e), and (h) shows annual mean EKE for the same period as calculated based on annual mean u (solid dark blue line), a 4-month running mean u (dashed orange line), and monthly mean u (dotted green line). The right column (c), (f), and (i) depicts the monthly seasonal cycle of EKE for the period 1970-1999. Colors and styles of the lines are identical to the center column. The details of the different methods to calculate EKE are described in the text.

needs to remain qualitative. A major disadvantage of $b = 1$ year is the impossibility to study the seasonal cycle of EKE. To overcome this shortcoming, b can be chosen to be 1 month.

• **1-year a and 1-month b** Choosing $a = 1$ year and $b = 1$ month yields an additional error in the amplitude and phase of the seasonal cycle of EKE due to the term RES in (2.10) which is small in most regions, as already shown by Kang and Cur-

chitser (2017). However, it can potentially be large in other regions, so that careful inspection is necessary before investigating the seasonal cycle of EKE. In the subpolar North Atlantic (Fig. 2.1i), all three methods yield similar mean and amplitude of the seasonal cycle. In the South Pacific STCC (Fig. 2.1f), the case where $a = 1$ year and $b = 1$ month exhibits a similar phase of the seasonal cycle as the running mean a and the relative (to the mean) amplitude is comparable. In the tropical Indian Ocean (Fig. 2.1c), the timing of the seasonal cycle is comparable between all three methods, however, the relative amplitude is drastically increased (compared to the running mean a) and $a = 1$ year, $b = 1$ month appears to be inadequate for the tropical Indian Ocean, where the seasonal cycle of the mean currents is large.

• **1-month a and b** One possible solution to study the seasonal cycle of EKE without the introduction of the residual term in (2.10) is to set $a = b = 1$ month. However, this does not fully take into account the definition of the mesoscale. Using the deviations (u', v') from monthly mean values implies that the mesoscale features under investigation have time scales shorter than one month. This assumption is not valid in most regions of the world's oceans and indeed, $a = b = 1$ month yields a significant reduction of EKE and its variability in the tropics and subtropics (Fig. 2.1b, c, d, and f).

• **Running mean a** To include the full range of mesoscale variability in (u', v') and simultaneously study the seasonal cycle of EKE at a high resolution (as opposed to e.g. seasonal averages) it is possible to define a running mean window and filter the original time series of (u, v) do derive ($\overline{u}$, $\overline{v}$). However, this method still involves a residual term (Kang and Curchitser 2017) in (2.10) and additionally is computationally expensive compared to the other methods. Nevertheless, the error made by a running mean a appears to be the smallest of the errors associated with the methods discussed here and can serve as a reference for the other methods in Fig. 2.1.

The main features of Eddy Kinetic Energy investigated in this thesis are its interannual to decadal variations. With a focus on these long time scales, most results are derived utilizing annual or longer mean values of the quantities under consideration. Furthermore, it is desirable to calculate EKE in the same manner everywhere, and for investigations of all time scales. In the subpolar North Atlantic, the region of focus of section 5, the amplitude and phasing of the temporal variations of EKE are almost

independent of the method chosen. In the subtropical South Pacific (focus of section 4), the different methods exert a larger influence on the EKE. Setting $a = b = 1$ month almost diminishes the seasonal and longer scale variations of EKE, in fact even the mean EKE is greatly reduced. Clearly, the choice of $a = 1$ month attributes parts of the mesoscale to $(\overline{u}, \overline{v})$ and is thus disregarded. When choosing $a = 1$ year and $b = 1$ year for the investigation of interannual to decadal variability and $b = 1$ month for the investigation of the seasonal cycle, the differences to the case where a is a running mean are mostly confined to the average EKE. The effects on the relative amplitudes and the phase of variations and the seasonal cycle are only minor. Additionally, the running mean method has the disadvantage of the computational expense, which is considered more important than its better accuracy at this point. Thus, to ensure EKE is efficiently calculated in the same way for all regions, $a = 1$ year in the remaining sections of this thesis. When focusing on interannual to decadal variability $b = 1$ year, and $b = 1$ month for the investigation of the seasonal cycle.

It should be noted that the insights gained in this thesis do not depend on the choice of a and b. All methods but $a = b = 1$ month yield similar variations relative to the mean EKE at seasonal, interannual, and decadal time scales in the subtropical South Pacific and the subpolar North Atlantic. In the regional context of this study, the method used to derive EKE is thus not critical to the investigation of the time scales considered. Only when a comparison of the energy of the mesoscale and the mean circulation, i.e. EKE and MKE, is required, does the choice of a and b become essential. In the subtropical South Pacific for example, EKE is 7 times as large as MKE when $a = b = 30$ years (not shown). In the case $a = b = 1$ year this factor reduces to 6 and for $a = b = 1$ month EKE and MKE are almost identical. Depending on the method chosen, it could be claimed that EKE is an order of magnitude larger than MKE or that they are of similar magnitude. Therefore, it is essential to carefully choose the averaging periods a and b for the calculation of EKE depending on the investigated region and the processes to study.

3 On the Influence of Lateral Diffusion of Momentum on Eddy Kinetic Energy in an Ocean General Circulation Model

3.1 Background

The technological advances of the recent decades make it possible today to integrate Ocean General Circulation Models in global configurations at high resolutions of $1/10°$ and higher for simulation periods of up to a few decades (e.g. Smith et al. 2000; Maltrud and McClean 2005; Sasaki et al. 2008; Deshayes et al. 2013; Rieck et al. 2015; Sérazin et al. 2015). One of the key advantages of these high-resolution OGCMs is their ability to simulate the oceanic mesoscale and its effects on the ocean's climate at a wide range of latitudes (cf. Hallberg 2013). However, even by today's standards, OGCMs with resolutions finer than $1/10°$ are computationally expensive and under certain circumstances it is favorable to use a model with a coarser resolution, depending on the processes to investigate and the latitudinal range involved. The major benefits of coarser-resolution OGCMs is the possibility to extend the simulation length and conduct sensitivity studies to investigate different parameter spaces or the influence of certain aspects of the atmospheric forcing. To exploit these benefits, section 3 and 4 of this thesis are based on an eddy-permitting $1/4°$ OGCM.

A $1/4°$ OGCM should be able to resolve the first baroclinic Rossby radius of deformation and thus at least parts of the mesoscale variability from the equator to roughly $20-25°$ North and South (Chelton 1998). Earlier studies utilizing $1/4°$ configurations exhibit mesoscale eddies and variability well into the midlatitudes (e.g. Penduff et al. 2010; Sérazin et al. 2015), although less of the range of mesoscale features is resolved the further poleward the area of investigation is located. It thus seems promising to use a $1/4°$ OGCM to investigate mesoscale variability in the subtropics and at the same time carry out sensitivity studies with variations to the atmospheric forcing and some tests with changing model parameters. One of the most challenging parameters to define, especially within an eddy-permitting model, is the lateral diffusion of momentum that will be discussed here.

Physically, momentum is dissipated by friction on the molecular scale. As ocean models do not resolve such small scales, a viscosity parametrization is implemented to account for the transfer of energy toward smaller scales and its dissipation. A second role of the viscosity is to ensure numerical stability of the model. Depending on the horizontal resolution, the resolved dynamical processes flux a certain amount of energy to smaller scales which then is essentially trapped at the grid-scale. The viscosity parametrization acts to dissipate this energy at the grid-scale and suppresses the growth of unstable waves that could potentially lead to a blow-up of the model. Most advection schemes implemented in model formulations yield some additional numerical dissipation of energy, but this aspect is not discussed here in detail.

In very high-resolution models that resolve ocean dynamics down to the scale at which the direction of the energy flux changes from upscale to downscale (e.g. Scott and Wang 2005), the role of the parametrization of lateral viscosity of momentum is relatively straight-forward to assign. The energy flux from smaller scales to larger scales is explicitly simulated by the model and the viscosity parametrization only needs to account for the flux toward smaller scales that are not resolved by the model and the dissipation at the molecular scale.

In coarse-resolution models (0.5° and lower) the mesoscale is not resolved. Both the effect of mesoscale eddies on the large-scale oceanic properties and the flux of energy toward small scales can be parametrized though. Gent and Mcwilliams (1990) show one example for the parametrization of the effect of mesoscale eddies. Their parametrization essentially aims at mimicking baroclinic instability with the help of an additional eddy-induced advection velocity, reducing the lateral gradients of tracers and the available potential energy. The flux of energy to the small scales is, as in high-resolution models, approximated by the viscosity. In coarse-resolution models the parametrized viscosity removes energy from scales that are much larger than physically realistic. However, this deficiency can be partly counteracted because the oceanic mesoscale and its effect on the larger scales are parametrized, and thus controllable, as well.

The most problematic case with respect to the choice of lateral viscosity is the case of intermediate resolution between 1/3° and 1/10°, 1/4° in this study. At 1/4°, the mesoscale is partly resolved, at least in the tropics and subtropics. Thus, the grid-scale of the model configuration lies within the mesoscale range and energy from this grid-

scale could be fluxed to larger scales. However, numerical dissipation and viscosity in its most common forms only dissipate energy, i.e. parametrize the flux of energy to smaller scales, and thus do not account for the mesoscale's effect on the large-scale. Due to this contradiction, the choice of lateral viscosity in eddy-permitting ocean models is a delicate one. On the one hand, the viscosity needs to be large enough to assure that energy does not accumulate at the grid-scale. On the other hand, the viscosity should be chosen as small as possible to allow a free evolution of the dynamical features resolved by the model.

Several constraints, based on theoretical considerations, limit the choice of an adequate magnitude of the lateral viscosity of momentum. An upper bound is given by a criterion for numerical stability, the viscous Courant-Friedrichs-Levy criterion (Jochum et al. 2008). This upper bound should be adhered to in order to avoid the possibility of diffusion of momentum across more than one grid cell in one time step. Furthermore, there are two constraints on the lower bound of an adequate lateral viscosity (Bryan et al. 1975; Large et al. 2001). First, the Grid-Reynolds number should not exceed some threshold α in order to suppress grid-scale noise. In the case of advection schemes based on centered differences, $\alpha = 2$ for second-order diffusive operators and $\alpha = 16$ for fourth-order diffusive operators (Griffies and Hallberg 2000). Second, the grid needs to resolve the Munk boundary layer (Munk 1950). This boundary layer is determined by the ratio of the viscosity and the planetary vorticity gradient. Essentially, the Munk boundary layer becomes thinner for decreasing vorticity and the grid spacing needs to be chosen adequately to resolve it. Or, when the grid-spacing is fixed, the viscosity should not decrease below a certain threshold.

The upper and lower theoretical bounds for the viscosity parameter still leave a range of possible choices that is additionally influenced by the numerical diffusion of the advection scheme. The numerical diffusion is often unknown and hard to assess (e.g. Ilıcak 2016) so that a careful testing of different viscosity parameters is necessary to find an adequate value and achieve the best results. A rather large viscosity near the upper limit ensures a minimum of numerical noise and thus reduces spurious, undesirable diapycnal mixing of tracers (Megann 2018). At the same time, the stronger diffusion of momentum weakens gradients across fronts and could potentially decrease the generation of instabilities and mesoscale variability. Especially in an eddy-permitting simulation, e.g. the $1/4°$ simulation used in this study, the viscosity should be kept as low as possible in order to benefit from the partly resolved mesoscale and its effects on

the large-scale circulation. Indeed, reducing the viscosity has been shown to increase Eddy Kinetic Energy (Böning et al. 1991) and improve the representation of many large-scale currents (Jochum et al. 2008) in eddy-permitting models. Jochum et al. (2008) even argue that violating some of the theoretical constraints mentioned above can be beneficial to eddy-permitting simulations. Specifically, the advantages of a more vigorous eddy field and its effect on the mean currents can potentially outweigh the disadvantages of an increased level of grid-scale noise.

Based on these considerations, the effect of a reduced lateral viscosity on EKE in the eddy-permitting ocean model configuration used in section 4 of this thesis is investigated in this section. The aim is to optimize the simulation's ability to represent mesoscale variability without developing an excessive amount of grid-scale noise. The regional focus is on the subtropical South Pacific, the study region of section 4.

3.2 Model Configuration

The specific configuration of the model (described in section 2) used in this section is global and eddy-permitting at a horizontal resolution of 1/4° (ORCA025). It has an orthogonal, curvilinear, tripolar Arakawa-C type grid, shared with the numerous varieties of the ORCA025 configuration developed within the DRAKKAR framework (DRAKKAR Group 2007, 2014). The version of ORCA025 used in this study has 46 vertical levels with increasing thickness toward the ocean bottom. The surface grid cell is 6 m and cells at depth are up to ~ 250 m thick, with 24 (9) of the 46 cells being located in the upper 1000 m (100 m). A partial-cell formulation is applied for the bottom cells (cf. Barnier et al. 2006). The data products and bulk formulations of the Coordinated Ocean-Ice Reference Experiments version 2 (CORE.v2) are used to atmospherically force the simulations (see section 2 for a detailed description of CORE.v2). All model simulations apply a very weak sea surface salinity restoring (SSSR) to climatology (PHC2.1, updated from Steele et al. 2001) of 33.33 mm day^{-1}, which corresponds to a relaxation time scale of 1500 days over a 50 m surface layer.

The presented configuration of ORCA025 uses a bilaplacian horizontal diffusion for momentum. The fourth order diffusive operator from the momentum equations (see

section 2) is given by (see Madec 2008)

$$\mathbf{D}^{lU} = \nabla_h \left\{ \nabla_h \cdot \left[-A^{lm} \nabla_h(\chi) \right] \right\} + \nabla_h \times \left\{ \mathbf{k} \cdot \nabla \times \left[-A^{lm} \nabla_h \times (\zeta \mathbf{k}) \right] \right\} \tag{3.1}$$

where $\nabla_h = \frac{1}{e_1}\frac{\partial}{\partial i}\mathbf{i} + \frac{1}{e_2}\frac{\partial}{\partial j}\mathbf{j}$, A^{lm} is the viscosity coefficient, $\mathbf{i}$, $\mathbf{j}$, and $\mathbf{k}$ are the unit vectors ($\mathbf{k}$ locally upward), and χ and ζ are the divergence of the horizontal velocity field and the relative vorticity, respectively, given by

$$\chi = \frac{1}{e_1 e_2}\left[\frac{\partial(e_2 u)}{\partial i} + \frac{\partial(e_1 v)}{\partial j}\right] \tag{3.2}$$

$$\zeta = \frac{1}{e_1 e_2}\left[\frac{\partial(e_2 v)}{\partial i} - \frac{\partial(e_1 u)}{\partial j}\right] \tag{3.3}$$

Here, e_1 and e_2 are the horizontal scale factors, i.e. the lengths of the grid cell in i- and j-direction, respectively. The horizontal velocities in i- and j-direction are denoted by u and v, respectively. The viscosity coefficient A^{lm} depends on the size of the grid cell considered.

$$A^{lm} = \frac{max(e_1, e_2)^3}{e_{max}^3} A_0^{lm} \tag{3.4}$$

where e_{max} is the global maximum of all horizontal scale factors e_1 and e_2 in the grid configuration and A_0^{lm} is the background viscosity coefficient. If all grid cells were the same size, $A^{lm} = A_0^{lm}$ everywhere. In ORCA025 however, grid cells are largest at the equator and decrease in size toward the poles, so that A^{lm} also decreases from A_0^{lm} at the equator to smallest values near the poles of the tripolar grid. The background viscosity coefficient A_0^{lm} (hereafter simply called viscosity) is varied in the different simulations conducted. A viscosity of A_0^{lm} =1.5×10^{11} m^{4}s^{-2} has been widely used in previous simulations with ORCA025 and acts a standard value for the control experiments V15 (spin-up experiment) and V15H (hindcast simulation) here. Three additional experiments are analyzed. A combination of a spin-up (V06) and a hindcast simulation (V06H) with a reduced viscosity of A_0^{lm} =0.6×10^{11} m^{4}s^{-2} and a short spin-up experiment with very low viscosity A_0^{lm} =0.2×10^{11} m^{4}s^{-2} (V02). While all three values for the viscosity, 1.5, 0.6, and 0.2×10^{11} m^{4}s^{-2}, lie well below the upper bound for adequate values given by the viscous Courant-Friedrichs-Levy criterion, only 1.5×10^{11} m^{4}s^{-2} fulfills the Grid Reynolds number criterion, and none of them strictly adheres to the Munk boundary layer criterion. However, as mentioned above, these viscosity parameterizations do not take into account the additional numerical diffusion by the advection scheme, so that the actual diffusion acting upon the momentum in

the simulation is higher and a stable model integration could be possible with these low values of the viscosity parameter.

In V02, the horizontal diffusion coefficient for tracers is additionally adapted to the lower viscosity for momentum. The ORCA025 simulations analyzed in this study use a laplacian diffusive operator of the form

$$\mathbf{D}^{lT} = \nabla \cdot \left(A^{lt} \, \Re \, \nabla T \right) \quad \text{with} \quad \Re = \begin{pmatrix} 1 & 0 & -r_1 \\ 0 & 1 & -r_2 \\ -r_1 & -r_2 & r_1^2 + r_2^2 \end{pmatrix} \tag{3.5}$$

where A^{lt} is the diffusion coefficient that (as for momentum in Eq. 3.4) depends on the local grid cell size, T is the tracer field and r_1 and r_2 are the slopes between isoneutral surfaces and the model's vertical level in the i- and j-direction, respectively. Analogously to the diffusion of momentum, there is a background value A_0^{lt} for the tracer diffusion coefficient A^{lt}. The standard value of A_0^{lt} in V15, V15H, V06, and V06H is 300 $\mathrm{m^2 s^{-1}}$. In V02 however, the viscosity for momentum is reduced drastically, so that A_0^{lt} is changed to 100 $\mathrm{m^2 s^{-1}}$ to avoid that the diffusion for momentum and tracers differs strongly.

The three different spin-up simulations V15, V06 and V02 are initialized with temperature and salinity from climatology (PHC2.1, updated from Steele et al. 2001) and a sea ice field from December 31st, 1992 from a previous ORCA025 simulation. First, the three simulations, only differing in their choices of diffusion coefficients, are integrated for 5 years, forced by the CORE.v2 atmospheric forcing from 1 January 1980 to 31 December 1984. The spin-up integrations for V15 and V06 are then continued for another 25 years until 31 December 2009. The state of the ocean at the end of this spin-up period is then used as the initial condition for the two hindcast simulations V15H and V06H. The hindcast simulations are integrated for 52 years with the forcing from 1 January 1958 to 31 December 2009.

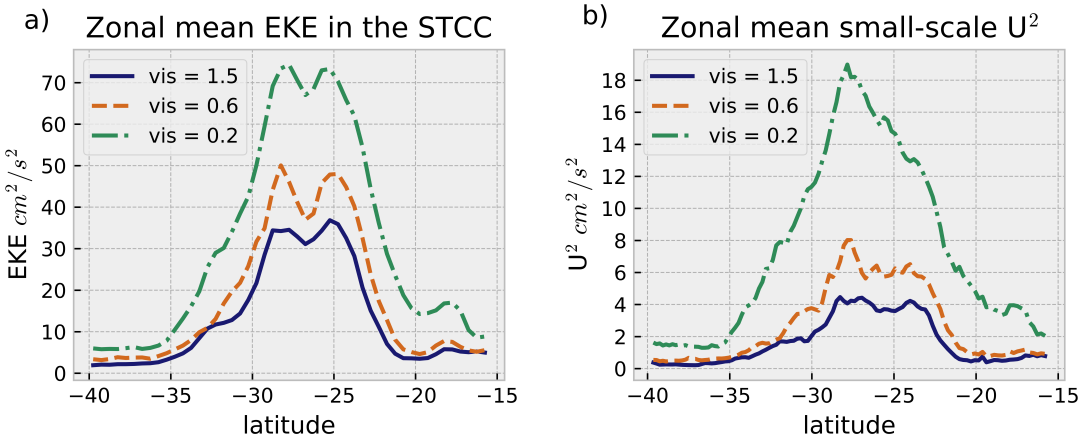

Figure 3.1: (a) Zonal mean (153 – 175°W) EKE (cm^2s^{-2}) at 94 m depth, averaged over 3 years from 1982 – 1984, for three different lateral viscosities. 1.5×10^{11} m^4s^{-2} (V15; solid blue line), 0.6×10^{11} m^4s^{-2} (V06; dashed orange line), and 0.2×10^{11} m^4s^{-2} (V02; dash-dotted green line). (b) as (a) but for small-scale squared zonal velocity U^2 (cm^2s^{-2}). Zonal velocities are filtered in the zonal and meridional directions with a boxcar window with the size of 2 grid cells and then subtracted from the original field to retain small-scale velocities.

3.3 Results

The aim of this section is to characterize and quantify the changes to EKE in the STCC and the large scale hydrographic properties and circulation resulting from different values of the viscosity parametrization. The underlying question is whether it is possible to optimize the models simulation of the mesoscale without increasing the grid-scale noise above an acceptable level.

The EKE in the subtropical South Pacific generally exhibits an increase when decreasing the model's viscosity (Fig. 3.1a). Zonally averaged from 153 – 175°W, EKE at 94 m depth in the V06 case is up to 15 cm^2s^{-2} (50%) higher in the latitude range of the STCC (∼23–30°S) when compared to V15. Outside the STCC the changes are only minor. In V02, EKE increases by 30 cm^2s^{-2} (100%) in the STCC, with respect to V15. In all three simulations, the meriodional structure of the STCC system remains unchanged with a sharp increase of EKE between 35 and 30°S, two peaks of EKE at roughly 28 and 25°S accompanied by a local minimum between these latitudes, and a decrease of EKE between 25 and 20°S.

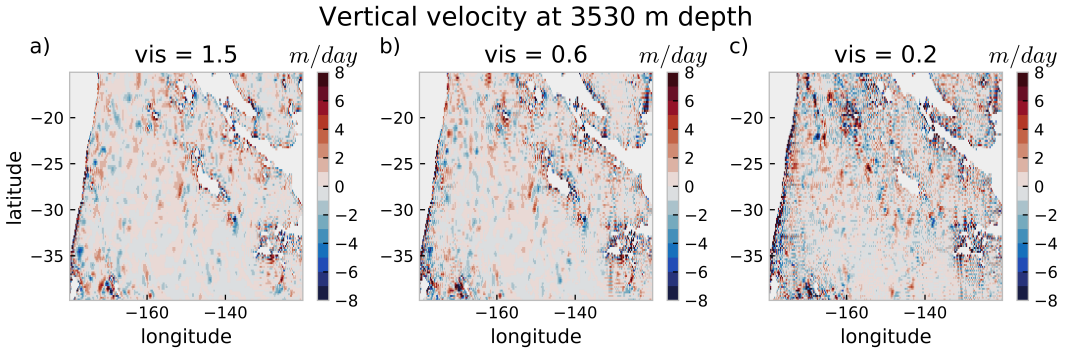

Figure 3.2: Snapshots (5-day mean) of vertical velocity (m day^{-1}) at 3530 m depth in the South Pacific for (a) V15 (viscosity of 1.5×10^{11} m^{4}s^{-2}), (b) V06 (viscosity of 0.6×10^{11} m^{4}s^{-2}), and (c) V02 (viscosity of 0.2×10^{11} m^{4}s^{-2}).

While an increase of EKE to levels as simulated by a 1/10°-simulation (see section 4.3.4) seems desirable, care has to be taken when interpreting these results. Indeed, most of the additional EKE observed in V02 stems from velocity anomalies near the grid-scale. To quantify these small-scale velocities, the zonal velocity U is filtered in the zonal and meridional directions with a boxcar window with the length of 2 grid cells (the filtered value in each cell is the mean of the unfiltered value of this cell and the cell to the west and south, respectively). These filtered fields are then subtracted from the original fields, so that only anomalies near the grid-scale are retained. These small-scale anomalies are then squared and zonally averaged (Fig. 3.1b).

The small-scale velocities in V06 are only locally larger than in V15. The maximum increases observed within the STCC (∼23-31°S) do not exceed $2-4$ cm^{2}s^{-2}. In V02 however, small-scale velocities are significantly increased between $15-36$°S. In the STCC small-scale U^2 is up to 14 cm^{2}s^{-2} larger in V02 as compared to V15. This drastic increase on the order of $300-400$% questions the usability of V02 for long, realistic hindcast simulations.

To further investigate the effect of low viscosity on grid-scale noise, the vertical velocities are studied. Vertical velocities are very sensitive to grid-scale noise in the model configuration because they are calculated diagnostically from the divergence of the horizontal velocities, simplified $-dw/dz = du/dx + dv/dy$. The influence of horizontal velocities with alternating sign from cell to cell that are characteristic of grid scale noise is thus well observable in the vertical velocities, especially near topography, where vertical velocities are generally larger.

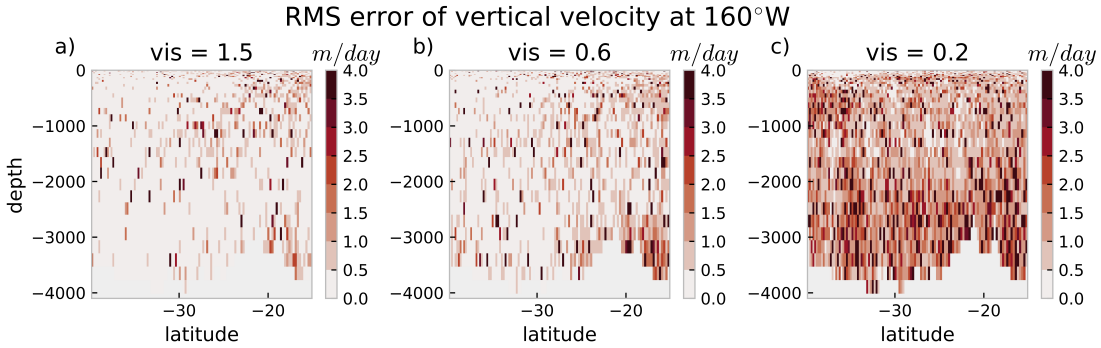

Figure 3.3: Vertical sections of the RMS error of vertical velocity w_{RMS} (m day^{-1}) at 160°W, averaged over 3 years (1982 – 1984) for (a) V15 (viscosity of 1.5×10^{11} m^{4}s^{-2}), (b) V06 (viscosity of 0.6×10^{11} m^{4}s^{-2}), and (c) V02 (viscosity of 0.2×10^{11} m^{4}s^{-2}). w_{RMS} is calculated as described in the text.

The vertical velocities in the interior basins at 3530 m depth, away from topography are generally below 2 m day^{-1} (Fig. 3.2). In V15 higher velocities are found e.g. near the ridges in the northwestern part of the investigated region. At some locations (for example between 140 – 150°W, near 25°S) the typical pattern of grid-scale noise can be observed even with the standard viscosity parametrization. In V06, the vertical velocities in the interior are not changed significantly, whereas grid-scale noise can be seen close to all the topographic features in the region at a slightly increased level compared to V15. For the low viscosity case, the majority of vertical velocities can be attributed to noise. Close to topography, the velocities often exceed 10 m day^{-1} and the typical pattern of velocities of alternating sign in neighboring grid cells can be observed hundreds of kilometers away.

To better quantify the amount of grid-scale noise, the vertical velocities are vertically smoothed with a 5-point Hanning window (w_{smooth}) and a root-mean-square (RMS) error is calculated.

$$w_{RMS} = \left\langle \sqrt{\frac{(w - w_{smooth})^2}{w^2}} \right\rangle \tag{3.6}$$

Here, $\langle\cdot\rangle$ denotes a temporal mean. This approximation of grid-scale noise is displayed in Figure 3.3. For V15, there are low levels of noise in most of the region, with only slightly increased levels north of 25°S in the upper ocean and near the ridge north of 20°S in the deep ocean. Average values of the RMS error are 0.58 m day^{-1} for the upper 1000 m and 0.37 m day^{-1} for the depths below 1000 m. Decreasing the

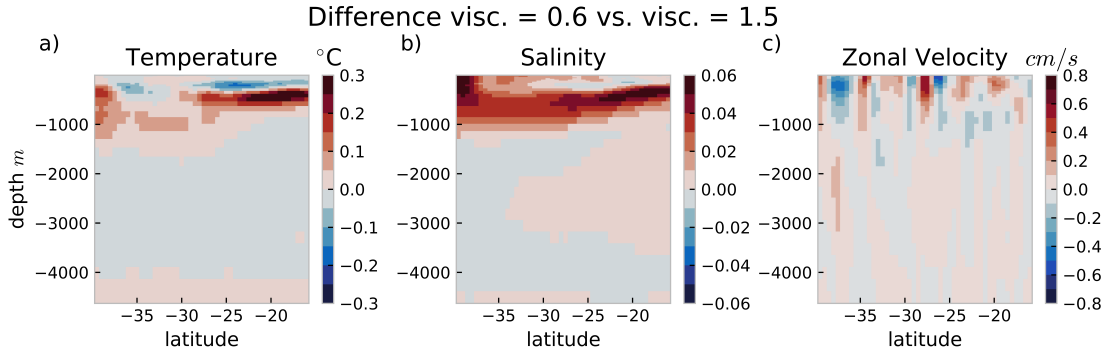

Figure 3.4: Differences between V06H (viscosity 0.6×10^{11} m^{4}s^{-2}) and V15H (viscosity of 1.5×10^{11} m^{4}s^{-2}), zonally averaged over $153-175$°W for the period $1980-2009$. Displayed are differences in (a) temperature (°C), (b) salinity, and (c) zonal velocity U (cm s^{-1}).

viscosity to the medium value (V06) yields a weak increase of noise everywhere, with average values of 0.74 m day^{-1} for the upper ocean and 0.50 m day^{-1} below 1000 m. The largest increase is found in the deep ocean north of 20°S, close to the topographic feature there. In V02, noise is significantly increased at all depths and latitudes, with largest increases in the deep ocean, and in the surface ocean south of 30°S. Average values are increased by ∼700% in the upper 1000 m (4.69 m day^{-1}) and by ∼400% below (1.82 m day^{-1}). Note that the average values for w_{RMS} presented here seem contradictory to Figure 3.3, where w_{RMS} appears larger at depth compared to the upper ocean. However, while w_{RMS} exhibits a more homogeneous increase at all latitudes below 1000 m, single grid cells in the upper ocean have values much larger than the maximum of the color scale in Figure 3.3 so that the average value of w_{RMS} is higher above 1000 m.

While the increase in grid-scale noise is relatively small in V06, so that this simulation should not necessarily be excluded from further investigations, the noise levels in V02 are well above an acceptable value. In the following, the influence of reduced viscosity on hydrographic properties and the large scale circulation will thus be studied with the help of two 52 year long hindcast simulations with viscosity parameters of 1.5×10^{11} m^{4}s^{-2} (V15H) and 0.6×10^{11} m^{4}s^{-2} (V06H).

The changes in temperature and salinity are below 5% and 0.5%, respectively, of the mean in V15H. Significant influence of the reduced viscosity on the mean temperature is only exerted above 1000 m depth. Especially north of 28°S, where a dipole structure emerges with a temperature increase of up to 0.3°C below a decrease of more than

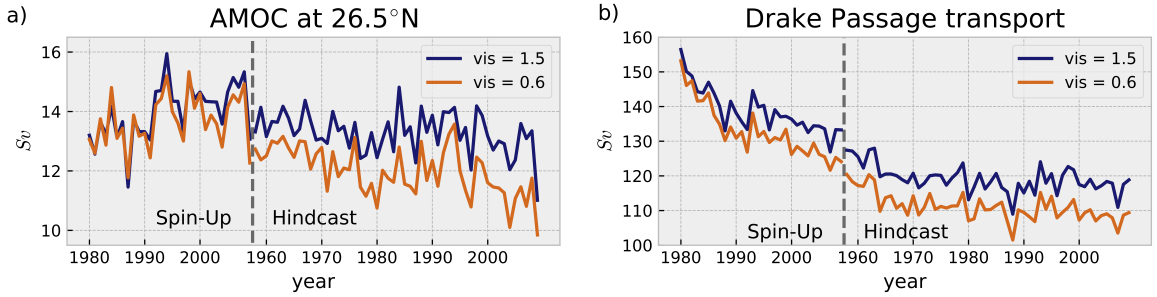

Figure 3.5: Annual mean values of (a) the maximum transport of the Atlantic Meridional Overturning Circulation at 26.5°N and (b) the transport through Drake Passage between South America and Antarctica, both in SV ($1\ Sv = 10^6\ \mathrm{m^3 s^{-1}}$). Displayed are the Spin-Up periods (left of the vertical dashed gray line) and the Hindcasts (right of the vertical dashed gray line) for the standard viscosity of $1.5{\times}10^{11}\ \mathrm{m^4 s^{-2}}$ (V15 and V15H; solid blue line) and the reduced viscosity(V06 and V06H; $0.6{\times}10^{11}\ \mathrm{m^4 s^{-2}}$).

0.1°C above $\sim$ 200−250 m (Fig. 3.4a). The changes in salinity are similarly restricted to the upper 1000 m (Fig. 3.4b). At the latitudes of the STCC, salinity increases by up to 0.06 below 200−250 m, however, only a marginal decrease is observed above. Both the changes in temperature and salinity indicate that the vertical gradients in the upper ocean are weakened in V06H, compared to V15H. There are two probable explanations for this observed weakening. First, the reduced viscosity in V06H allows stronger mesoscale horizontal velocities (EKE) to develop (Fig. 3.1). The horizontal circulation of mesoscale eddies features an associated vertical velocity field, that is increased for higher horizontal velocities. These additional vertical velocities then lead to an increased exchange of warm, saline water near the surface and cooler, less saline water below, resulting in a net cooling and freshening above 200−250 m and a net warming and salinification below. Second, the vertical velocities near the grid-scale in V06H are also slightly increased compared to V15H (Fig. 3.3), essentially having the same effect on the vertical distribution of temperature and salinity as the mesoscale velocities described above.

Changes in the mean horizontal velocities between V15H and V06H are below 10% of the mean in most of the STCC and have alternating directions (Fig. 3.4c). The influence of the reduced viscosity on mean currents is not easily discernible. While a lower viscosity should allow for sharper fronts to develop, the increased EKE should also lead to a stronger work by the eddies to flatten the fronts. The result is a rather heterogeneous distribution of alternating velocity changes, so that no substantial change in the mean transport of the STCC is expected.

On a global scale, the choice of the viscosity parameter does appear to influence the mean circulation. The Atlantic Meriodional Overturning Circulation (AMOC) and the transport through Drake Passage (as an indicator for the Antarctic Circumpolar Current strength) decrease by $5-10\%$, when reducing the viscosity from 1.5×10^{11} $\mathrm{m^4s^{-2}}$ to 0.6×10^{11} $\mathrm{m^4s^{-2}}$ (Fig. 3.5). While V15 and V06 exhibit a nearly identical AMOC throughout the first 20 years of the Spin-Up phase, the Drake Passage transport already diverges after less than 10 years. This points to different reasons for the reduction of the AMOC and Drake Passage Transport. However, these are not further investigated due to their limited effect on the dynamics of the STCC on the time scales considered here.

3.4 Conclusion

Three different choices of biharmonic laplacian viscosity for lateral momentum are tested for their suitability for a simulation of the South Pacific STCC and its associated EKE within a $1/4°$ Ocean General Circulation Model. The standard viscosity of 1.5×10^{11} $\mathrm{m^4s^{-2}}$ (V15) is reduced to 0.6×10^{11} $\mathrm{m^4s^{-2}}$ (V06) and 0.2×10^{11} $\mathrm{m^4s^{-2}}$ (V02). Both reductions yield an increase in the STCC's EKE of 50 and 100%, respectively. However, they are also accompanied by an increase of grid-scale noise in the velocities. While grid-scale noise increases by $20-30\%$ in V06, a drastic increase of $400-700\%$ is observed in V02, depending on the depth range investigated. The very low viscosity in V02 is thus considered not suitable for the $1/4°$ ORCA025 simulation and only the hindcast simulations V15H and V06H are compared with respect to the viscosities impact on mean temperature, salinity and velocity fields.

The reduced viscosity in V06H leads to changes in STCC region smaller than 5 and 0.5% for mean temperature and salinity, respectively. Largest changes are found in the upper 1000 m of the water column, where a reduction of the vertical gradients is observed. There is no unidirectional influence of the reduced viscosity on the mean zonal velocity and thus the transport of the STCC. On the global scale, V06H exhibits a $\sim$10% decrease of the Atlantic Meridional Overturning Circulation and the transport through Drake Passage, compared to V15H. As transports in the AMOC and through Drake Passage are already rather low in ORCA025 simulations with the standard viscosity (e.g. DRAKKAR Group 2014; Rühs et al. 2015) compared to observations, a

further reduction is not desirable and a viscosity of 0.6×10^{11} m^4s^{-2} does possibly not improve ORCA025 with respect to the global circulation. On very long time scales well above the ∼50 years investigated in this study, a negative impact of the reduced viscosity might also emerge in the STCC, communicated through the global-scale circulation. However, for the purpose of investigating the seasonal to decadal variations of EKE in the South Pacific STCC, V06H clearly benefits from the improved representation of the mesoscale velocities and a viscosity coefficient A_0^{lm} of 0.6×10^{11} m^4s^{-2} is used in all simulations with the ORCA025 configuration in the following section 4.

4 Decadal Variability of Eddy Kinetic Energy in the South Pacific Subtropical Countercurrent in an Ocean General Circulation Model

After establishing the suitability of the 1/4° ORCA025 configuration with a specifically adapted horizontal viscosity parameter for the investigation of the mesoscale in the subtropical South Pacific in the previous section, this section investigates the interannual and decadal variations of Eddy Kinetic Energy in the South Pacific Subtropical Countercurrent and its relation to the atmospheric forcing.

This section has been published in "Journal of Physical Oceanography":

*Rieck, J. K., C. W. Böning, and R. J. Greatbatch, 2018: Decadal Variability of Eddy Kinetic Energy in the South Pacific Subtropical Countercurrent in an Ocean General Circulation Model, Journal of Physical Oceanography, **48**, 757–771, doi:10.1175/JPO-D-17-0173.1.*

Abstract

The Eddy Kinetic Energy (EKE) associated with the Subtropical Countercurrent (STCC) in the western subtropical South Pacific is known to exhibit substantial seasonal and decadal variability. Using an eddy-permitting ocean general circulation model, which is able to reproduce the observed, salient features of the seasonal cycles of shear, stratification, baroclinic production and the associated EKE, we investigate the decadal changes of EKE. We show that the STCC region exhibits, uniquely among the subtropical gyres of the world's oceans, significant, atmospherically forced, decadal EKE variability. The decadal variations are driven by changing vertical shear between the STCC in the upper 300 m and the South Equatorial Current below, predominantly caused by variations in STCC strength associated with a changing meridional density gradient. In the 1970s, an increased meridional density gradient results in EKE twice as large as in later decades in the model. Utilizing sensitivity experiments, decadal variations in the wind field are shown to be the essential driver. Local wind stress curl anomalies associated with the Interdecadal Pacific Oscillation (IPO) lead to up- and downwelling of the thermocline, inducing strengthening or weakening of the STCC and the associated EKE. Additionally, remote wind stress curl anomalies in the eastern subtropical South Pacific, which are not related to the IPO, generate density anomalies that propagate westward as Rossby waves and can account for up to $30 - 40$ % of the density anomalies in the investigated region.

4.1 Introduction

During the last decade, it has become evident that a large fraction of variability in the global ocean is intrinsic in a sense that no interannual to decadal atmospheric variability is needed to drive oceanic variability on these time scales. Studies utilizing Ocean General Circulation Models (OGCMs) have shown this intrinsic variability to manifest itself in Sea Surface Height (SSH) variance (Combes and Di Lorenzo 2007; Penduff et al. 2011; Sérazin et al. 2015) as well as Eddy Kinetic Energy (Wilson et al. 2015). Even properties not directly related to the mesoscale such as the Atlantic Meridional Overturning Circulation (AMOC) (Grégorio et al. 2015), ocean heat content (Sérazin et al. 2017), and sea level trends (Sérazin et al. 2016) exhibit intrinsic variability.

Nevertheless, there are regions with lower intrinsic variability on interannual to decadal time scales. These regions are mainly, but not exclusively, located in the tropical oceans, where the ocean dynamics are relatively linear and largely depend on air-sea interactions (Penduff et al. 2011; Sérazin et al. 2015). Apart from these areas, the interior subtropical South Pacific (SP) exhibits relatively weak intrinsic variability of SSH at $\sim 30°$S compared to that found in the other subtropical oceans (Sérazin et al. 2015).

In the subtropical SP, the Subtropical Countercurrent (hereafter called STCC, Travis and Qiu 2017), initially called the South Tropical Countercurrent (Merle et al. 1969; Morris et al. 1996), is located between 25° and 33°S on top of the large scale gyre circulation. Contrary to the gyre circulation, which flows westward in the South Equatorial Current (SEC) at these latitudes, the STCC flows eastward, thereby creating a vertical shear of horizontal velocities. Similar current systems, associated with subtropical or similar fronts, can be found in the North Pacific (Kobashi and Kubokawa 2012) and the Indian Ocean (Menezes et al. 2014). The vertical shear in these systems is generally baroclinically unstable (e.g. Qiu 1999; Qiu and Chen 2004) and generates mesoscale variability.

Depending on the current systems, the mesoscale variability exhibits variability on different time scales. The North Pacific Subtropical Countercurrent, the STCC and parts of the South Indian Countercurrent (SICC) all have been shown to generate more mesoscale turbulence in summer than in winter (Qiu 1999; Qiu and Chen 2004; Jia et al. 2011b). These seasonal variations are driven by an increased meridional density gradient across the associated fronts in summer, inducing a stronger, surface

intensified current and thus enhanced shear with the underlying currents. The source of the increased meridional density gradient can be either dynamic or thermodynamic. In the South Pacific, Qiu and Chen (2004) argue for latitudinally dependent surface cooling to be the main factor in the STCC. However, Jia et al. (2011b) show Ekman and geostrophic flux convergence to be responsible in the SICC. The variability in countercurrent systems is not restricted to the seasonal time scales. The SICC has been shown to vary with a quasi-biennial period (Menezes et al. 2016) and interannually (Jia et al. 2011a) due to changes in the meridional density gradient driven by anomalous Ekman upwelling (Jia et al. 2011a), which they relate to changes in the wind field associated with the Southern Annular Mode. Qiu and Chen (2010) argue that the interannual variability in the North Pacific Subtropical Countercurrent is generated by surface heat flux forcing related to the Pacific Decadal Oscillation.

More recently, Travis and Qiu (2017) investigated the decadal variations of instability in the STCC region. The decadal changes are caused by a combination of variations of vertical shear of velocities, and stratification. Stronger (weaker) vertical shear and weaker (stronger) stratification both induce enhanced (decreased) instability. Travis and Qiu (2017) find the variability of vertical shear to be the dominant mechanism. However, they did not determine which factors ultimately drive the associated density changes observed in the STCC. Decadal variability in SP SSH has been shown to affect the large scale gyre circulation (Roemmich et al. 2016) as well as local EKE levels associated with the Tasman Front (Sasaki et al. 2008). Sasaki et al. (2008) show that basin scale wind stress curl variations related to decadal modulations in El Niño/Southern Oscillation (ENSO) drive the SSH and EKE changes. An influence on the STCC system and associated EKE can thus be expected.

In this study, the use of an OGCM enables us to extend our knowledge of the STCC and its variability due to a long study period of more than five decades and a deeper investigation of mechanisms. We show that the decadal variability of surface currents and EKE is related to atmospheric forcing rather than internal variability in the STCC region (section 4.3.1). Furthermore, we validate the mean state of the STCC and associated mesoscale variability from the OGCM in section 4.3.2 and in section 4.3.3 we show that the OGCM is able to reproduce the seasonal cycle of EKE. Then in section 4.3.4 we investigate the decadal variations, and in section 4.3.5 we investigate the role of the atmospheric forcing in the context of decadal variability associated with the Interdecadal Pacific Oscillation (IPO).

4.2 Model, Methods, and Data

This study is based on an eddy-permitting global ocean circulation model using a 1/4° configuration (ORCA025) based on the NEMO code (Madec et al. 1998) version 3.6, developed as part of the DRAKKAR collaboration. It is accompanied by an additional configuration (TROPAC01) with a refined grid in the South Pacific. As a base, TROPAC01 has a global 1/2° horizontal grid (ORCA05) and shares the vertical levels with ORCA025. Between 49°S−31°N in the Pacific, a grid with 1/10° resolution is nested into the ORCA05 grid using AGRIF (Adaptive grid refinement in FORTRAN; Debreu et al. 2008). TROPAC01 has been compared to observations in Czeschel et al. (2011) and van Sebille et al. (2014). For more information on TROPAC01, the reader is referred to Schwarzkopf (2016).

Hindcast experiments were performed with the two configurations from $1958-2009$ and $1960-2007$ for ORCA025 and TROPAC01, respectively. Comparing these hindcast experiments, it is shown that the ORCA025 configuration has about $60-70$ % of the mesoscale variability of TROPAC01 in the subtropical South Pacific (see section 4.3.4). Most importantly, ORCA025 is able to reproduce the relative amplitude of the decadal variability simulated in TROPAC01 (Fig. 4.1a and b and section 4.3.1 and 4.3.4). Thus, the several sensitivity experiments carried out as part of this study have been performed with the ORCA025 configuration.

The various ORCA025 configurations developed in recent years (DRAKKAR Group 2007, 2014) share the same global, orthogonal, curvilinear, tripolar Arakawa-C type grid with a nominal resolution of 1/4° in longitude. ORCA025 configurations have been widely used in studies investigating ocean variability mechanisms in different areas (e.g. Lübbecke et al. 2008; Lorbacher et al. 2010; Rühs et al. 2015) as well as influences of large scale atmospheric variability on the ocean (e.g. Feng et al. 2011; Ummenhofer et al. 2013; Barrier et al. 2015), and intrinsic oceanic variability on different time scales (Penduff et al. 2010; Sérazin et al. 2015).

The particular (Kiel) version of ORCA025 employed here uses 46 vertical levels with 6 m thickness at the surface, increasing towards ~ 250 m in the deep ocean and a partial-cell formulation at the bottom (cf. Barnier et al. 2006). The atmospheric forcing for the simulations from $1958-2009$ utilizes the bulk formulations and data products comprised in the Coordinated Ocean-Ice Reference Experiments (CORE.v2;

Experiment	length	wind stress forcing	buoyancy forcing
REF	$1958-2009$	full	full
CLIM	62 years	Normal Year	Normal Year
WIND	$1958-2009$	full	Normal Year
BUOY	$1958-2009$	Normal Year	full
IPOsim	28 years	IPO	Normal Year

Table 4.1: Length and forcing of the five main experiments, see section 4.2 for more details. More information on the experiments can be found alongside the data at http://data.geomar.de .

Griffies et al. 2009; Large and Yeager 2009). The CORE.v2 products are available for the period $1948-2009$, however, some forcing fields are climatological in the first decades of the forcing. Starting the simulations from 1958 thus constitutes a compromise between a long study period to investigate decadal variability and discarding the decades with highest uncertainty from the forcing. All model simulations apply a very weak sea surface salinity restoring (SSSR) to climatology of 33.33 mm day^{-1}, which corresponds to a relaxation time scale of 1500 days over a 50 m surface layer.

The model is spun up from rest with temperature and salinity from climatology (PHC2.1, updated from Steele et al. 2001) and an initial sea ice field from December 31st, 1992 from a previous ORCA025 simulation as this sea ice state fits the initial temperature and salinity fields. The model spin-up is forced for 30 years with the atmospheric forcing from $1980-2009$. The ocean state at the end of this spin-up period is then used as the initial condition for the hindcast simulations. Five experiments have been simulated in total: REF, CLIM, WIND, BUOY and IPOsim (Table 4.1).

REF ($1958-2009$) is the reference simulation with no changes to the forcing described above, to represent a realistic estimate of the simulated period. The CLIM simulation (62 years) with a repeating Normal Year (NY; Large and Yeager 2009) forcing is used to study the relative importance of intrinsic and forced variability. WIND ($1958-2009$) applies an interannually varying wind stress forcing in combination with climatological NY buoyancy forcing (heat and freshwater fluxes). WIND is accompanied by BUOY, which utilizes an interannually varying buoyancy forcing in combination with a NY wind stress forcing. The latter two experiments are intended to determine whether decadal variations in the STCC can be related to wind or buoyancy forcing from the atmosphere. The fifth experiment (IPOsim, 28 years) starts with 3 years of NY forcing.

For the following 10 years, the annual mean wind field of the NY forcing is replaced by a mean wind field representative of a negative state of the Interdecadal Pacific Oscillation (IPO), while keeping the synoptic variability and seasonal cycle of the NY forcing. This negative IPO phase is followed by 10 years where the mean wind field represents a positive IPO. The experiment concludes with 5 more NY forced years. The IPO phases are defined after the IPO Tripole Index (TPI), from Henley et al. (2015), to be the averaged wind field over $1970-1975$ and $1980-1985$ for the negative and positive phases, respectively. During the first and last year of the 10 year negative (positive) IPO phase, the mean wind field is linearly interpolated from the climatological state to the negative (positive) IPO state and back toward climatology, respectively.

EKE is defined to be EKE $= 0.5(u'^2 + v'^2)$, where $(u', v') = (u - \bar{u}, v - \bar{v})$. (u, v) are the 5 day mean zonal and meridional velocities at 93 m depth, respectively, and $(\bar{u}, \bar{v})$ are the one year mean horizontal velocities at 93 m depth. One year mean velocities $(\bar{u}, \bar{v})$ are used as to avoid interannual variations of the mean currents to be considered in the calculation of EKE. For further details on the calculation of EKE see Penduff et al. (2004) and Rieck et al. (2015). All investigations of near-surface circulation and EKE from the model output are performed at a depth of 93 m to exclude any ageostrophic circulation features, such as Ekman currents, that are present at the surface. To allow for the equilibration of EKE after the spin-up, the first two years of all hindcast experiments are discarded from use in the analysis (so that the periods used from REF, CLIM, WIND and BUOY are $1960-2009$).

All model output and the derived quantities have been detrended prior to any averaging applied. When monthly time series are shown, the climatological seasonal cycle has been removed as well. Unless otherwise stated, all temporal filtering has been performed with a simple Lanczos filter. A Boxcar filter has also been tested, but did not qualitatively alter the conclusion drawn from the presented results. After filtering with a five-year cut-off period, the first and last three years of the timeseries have been discarded from further analyses to avoid any boundary effects of the filter.

For validation of the reference simulation (REF), objectively analyzed monthly climatological temperature and salinity data on a $1/4^\circ$ grid, averaged over all available six decades from the World Ocean Atlas 2013 (WOA13.v2; Locarnini et al. 2013; Zweng et al. 2013) are used. From these temperature and salinity fields, potential density σ_0 is calculated and used to derive geostrophic velocities with a reference depth of

1500 m. Horizontal surface geostrophic velocities derived from sea surface height measurements by satellite altimetry, produced by SSALTO/DUACS and distributed by Archiving, Validation, and Interpretation of Satellite Oceanographic data (AVISO, http://www.aviso.altimetry.fr/duacs) are used to calculate observational surface EKE.

4.3 Results

4.3.1 Intrinsic and Forced Variability

A large part of the variability in the oceanic mesoscale, even on decadal time scales, is of an intrinsic nature and, therefore, cannot be related to changes in the forcing of the ocean (e.g. O'Kane et al. 2013, also see section 4.1). Thus, in order to detect significant, deterministic decadal changes of EKE and to attribute an atmospheric driver, the amplitude of these changes should be sufficiently large. Simultaneously, the intrinsic variability in the region should be relatively low, so as to minimize the possibility that the decadal changes in EKE are of an intrinsic nature. The intrinsic variability on decadal time scales is investigated by means of the ratio of intrinsic variance σ_i^2 to total variance σ_t^2 of EKE on decadal time scales (Fig. 4.1c and 4.2b).

Following Penduff et al. (2011): σ_i^2 is the variance of low-pass filtered annual mean EKE, filtered with a 5-year cut-off period, of the climatological run CLIM, where the atmosphere does not exhibit any variability on interannual to decadal scales. Thus, all decadal variability observed in CLIM's ocean must arise from processes internal to the ocean. σ_t^2 is the same variance of decadal EKE but from the simulation with interannual forcing variability (REF). If σ_i^2/σ_t^2 approaches one, most of the variability is generated internally. It should be noted that σ_i^2/σ_t^2 is only an estimate, as the intrinsic variability in REF can be different from the intrinsic variability in CLIM. It has been shown that interannual to decadal atmospheric variability is able to trigger modes of internal variability in the ocean (e.g. Taguchi et al. 2010; O'Kane et al. 2013), which are not accounted for in σ_i^2/σ_t^2.

Over most of the global ocean in REF, the standard deviation of EKE at 93 m depth on decadal time scales, σ_t, is about $10 - 40$ % of the mean EKE (Fig. 4.1). Outside the tropics, this is less than the part of variability that can be attributed to processes

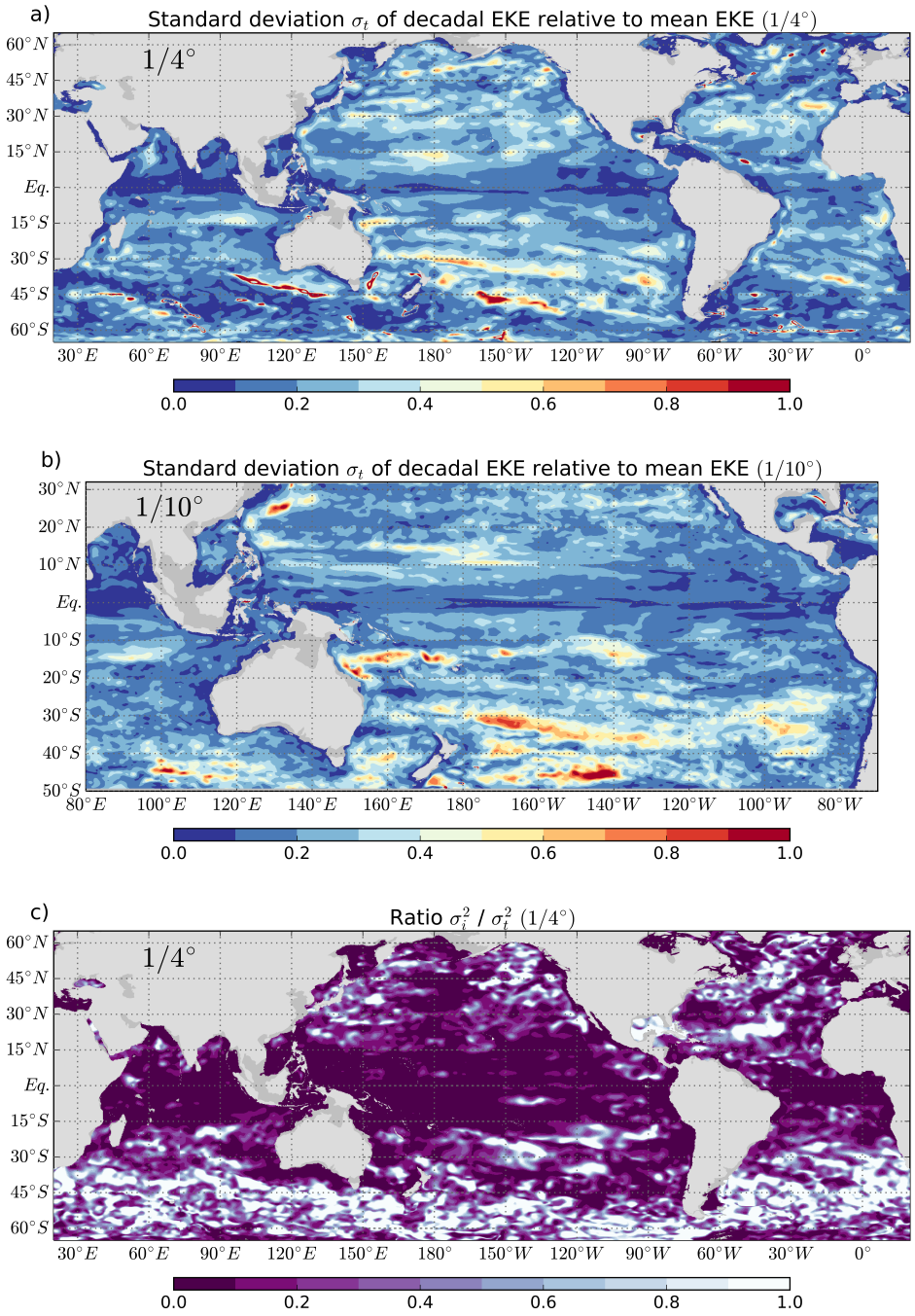

Figure 4.1: (a) The standard deviation of decadally smoothed EKE from ORCA025 (REF, $1963-2006$) at 93 m (a low-pass Lanczos filter with a 5-year cutoff period is used at every grid point), divided by the mean EKE (REF, $1963-2006$) at each grid point. A value of one indicates the amplitude of decadal EKE variations to be as large as the mean EKE, while a value close to zero depicts a grid point without significant EKE variability on decadal time scales. (b) As (a), but for the $1/10°$ resolution domain of TROPAC01. (c) The ratio of variance of decadally smoothed intrinsic EKE from CLIM (93 m depth, year $16-59$) to variance of decadally smoothed total EKE from REF (93 m depth, $1963-2006$) as described in section 4.3.1. A ratio of one indicates that all variability is intrinsic, while values close to zero show grid points where most of the variability is deterministic.

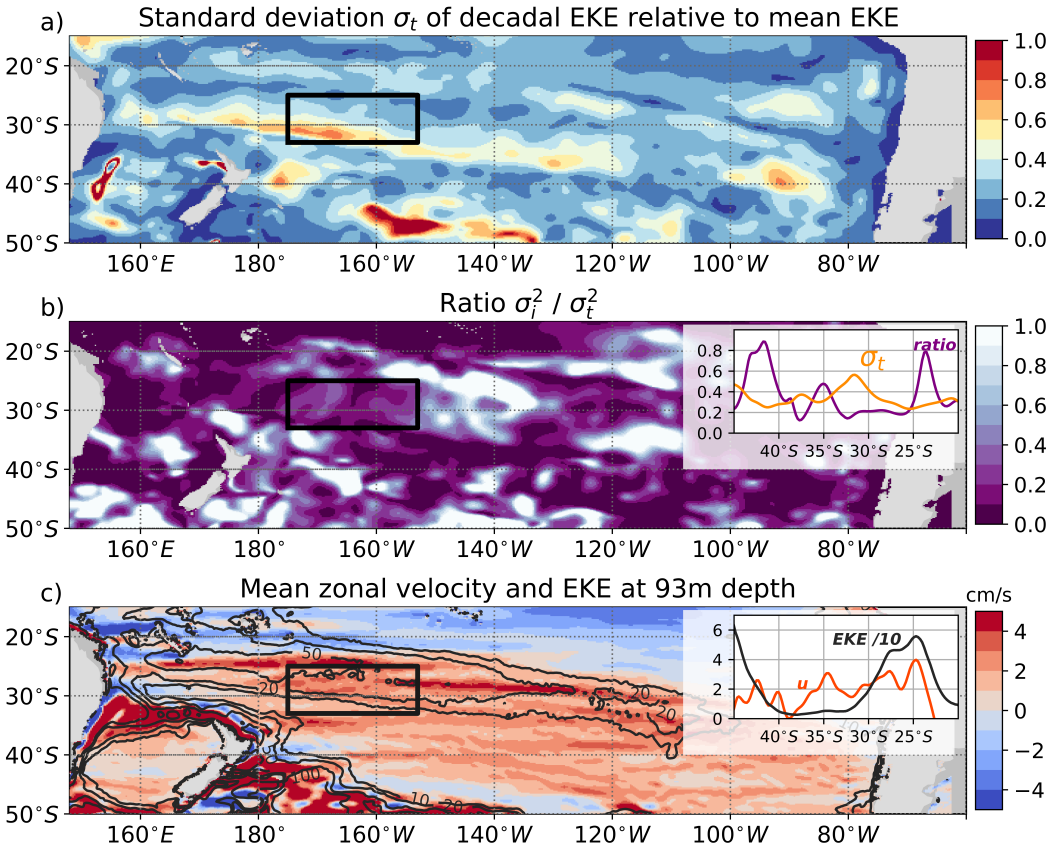

Figure 4.2: (a) As Fig. 4.1a but only showing the South Pacific. (b) As Fig. 4.1c but only showing the South Pacific. The small inset shows the zonal averages (averaged over the longitudes of the black box) of the standard deviation depicted in (a) (orange line) and the ratio depicted in (b) (purple line), both without units. (c) Mean zonal velocity in cm s^{-1} at 93 m depth from REF (shading). The zonal velocity is positive eastward. Overlying contours show EKE at 93 m from REF. Contour levels are 10, 20, 50, 100 cm^2 s^{-2}. The small inset depicts the zonal averages (averaged over the black box) of zonal velocity u (red line, cm s^{-1}) and EKE (black line, cm^2 s^{-2} divided by 10). In (a), (b) and (c) the black box indicates the region in which further investigations are conducted.

internal to the ocean. Poleward of 15°N and 15°S, the ratio of intrinsic to total variability σ_i^2/σ_t^2 is above 30 % on average (Fig. 4.1). Aside from western boundary currents and other strong current systems, the subtropical South Pacific is the only location in the world oceans where decadal variability with magnitude > 50 % of the mean is found along with a relatively low ratio σ_i^2/σ_t^2 (Fig. 4.1a and c, and 4.2a and b).

We focus further analyses on a box between $175 - 153$°W and $25 - 33$°S. The box is characterized by a large decadal variability of EKE, with σ_t between 30 and more

than 70 % of the mean EKE with a zonal mean maximum of 60 % at 31°S (Fig. 4.2a). At the same time, the ratio σ_i/σ_t of intrinsic to total variance of decadal EKE is low. σ_i/σ_t exhibits a local minimum, from < 0.1 to 0.3, with a zonal average of 0.2 (Fig. 4.2b). This combination of large decadal variability and a low ratio of intrinsic to total variability of EKE cannot be found to such an extent in any other subtropical ocean (Fig. 4.1a and c).

After establishing the exceptional properties of decadal EKE variability in the STCC region we now describe the mean state of the STCC region in detail, validate the model simulations against observations (sections 4.3.2 and 4.3.3), and then investigate the decadal variability of the EKE associated with the STCC (section 4.3.4) and the associated atmospheric forcing (section 4.3.5).

4.3.2 The Subtropical Countercurrent: Mean State

The near-surface circulation from REF in the subtropical South Pacific is dominated by the anti-clockwise subtropical gyre with broad eastward flow between roughly 30 and 45°S, and westward flow in the SEC between 15 and 30°S (Fig. 4.2c). Between 25 and 35°S, slanting southward towards the east, however, bands of eastward velocity are located above the SEC (Fig. 4.3a). These eastward velocities have a maximum of > 5 cm s^{-1} at 25°S and extend down to about 250 m between $25 - 33$°S. The SEC below has a maximum of 2.5 cm s^{-1} at 26°S and 600 m depth, the core of the SEC (5 cm s^{-1}), however, lies to the north between 21 and 22°S at $300 - 400$ m depth. While the core of the SEC and the northern edge of the STCC are located 2 to 3° further north in the geostrophic velocities derived from WOA13.v2 data, the overall structure of the current system compares well between the simulation and the observations (Fig. 4.3b). Larger differences can only be found in the southern branch of the STCC at 27 to 29°S, that is roughly 2 cm s^{-1} weaker in REF. The westward flow at depth is stronger in REF compared to WOA13.v2 inside the box, so that the vertical shear of horizontal velocities remains similar. One cause for this discrepancy could be the choice of the reference depth of 1500 m for the calculation of the geostrophic velocities.

The cause for the reversal of the horizontal flow with depth can be seen in the isopycnals shown in Fig. 4.3a and b. The meridional density gradient at depth is positive

to the north, associated with the westward SEC. At 600 m depth, however, the gradient reverses and in accordance with the thermal wind balance, the westward current weakens towards the surface, reversing at around 250 m. The induced vertical shear in horizontal velocity has been shown to be baroclinically unstable (Qiu and Chen 2004), resulting in a maximum of EKE at the latitude of the largest shear (25°S, Fig. 4.3a). The surface EKE from AVISO has a similar meridional distribution between 25 and 33°S, however, the magnitude of the EKE is roughly three times higher in AVISO than in REF (Fig. 4.3). Part of this difference can be accounted for by the fact that the EKE from the model is calculated at 93 m depth. Simulated EKE at the surface is twice as large as at 93 m depth on average in the STCC region (not accounting for possible ageostrophic contributions). Despite the EKE from satellite altimetry being still 50 % higher after accounting for this depth dependency, the 1/4° model is found to be suitable to investigate the temporal variations in EKE in the STCC region, as will be demonstrated in the following section.

4.3.3 Seasonal Cycle

Changes in stratification and vertical shear of horizontal velocities have been shown to cause decadal variations of baroclinic instability in the STCC region by Travis and Qiu

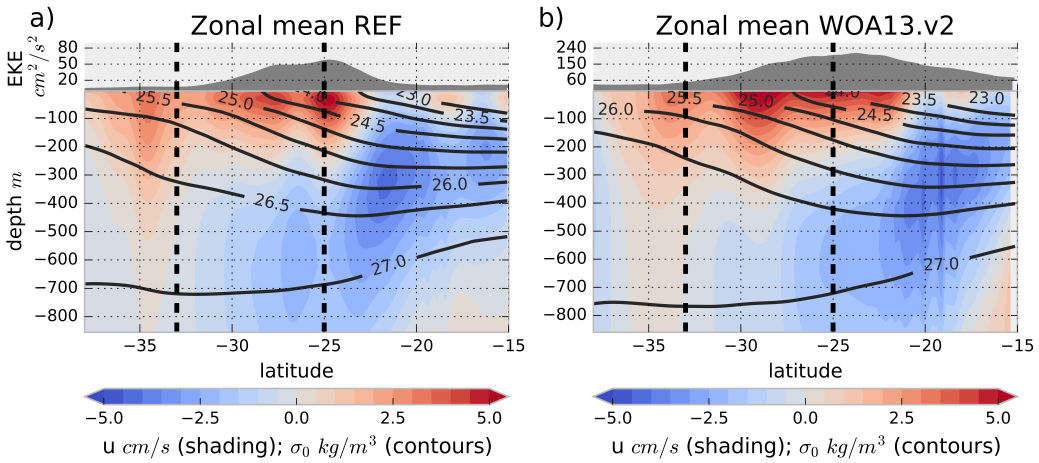

Figure 4.3: (a) Zonal mean velocity u in cm s^{-1} from REF, averaged from 1963 – 2006, against depth (shading). Positive values indicate eastward velocities. Overlying contours show density (σ_0) with contours every 0.5 kg m^{-3} from 23.0 – 27.0 kg m^{-3}. In the upper section, zonal mean EKE in cm^2 s^{-2} at 93 m depth is shown. All quantities shown are averaged over the longitudes of the black box shown in Fig. 4.2. (b) As (a), but for WOA13.v2 (u, σ_0) and AVISO (EKE) data. In (b), u are geostrophic velocities calculated with a reference depth of 1500 m.

(2017). Using observational data, they showed these variations to manifest themselves in decadal EKE variability. For the extended period from $1960-2009$ investigated in this study, it is not possible to verify the simulated fields of velocities and stratification against observations, because the data coverage from observations is not sufficient. Nevertheless, the simulations can be validated using the seasonal cycle of EKE. The seasonal cycle, similar to the decadal variability, is driven by changes in stratification and shear (Qiu and Chen 2004) that influence baroclinic instability.

To compare REF to observations, monthly climatological values are used. The vertical shear Δu of horizontal velocities in the region $175-153°$W and $25-33°$S is estimated using the difference between zonal velocity at 93 m and 628 m (100 m and 600 m) in REF (WOA13.v2). On average, Δu and the amplitude of its seasonal cycle are 0.1 cm s^{-1} larger in REF compared to observations (Fig. 4.4a and b). The phase of the seasonal cycle is similar though, with a minimum in April (April/May) and largest values in September and December (August and November) in the estimate based on observations (model).

The variations in stratification are estimated using the density difference $\Delta\sigma$ between the same depth levels as for the zonal velocities. Stratification is stronger in REF by 0.3 kg m^{-3} and the amplitude of the seasonal cycle is slightly larger in the observations (Fig. 4.4a and b). The phase of the seasonal cycle agrees well between model and observations with a minimum in June and a maximum in October. Given the seasonal cycles of Δu and $\Delta\sigma$, baroclinic instability should be stronger in austral spring/summer, compared to austral autumn/winter.

We estimate the strength of the baroclinic production mechanisms in the model by calculating $\overline{w'T'}$ as a measure of the energy transfer from the reservoir of Eddy Available Potenital Energy to EKE (Zhai and Marshall 2013), where $\overline{()}$ denotes the mean over all available data for each month and $()'$ denotes the 5-day mean deviation from the monthly climatology; w is the vertical velocity and T the potential temperature. For simplicity, potential temperature T is used here as an estimate for density fluctuations and the gravitational constant in the term $(\overline{w'\rho'}g)$ from Zhai and Marshall (2013) is neglected. Indeed, $\overline{w'T'}$ exhibits a clear seasonal cycle with a minimum in May and a maximum in October/November, followed by a minimum and maximum, respectively, in EKE with a lag of 1 to 2 months (Fig. 4.4c). A lag between $\overline{w'T'}$ and EKE is to

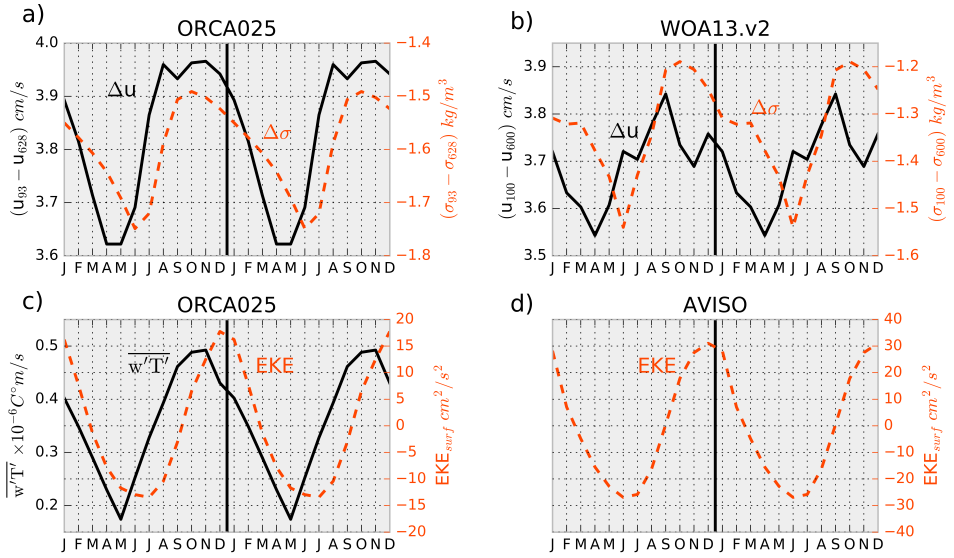

Figure 4.4: Climatological seasonal cycles averaged over $153 - 175°$W, $25 - 33°$S of: (a) Simulated (REF) zonal velocity difference Δu in cm s^{-1} between 93 m and 628 m (black solid line), and simulated (REF) density difference $\Delta\sigma_0$ in kg m^3 between 93 m and 628 m (red dashed line). (b) Geostrophic zonal velocity difference Δu in cm s^{-1} between 100 m and 600 m (black solid line), and density difference $\Delta\sigma_0$ in kg m^{-3} between 100 m and 600 m (red dashed line) based on WOA13.v2. (c) Simulated (REF) $\overline{w'T'}$ in 10^{-6} C° m s^{-1} averaged from 64 m to 322 m, and simulated (REF) surface EKE in cm^2 s^{-2}. (d) Observed (AVISO) geostrophic surface EKE in cm^2 s^{-2}. Note the different scales on the y axes of panels (a) and (b), and (c) and (d). For an easier interpretation of the results, the seasonal cycles are repeated once on the x-axis.

be expected because the instabilities require time to grow, depending on their growth rate. The EKE from AVISO has exactly the same phase as that from the model, however, the amplitude of the seasonal cycle is ~ 50 % larger than in the model (Fig. 4.4d). This could be partly due to the stronger stratification in the model and partly because the model's resolution is not high enough to simulate the whole spectrum of mesoscale, baroclinic instabilities.

Nevertheless, we have demonstrated that the ORCA025 model is capable of simulating baroclinic instabilities and their seasonal variability in the STCC. This gives confidence in the model's ability to simulate the correct timing of decadal changes of EKE, especially considering their dependence on large scale properties such as stratification and vertical shear of horizontal current systems. These decadal changes of EKE will be investigated in the next section.

4.3.4 Decadal Variability

The EKE in REF inside the box shown in Fig. 4.2 exhibits large variations on decadal time scales. After an increase in the late 1960s, the 1970s have an average EKE of 40 cm^2 s^{-2} (solid black curve in Fig. 4.5). EKE decreases again in the mid 1980s, levels off at 20 cm^2 s^{-2} and increases again in the 2000s. To illustrate the atmospherically forced nature of this variability, the variations of EKE from CLIM are shown in Fig. 4.5 to be less than 50 % of REF and to have a completely different phase. Comparing REF to the higher resolution configuration of the same model (1/10°, TROPAC01), mean EKE levels are 1.5 times higher in the higher resolution run, however, the relative peak to peak amplitude is ~ 100 % of the mean in both simulations, and both simulations show similar phases of EKE variations. Further investigation will be focused on the period $1971 - 1981$ and its anomalous, unique properties of the surface ocean.

In section 4.3.2 we demonstrated the importance of meridional density gradients to the STCC-SEC system and thus expect changes in these density gradients to influence the STCC and its EKE. Indeed, corresponding to the elevated EKE in the 1970s, there is a dipole of density anomalies in the sub-surface ocean (note that all anomalies are referenced to the period $1960 - 2009$). A positive density anomaly with a maximum of 0.1 kg m^{-3} is centred at 33°S and 300 m depth, co-located with a negative temperature anomaly of up to −0.6°C (Fig. 4.6a). Further to the north, at 25°S and 150 m depth, the density is about 0.1 kg m $^{-3}$ lower, compared to the mean. This negative anomaly

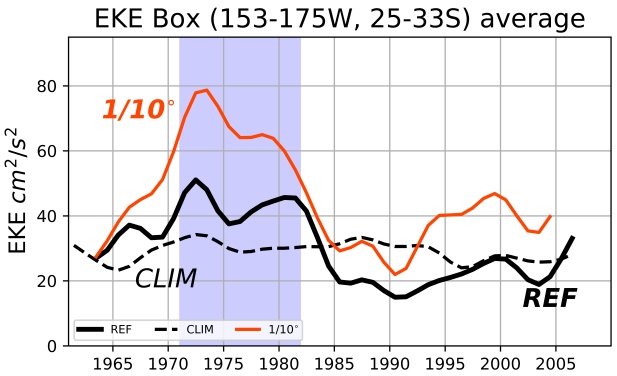

Figure 4.5: Time series of EKE (cm^2 s^{-2}) at 93 m depth averaged over the black box shown in Fig. 4.2 ($153 - 175$°W, $25 - 33$°S) for REF (solid black line), CLIM (dashed black line), and a 1/10° model (TROPAC01, solid red line)). All time series in the main plot have been filtered with a 5 year cutoff period. Blue, shaded area shows the anomalous period from 1971-1981.

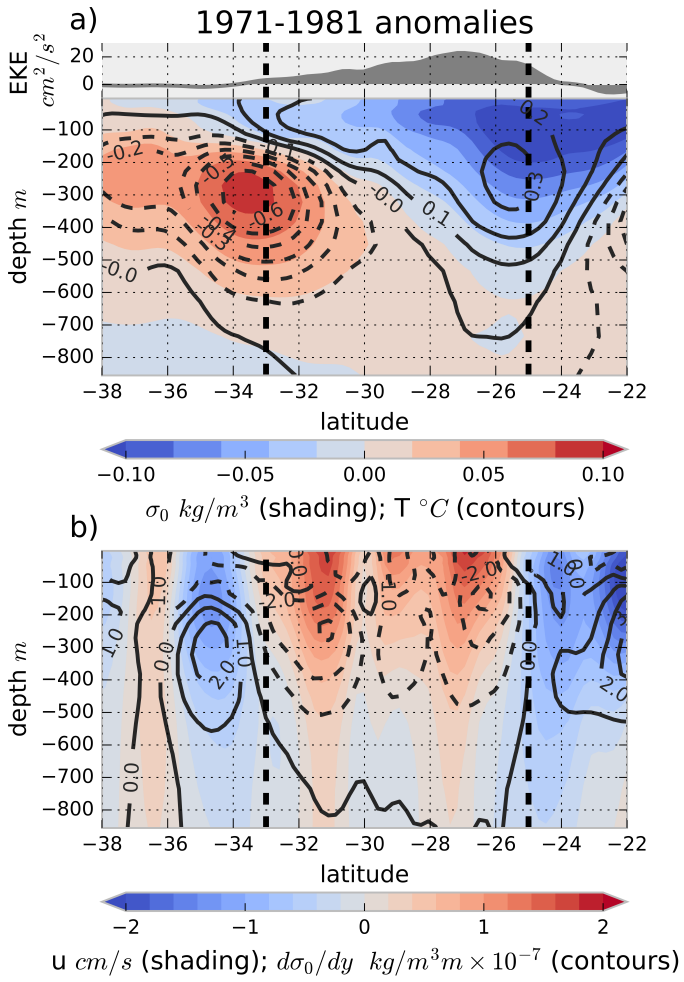

Figure 4.6: (a) $1971-1981$ anomaly of zonal mean density σ_0 (REF) against depth (shading). Overlying contours show temperature anomalies with contours every 0.1°C from -0.6 to 0.3°C. In the upper section, the zonal mean EKE anomaly at 93 m depth is shown. (b) $1971-1981$ anomaly of zonal velocity u in cm s^{-1} against depth (shading). Overlying contours show the anomalous zonal mean meridional density gradient $d\sigma_0/dy$. Negative values indicate an increased southward density gradient. Contours are shown every 1×10^{-7} kg m^{-3} m^{-1} from -3 to 3×10^{-7} kg m^{-3} m^{-1}. All quantities shown are averaged over the longitudes of the black box shown in 4.2 ($153-175$°W). Anomalies are calculated with respect to the 1960-2009 mean.

is supported partly by a positive temperature anomaly of 0.3°C centred at 26°S, 250 m depth. Closer to the surface, at the northern boundary of the box, salinity also plays a role in determining the strength and structure of this density anomaly (Fig. 4.7).

This anomalous dipole structure steepens the slope of the isopycnals and thus increases the meridional density gradient, especially between 200 and 300 m depth (Fig. 4.6b). This results in surface-intensified eastward current anomalies of up to 2 cm s^{-1} at the latitudes of the strongest increase in the density gradient (27 and 31°S) arising from the increased vertical shear, resulting in a baroclinically more unstable current system as already illustrated by Qiu and Chen (2004) for seasonal time scales and Travis and Qiu (2017) for decadal time scales. Fig. 4.8 illustrates the decadal variations of the vertical shear Δu and $\overline{w'T'}$ as an indicator for the baroclinic instability. During $1971-1981$, Δu exhibits a $20-30$ % increase with respect to the mean and accordingly, $\overline{w'T'}$ is $40-50$ % larger. This additional baroclinic instability in turn leads to intensified mesoscale variability and elevated EKE in the upper ocean.

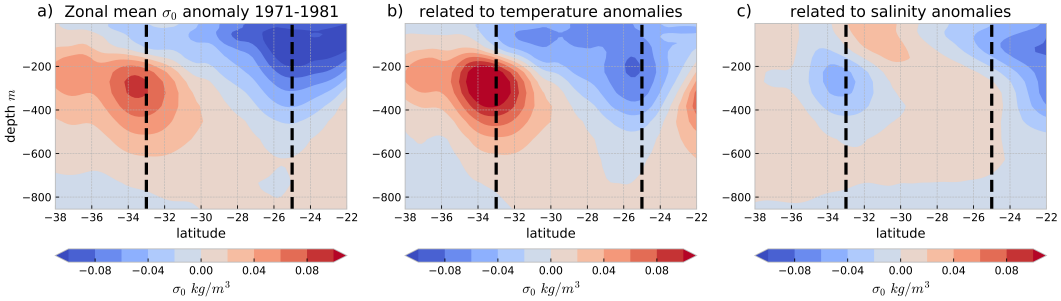

Figure 4.7: (a) $1971-1981$ anomaly of zonal mean density σ_0 (REF) against depth (shading). (b) Density σ_0 calculated from mean salinity and anomalous temperature to illustrate the effect of temperature anomalies on the density distribution. (c) Density σ_0 calculated from mean temperature and anomalous salinity to illustrate the effect of salinity anomalies on the density distribution. All quantities shown are averaged over the longitudes of the black box shown in Fig. 4.2 ($153-175$°W), the latitudes of the box are indicated by the vertical, dashed black lines. Anomalies are calculated with respect to the $1960-2009$ mean.

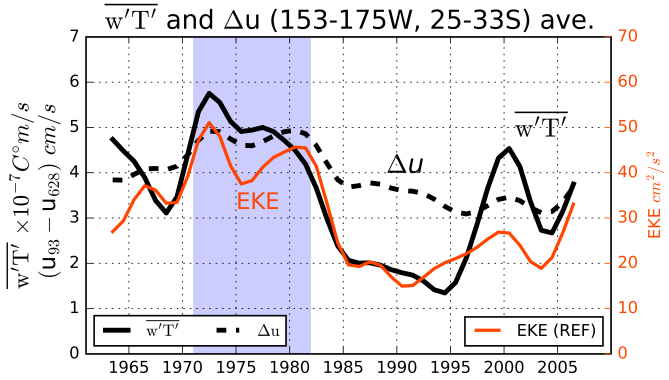

Figure 4.8: Time series averaged over $153-175$°W, $25-33$°S of simulated (REF) $\overline{w'T'}$ in 10^{-7} C° m s^{-1} averaged from 64 m to 322 m (solid black line), simulated (REF) zonal velocity difference Δu between 93 m and 628 m depth in cm s^{-1} (dashed black line), and simulated (REF) EKE in cm^2 s^{-1} at 93 m depth (solid red line.)

4.3.5 The Role of Wind and the Interdecadal Pacific Oscillation

To determine whether the subsurface temperature anomalies are caused by variations in buoyancy or momentum fluxes at the atmosphere-ocean interface, the two model runs BUOY and WIND are used. It can be clearly seen in Fig. 4.9 that BUOY exhibits only minor decadal variability, while WIND is able to reproduce the decadal variability of EKE found in REF. BUOY shows a minimum of around $25 - 30$ cm ^{2} s^{-2} in the 1970s, when WIND and REF have EKE of approximately $40 - 50$ cm^2 s^{-2}, followed by a slow increase towards $30 - 40$ cm^2 s^{-2} in BUOY, when WIND and REF show a minimum of $15 - 25$ cm^2 s^{-2}, in the 1980s and 90s. The decadal variability in BUOY is of the same order of magnitude as in CLIM and could thus be of intrinsic nature. After establishing the essential role of the wind forcing for variations of the STCC and EKE, the responsible mechanisms will now be explored.

From Fig. 4.10, it can be seen that the density anomalies at depth (322 m, the depth at which the anomalies are strongest) are related to wind stress curl anomalies at the surface to a certain extent. The positive wind stress curl anomaly in the early 1970s triggers anomalous downwelling between 26 and 38°S. This leads to density anomalies at depth, with the maximum in the thermocline, where the vertical temperature gradient is strongest. Anomalies in salinity can also be observed, although they are not dominant in determining the density structure (cf. Fig. 4.7).

In the late 1970s, a negative anomaly in wind stress curl then induces upwelling from $\sim$ 28°S toward the south. The maximum negative temperature anomaly is located slightly deeper then the positive anomaly further north (Fig. 4.6), as the strongest vertical gradient in temperature, i.e. the thermocline, is located deeper at these latitudes. As there are no associated anomalies on density surfaces (not shown), both these temperature anomalies are of an adiabatic nature as expected for anomalies associated to wind driven upwelling and downwelling.

Interestingly, the positive subsurface density anomaly in the early 1970s and the negative density anomaly in the late 1970s are both shifted northward with respect to the related wind stress curl anomalies by roughly 3° latitude (Fig. 4.10), rather than being located directly beneath the wind stress curl anomalies, where the upwelling and downwelling should occur. The most obvious reason for that 3° shift is the propagation of density anomalies into the region from the east. These anomalies are generated

in the eastern South Pacific ($110 - 120°$W, $25 - 33°$S), where local wind stress curl anomalies generate subsurface density anomalies (Fig. 4.11). In contrast to the wind stress curl anomalies in the western part of the basin, these anomalies occur on time scales shorter than five years. To focus on the influence of these interannual anomalies, but at the same time exclude shorter, more synoptic variability, the density anomalies in Fig. 4.11 have been band-pass filtered to include only variability on time scales of $2 - 5$ years. The density anomalies propagate westward at a speed of ~ 6 cm s^{-1}, arriving in the box investigated ($153 - 175°$W) after roughly two to three years. This propagation speed lies within the observed range of Rossby wave propagation speed at these latitudes from satellite altimetry (e.g. Chelton and Schlax 1996).

Sub-decadal density anomalies at $153 - 164°$W and $164 - 175°$W are correlated to the wind stress curl forcing in the eastern part ($110 - 120°$W) with a lag of 28 and 40 months, respectively (correlation coefficients -0.38 and -0.30, both significant at the 95 % level). More precisely, a negative density anomaly of up to -0.03 kg m^{-3} arrives in the box in the early 1970s, supporting the negative anomaly generated by the local wind stress curl forcing. In 1975, a strong positive anomaly of 0.03 kg m^{-3} is arriving at the same time the local wind stress curl forcing switches from positive to negative. Comparing the magnitudes in Fig. 4.10 and Fig. 4.11 it is obvious that, in the 1970s, between 30 and 40 % of the local density anomalies can be explained by signals arriving in the western basin, that originate from further east.

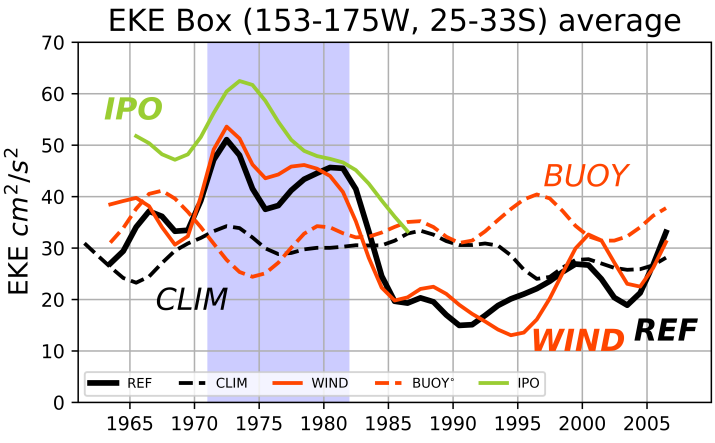

Figure 4.9: Time series of EKE at 93 m depth averaged over the black box shown in Fig. 4.2 ($153 - 175°$W, $25 - 33°$S) for REF (solid black line), CLIM (dashed black line), WIND (solid red line), BUOY (dashed red line), and IPOsim (green line). Blue, shaded area shows the period over which anomalies are averaged.

In the 1980s and early 1990s, both the local (in the western part) and eastern wind stress curl anomalies are weak (associated density changes are < 0.03 kg m^{-3}) and do not induce any significant changes in current strength and EKE (Fig. 4.9). The late 1990s and 2000s exhibit a weak increase in EKE, which is associated with strengthened local and remote (eastern) wind stress curl anomalies. However, the local wind stress curl anomalies exhibit a second maximum at $\sim 35°$S in contrast to the 1970s, when a minimum occurred at this latitude (Fig. 4.10). In combination with a negative density anomaly arriving from the east around the year 2000 (Fig. 4.11), this results in meridionally almost uniform subsurface density anomalies that do not change the meridional gradient significantly.

The decadal variability of the large-scale wind field over the South Pacific can to a large degree be understood in terms of the Interdecadal Pacific Oscillation (IPO). The wind stress curl at 33°S between 153 and 175°W is correlated to the IPO index with a

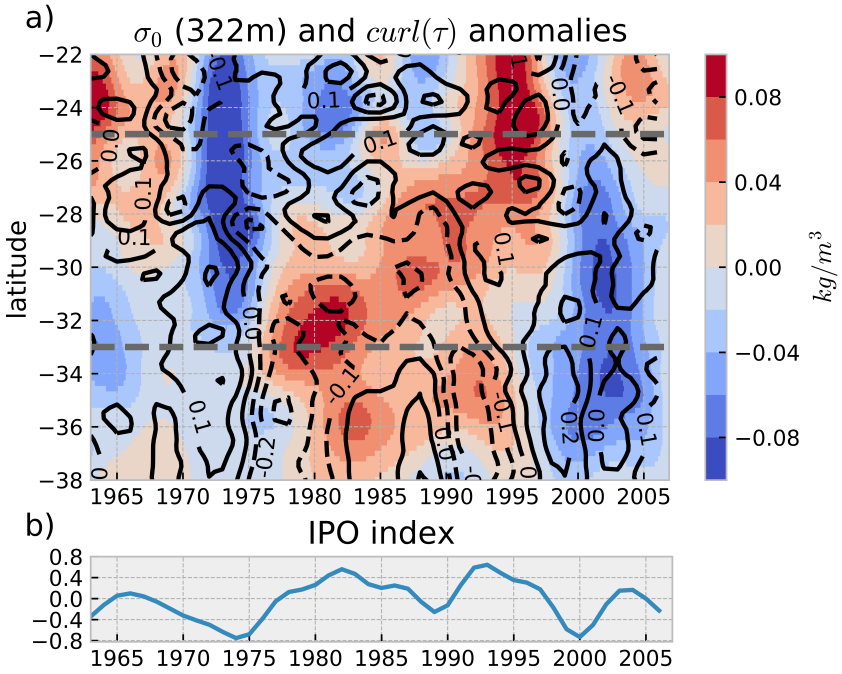

Figure 4.10: (a) Zonal mean density (σ_0) anomalies at 322 m depth (averaged over the longitudes of the black box shown in Fig. 4.2, the latitudinal extent is indicated here by the dashed grey lines.) over time (shading). Overlying contours depict wind stress curl anomalies. Contours are drawn every 0.1×10^7 N m^{-2} from -0.3 to 0.3×10^7 N m^{-2}. Anomalies are calculated with respect to the $1960-2009$ mean, detrended and filtered with a 5-year cutoff period Lanczos filter. (b) IPO index (from Henley et al. (2015)) filtered with a 5-year cutoff period Lanczos filter.

correlation coefficient of -0.34 at time scales > 5 years (also compare Fig. 4.10a and b). To investigate the role of the IPO in forcing the simulated changes in the STCC, the simulation IPOsim as described in section 4.2 is used. In Fig. 4.9, the green line shows the temporal evolution of EKE in the box in IPOsim to be quite similar to the REF and WIND cases. There is a strong increase in EKE in the early 1970s and a slow decrease afterwards, until the end of the IPOsim simulation. However, the second peak in EKE in the late 1970s is not captured in the IPOsim run. This is due to a weaker negative wind stress curl anomaly at the southern edge of the box in IPOsim, thus the meridional density gradient is not reinforced. This might be caused by the transition time between the negative and positive IPO phases. The IPOsim simulation uses wind fields from completely negative and positive IPO phases and does not fully account for the transition between these. In reality, the transition might be much more complex than the linearly interpolated attempt presented here, thus possibly explaining the differences between WIND and IPO.

The question arises, why EKE does not increase in a similar fashion in the 2000s, when the IPO again is in a negative phase. In addition to the meridional structure of the density anomaly in the 2000s, which is different from the 1970s due to a different structure of the local wind stress curl anomaly, and also the effect of density anomalies arriving from the east (Fig. 4.10 and 4.11), a second explanation can be brought forward. While the magnitude of the negative IPO phase in the 2000s is about as large as in the 1970s, the duration is much shorter. In the early decades, the IPO is in a mostly negative phase in the 1960s, the index is then slowly decreasing until 1975 and then abruptly increasing, reaching positive values in 1977. This results in more than 10 years of negative IPO forcing. Around the year 2000, the IPO index becomes negative in 1998, reaching its minimum in 2000 and shows positive values already in 2002, resulting in only 4 years of negative IPO forcing. Thus, the response of EKE is much weaker, though nonetheless present, around 2000 with a short peak in the late 1990s, early 2000s.

In summary, the IPO seems to set the large-scale background wind field that either favours or suppresses the increase of STCC strength through the induced anomalies of the meridional density gradient. However, additional factors are needed to ultimately set the strength of the STCC and EKE levels. In the 1970s, wind stress curl anomalies in the eastern basin aid with the generation of density anomalies, that propagate to the west and make up $30 - 40$ % of the observed anomalies in the western basin.

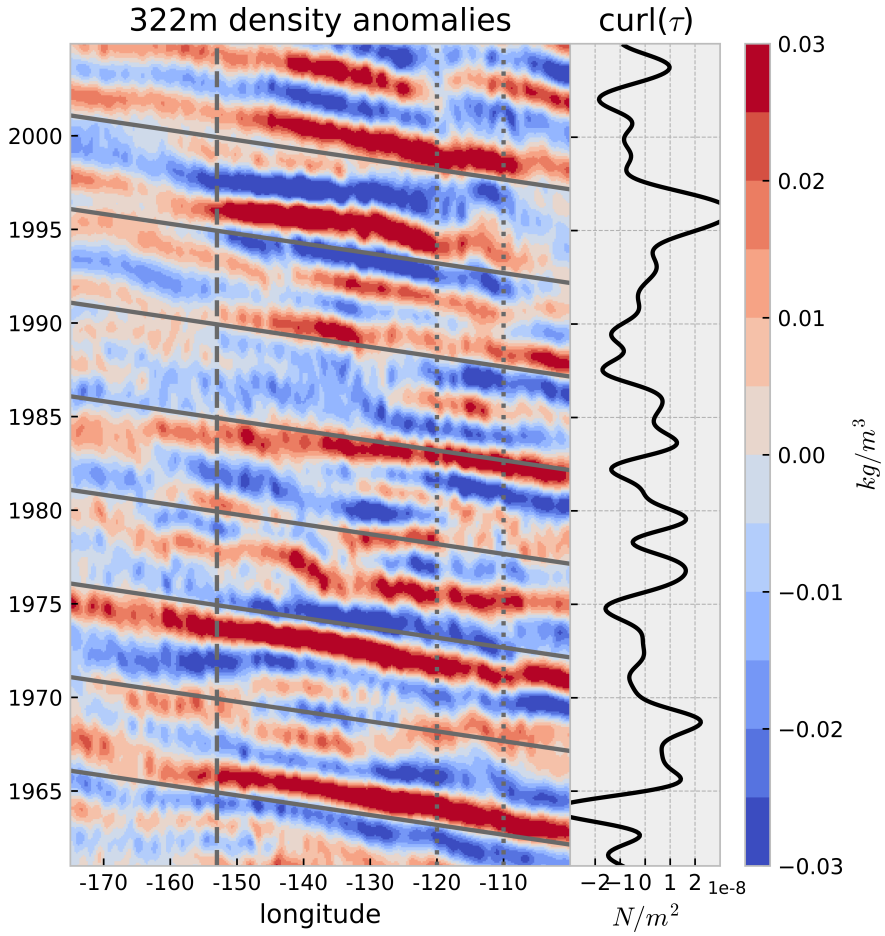

Figure 4.11: Meridional mean density (σ_0) anomalies (averaged over the latitudes of the black box shown in Fig. 4.2 whose longitudinal extent is indicated by the dashed grey line) at 322 m depth over time. Grey solid lines represent the theoretical path of an anomaly propagating westward with speed of 6 cm s^{-1}, which is in the range of observed speeds for Rossby waves at these latitudes (Chelton and Schlax 1996). The solid, black line in the right panel depicts the wind stress curl anomaly averaged over $110-120°$W, $25-33°$S (indicated by the two vertical dotted, grey lines). Density and wind stress curl are band-pass filtered, only retaining periods of $2-5$ years. Anomalies are calculated with respect to the $1960-2009$ mean.

These eastern wind stress curl anomalies are not associated with the IPO (correlation coefficient between the IPO index and wind stress curl averaged over $110-120°$W, $25-33°$S is 0.02).

4.4 Summary and Conclusion

Using an eddy-permitting global ocean general circulation model, we investigate a band of decadal variability of near-surface EKE in the subtropical South Pacific ($175 - 153°$W, $25 - 33°$S). This region exhibits, as a unique feature among the subtropical gyres of the world's oceans, significant, atmospherically forced, decadal EKE variability. Over most of the other subtropical oceans, decadal variations of EKE are small and masked by processes internal to the ocean.

The investigated region contains a vertically sheared current system, consisting of the eastward Subtropical Countercurrent in the upper 300 m and the westward South Equatorial Current below. As shown by previous studies based on observations (Qiu and Chen 2004), and confirmed in this study, this vertical shear in horizontal velocities is maintained by the meridional density gradient across the STCC and the current system is baroclinically unstable, resulting in a local maximum of near-surface EKE. The 1/4° OGCM is able to reproduce the salient features of the seasonal cycles of EKE, baroclinic instability and its two causes, vertical shear and stratification.

Based on the fact that decadal variations in EKE are driven by changes in vertical shear and stratification (Travis and Qiu 2017), we investigated the decadal variability of EKE. In the STCC region ($175 - 153°$W, $25 - 33°$S) EKE shows decadal variations of over 100 % of the mean, with a maximum in the 1970s, which is unmatched in the rest of the simulated period. The phase and amplitude of this decadal variability is supported by findings from a 1/10° resolution configuration of the same model, as well as other model studies. For example Sasaki et al. (2008) show similar variability of EKE in a region nearby in their 1/10° OGCM.

As the meridional density gradient sets the strength of the STCC and its mesoscale variability, anomalies in this density gradient are the cause for changes in near-surface EKE. In the 1970s, a dipole of a negative density anomaly in the STCC region and a positive anomaly just to the south increases the meridional density gradient. These anomalies are focused at thermocline depth where the vertical density gradient is strongest, and are dominated by temperature changes which, through the thermal wind balance, result in stronger vertical shear and associated baroclinic production of the STCC-SEC system.

Utilizing sensitivity experiments, we show interannual and decadal variability of the wind field to be the essential driver of changes in the STCC, while changes in air-sea heat and freshwater fluxes are negligible contributors. Positive (negative) anomalies in the large scale wind stress curl over the STCC drive downwelling (upwelling) in the 1970s that results in anomalies in the subsurface density field and its meridional gradient. While most of the decadal variations of the wind stress curl are related to the IPO (supported by another sensitivity experiment), other local and remote wind stress curl variability significantly influences the density field in the STCC region. $30 - 40$ % of the density anomalies in the 1970s can be explained by interannual variability, propagating into the region from the east, modulating the decadal signal of the IPO.

These interannual density anomalies are correlated to the wind stress curl at $110 - 120°$W at the same latitude and show no relation to the IPO. They propagate at a speed of ~ 6 cm s^{-1}, identifying them as long baroclinic Rossby waves (cf. Chelton and Schlax 1996). Travis and Qiu (2017) also find Rossby waves to propagate into the STCC region, explaining part of the SSH variability observed, even though Qiu and Chen (2006) predicted the Rossby waves dynamics to break down in this particular region.

In the 1980s and early 1990s, a positive phase of the IPO prevails and causes an extended period of very low EKE levels. In the late 1990s/2000s, differences in the structure and strength of the local wind stress curl anomalies and the westward propagating density anomalies suppress a response of the STCC to the negative phase of the IPO. Additionally, the later, negative IPO phase is much shorter than the earlier phase, not allowing for a full adjustment of the ocean. Accordingly, there are only minor similarities between the early (1970s) and late (1990s/2000s) negative phases of the IPO.

The STCC region uniquely demonstrates how large-scale, interannual and decadal atmospheric variability can manifest itself in variations of the oceanic mesoscale. At the same time, this study shows a complex interplay of local and remote, interannual and decadal changes in the wind field and associated oceanic variations, not always allowing for a direct attribution of a forcing to its consequences. Nevertheless, given the STCC's connection to the IPO, a behaviour similar to the 1970s can be expected in the future, if the IPO switches into a negative phase for a prolonged period. With more in-situ and remote sensing systems in place today, current and future changes

in the STCC can also be observed and used to validate the presented modelling efforts. Additionally, improved models and better observational coverage can be used to investigate the implications of the decadal changes of EKE in the STCC. The STCC is located in close proximity to a region of subduction (e.g. Tsubouchi et al. 2007; Li 2012). Thus, changes in currents, mesoscale variability and thermocline structure could influence the subduction and spreading of water masses and tracers.

5 The Nature of Eddy Kinetic Energy in the Labrador Sea: Different Types of Mesoscale Eddies, their Temporal Variability and Impact on Deep Convection

The second region of interest in this thesis is the Labrador Sea in the subpolar North Atlantic. The Labrador Sea is thought to play a major role in the Meridional Overturning Circulation (MOC) by forming parts of the Labrador Sea Water (LSW), an important water mass in the lower limb of the Atlantic MOC. Deep convection is a key process in the formation of LSW and mesoscale eddies impact this deep convection. While the 1/4° configuration used in the previous section can be tuned to realistically simulate the oceanic mesoscale in the subtropics, it is impossible to achieve this in the Labrador Sea. In the Labrador Sea, the model's horizontal resolution has to be at least 1/12° to sufficiently resolve the first baroclinic Rossby radius of deformation (Hallberg 2013), which is necessary to simulate mesoscale eddies. Therefore, a 1/4° global configuration with a high-resolution 1/20° nest embedded in the North Atlantic is used in this section to investigate the mesoscale eddies and their variability in the Labrador Sea.

This section has been submitted to "Journal of Physical Oceanography":

Rieck, J. K., C. W. Böning, and K. Getzlaff, 2019: The Nature of Eddy Kinetic Energy in the Labrador Sea: Different Types of Mesoscale Eddies, their Temporal Variability and Impact on Deep Convection, submitted to the Journal of Physical Oceanography.

Abstract

Oceanic eddies are an important component in preconditioning the central Labrador Sea (LS) for deep convection and in restratifying the convected water. This study investigates the different sources and impacts of Eddy Kinetic Energy (EKE) and its temporal variability in the LS with the help of a 52-year long hindcast simulation of a 1/20° ocean model. Anticyclonic Irminger Rings (IR) with warm and saline cores are generated in the West Greenland Current (WGC) between 60 and 62°N by baroclinic and barotropic instabilities. The IR exhibit a seasonal cycle and decadal variations linked to the WGC strength, which varies with the large scale circulation of the subpolar gyre. The IR have an

effect on preconditioning and limit the northward extent of the convection area, but only intermittently contribute to the restratification in spring. The main source of EKE and restratification in the central LS are Convective Eddies (CE) generated by baroclinic instabilities near the bottom of the mixed layer during and after convection. The CE have a mid-depth velocity core and reflect the temperature and salinity properties of the convected water mass with a distinct minimum in potential vorticity. Their seasonal to decadal variability is tightly connected to the local atmospheric forcing and the associated air-sea heat fluxes. A third class of eddies in the LS are the Boundary Current Eddies shed from the Labrador Current (LC). Since they are mostly confined to the vicinity of the LC, these eddies appear to exert only minor influence on preconditioning and restratification.

5.1 Introduction

The Labrador Sea (LS) in the western subpolar North Atlantic is one of the few regions in the world's oceans where deep convection occurs on a regular basis. Large air-sea heat fluxes, sometimes exceeding 1000 W m^{-2}, during the winter months cause the surface waters to loose buoyancy until the stratification of the water column is overcome and deep convection is triggered (e.g. Marshall and Schott 1999). The strength of the stratification is the limiting factor that usually prevents deep convection and thus a preconditioning of the LS is required. In this context preconditioning refers to a cyclonic large scale circulation with upward doming isopycnals at its center causing a weakly stratified thermocline and a weak stratification in the near-surface ocean. Over the past two to three decades, numerous studies on the basis of observations and numerical simulations suggested that oceanic eddies play a major role in determining both the location and strength of deep winter convection and the subsequent restratification of the convected water mass during spring and summer. Eddies can hinder deep convection by transporting heat and freshwater toward the interior, thereby increasing the stratification in the central LS.

Three types of eddies can be identified in the LS:

5.1.1 Irminger Rings

Irminger Rings (IR) originate in the West Greenland Current (WGC) at the west coast of Greenland between $61 - 62°$N (Heywood et al. 1994; Brandt et al. 2004; Zhang and Yan 2018). Near Cape Desolation (48.10°W, 60.44°N), the WGC encounters steep topography that induces instabilities, leading to the generation of the anticyclonic IR.

The nature of these instabilities is not fully understood to date. While earlier studies with Ocean General Circulation Models (OGCM) found barotropic instabilities (BT) to be the main driver (Eden and Böning 2002; Chanut et al. 2008), simulations with idealized numerical models pointed to baroclinic instabilities (BC) near the bottom (Katsman et al. 2004; Bracco et al. 2008). More recently Luo et al. (2011) also found near-bottom BC to be the major driver in an OGCM, while Zhu et al. (2014) point out the importance of both types of instabilities in their OGCM.

The IR have diameters of $30 - 60$ km, a relatively warm core (Lilly et al. 2003) and propagate towards the West and Southwest with a speed of $3 - 6$ cm s^{-1} (Katsman et al. 2004; Chanut et al. 2008; Zhang and Yan 2018). Mixing with the surrounding water in the northern LS increases the stratification there, effectively prohibiting deep convection (Chanut et al. 2008). Whether or not IR also aid in rapidly restratifying the central LS after the convection period is a matter of ongoing debate. Some studies find IR to have relatively little effect on the rapid restratification in spring (Chanut et al. 2008; Zhang and Yan 2014) while others point to a shared importance of IR and other sources (Gelderloos et al. 2011) or even attribute a major role in this process to the IR (Katsman et al. 2004). Part of these discrepancies can possibly be explained by the difficulties of many models to simulate the convective region at the right location. Often it is simulated too far north (e.g. Saenko et al. 2014) in the westward path of the IR.

The EKE maximum generated near Cape Desolation exhibits a seasonal cycle with a maximum in winter (January to March; Lilly et al. 2003; Brandt et al. 2004; Zhang and Yan 2018) in accordance with the winter maximum of the WGC velocity in that region. On interannual time scales the variations of EKE and IR in the WGC are less well understood. Brandt et al. (2004) speculate that the density gradient between the central LS and the boundary current is responsible for a stronger WGC and thus EKE, which is supported by a model study by de Jong et al. (2016). Zhang and Yan (2018) attribute the changes to the strength of the Subpolar Gyre (SPG) circulation.

5.1.2 Convective Eddies

Convective Eddies (CE) are thought to originate from the rim-current along the boundary of the convective patch driven by the large lateral buoyancy gradient between the convected water and its surroundings (Gascard and Clarke 1983; Marshall

and Schott 1999). Theoretical and idealized numerical studies show the rim-current to be baroclinically unstable and to generate cyclonic and anticyclonic CE (Send et al. 1995; Jones and Marshall 1997; Lilly et al. 2003). However, the few CE which have been observed were exclusively anticyclonic (Lilly et al. 2003). Their diameter ranges from $10 - 36$ km and maximum velocities of $0.1 - 0.3$ m s^{-1} are found at mid-depth around a core containing water from within the convective area, usually cold and fresh compared to the surroundings. In OGCMs with sufficiently high resolution, EKE generation is often found in the central LS (Chanut et al. 2008; Luo et al. 2011; Zhu et al. 2014), however CE have not yet been described in detail in a simulation with realistic geometry and forcing.

Due to their close proximity to the convective region, CE are supposed to play a role in the quick restratification in spring. However, as with IR, their relative importance is debated. Gelderloos et al. (2011) attribute only minor restratifying effects to the CE, while Chanut et al. (2008) find them to be essential for the restratification right after convection. The importance of CE for the central LS is underlined by float observations between 1000 and 1500 m depth showing EKE at these depths to dominate over surface EKE in most of the convection region (Fischer et al. 2018).

The seasonal variability of CE is dictated by the seasonal cycle of convection, making EKE in the central LS strongest in early spring (March, April; Brandt et al. 2004; Luo et al. 2011; Zhang and Yan 2018). However, most studies do not explicitly investigate CE, so that the variability could also arise from mesoscale features propagating into the region (Brandt et al. 2004). The interannual variations in CE generation are thought to be linked to the strength of deep convection (Lilly et al. 2003; Brandt et al. 2004).

5.1.3 Boundary Current Eddies

Boundary Current Eddies (BCE) are generated in Labrador Sea's boundary currents, the WGC and the Labrador Current (LC) (Chanut et al. 2008). At the eastern boundary, BCE are generated between the southern tip of Greenland and Cape Desolation. Most of the BCE at the western boundary are generated between 56 and 60°N along the shelf (Eden and Böning 2002; Brandt et al. 2004), with a pronounced maximum in winter when the boundary currents are strongest. BCE originate from baroclinic

instabilities of the WGC and LC, are surface intensified, and generally do not propagate far from the boundary (Chanut et al. 2008). However, in the western LS, the convection area is situated close to the LC. An impact of the BCE on the convection could thus be possible.

5.1.4 Objectives

The mesoscale variability of the LS is far from understood in all its details. While the general properties of the different types of eddies in the LS are well defined, there is still a lack of explanations for some of the generation mechanisms, as well as their relative importance for preconditioning and restratification. We address these questions by combining three important aspects in one simulation: a high-resolution (1/20°) ocean model, in realistic geometry, run over a 52-year period with forcing from a well-established reanalysis product. Using a realistic instead of an idealized geometry is expected to yield a better representation of the locations and timings of convection and mesoscale activities. The higher resolution compared to earlier studies with OGCMs (e.g. Zhu et al. 2014) improves the representation of the different types of eddies in the LS. The long hindcast simulation enables us to investigate temporal variations beyond interannual time scales. This is important as, especially near strong currents, a large part of the temporal variability of the mesoscale is intrinsic to the ocean, i.e. not attributable to a certain atmospheric forcing (Sérazin et al. 2015; Rieck et al. 2018), even at interannual time scales.

After describing the model, data, and methods in section 5.2, we focus on investigating the properties, generation mechanisms, and potential impact on deep convection of Irminger Rings (section 5.3.1), Convective Eddies (section 5.3.2), and Boundary Current Eddies (section 5.3.3), summarizing and discussing the results in section 5.4.

5.2 Model, Data, and Methods

This study utilizes a global ocean general circulation model based on the Nucleus for European Modelling of the Ocean (NEMO) code version 3.6 (Madec 2008), developed as part of the DRAKKAR collaboration. The ocean component of NEMO is based on Océan PArallélisé (OPA; Madec et al. 1998), while the sea-ice compo-

nent is the Louvain-la-Neuve Ice Model version 2 (LIM2; Fichefet and Maqueda 1997; Vancoppenolle et al. 2009). The specific configuration used here, VIKING20X, is an extended and updated version of VIKING20. It has been built on the experiences with VIKING20 in simulating various aspects of the subpolar North Atlantic, ranging from the Denmark Strait overflow (Behrens et al. 2017) and the circulation in the Deep Western Boundary Current (Fischer et al. 2015; Handmann et al. 2018) to the flow field along the North Atlantic Current (Mertens et al. 2014; Breckenfelder et al. 2017) and the influence of Greenland meltwater on the Labrador Sea (Böning et al. 2016). VIKING20X consists of a global, orthogonal, curvilinear, tripolar Arakawa-C type grid with a nominal resolution of $1/4°$ in longitude, which is refined to $1/20°$ in the Atlantic between 34°S and 70°N using AGRIF (Adaptive grid refinement in FORTRAN; Debreu et al. 2008). Both the base model and the refined nest share the same 46 vertical levels with 6 m thickness at the surface, increasing towards a maximum of 250 m in the deep ocean and a partial-cell formulation at the bottom (Barnier et al. 2006).

An atmospheric forcing based on the Coordinated Ocean-Ice Reference Experiments (CORE.v2; Griffies et al. 2009; Large and Yeager 2009) along with the associated bulk formulations is used. The model is spun up from rest with temperature and salinity from climatology (PHC2.1; updated from Steele et al. 2001) and an initial sea ice field from 31 December 1992 from a previous $1/4°$ simulation. The 30 year spin-up period is forced by the interannually varying atmospheric forcing for the period $1980 - 2009$. A snapshot of the oceanic state at the end of this spin-up is then used as initial state for the hindcast simulation from $1958 - 2009$. The model simulation applies a weak sea surface salinity restoring (SSSR) to climatology of 33.33 mm day^{-1}, which corresponds to a relaxation time scale of 1500 days over a 50 m surface layer.

Preliminary tests showed the lateral boundary condition to be a critical aspect to the simulation of IR in the WGC. Accordingly, a no-slip condition is implemented in the WGC ($43 - 51°$W, $59 - 62°$N) to represent the topographic effect on the current necessary to produce instabilities that generate IR, while the model uses a free-slip condition elsewhere. The reliance of the generation of IR on this no-slip condition is exploited to study the impact of IR on deep convection in the central LS. An additional sensitivity simulation differing only in the definition of a free-slip lateral boundary condition in the WGC is forked off the hindcast on 1 January 2007 and run for three years with the same atmospheric forcing.

The influence of resolution on CE in the central LS is investigated by comparing the 1/20°-behavior with a 1/12° simulation (ORCA12) which is driven by the same forcing as the 1/20° hindcast, for the period 1 January 1980 to 31 December 1991. Allowing for a short spin-up phase, the years $1983-1991$ are compared to the 1/20° simulation.

EKE is defined to be $EKE = 0.5\overline{(u'^2 + v'^2)}$, where $(u', v') = (u - \bar{u}, v - \bar{v})$. (u, v) are the 5 day mean zonal and meridional velocities, respectively. The mean velocities $(\bar{u}, \bar{v})$ are based on one year averages to avoid interannual current variability to be considered EKE (cf. Penduff et al. 2004; Rieck et al. 2015). The observational estimate for EKE is derived from the gridded, delayed time geostrophic surface velocities made available by E.U. Copernicus Marine Service (CMEMS) and calculated as described above. Additionally, 1 Hz along-track sea level anomaly (SLA) data developed, validated, and distributed by the CTOH/LEGOS, France (X-TRACK; Birol et al. 2017) are used in the Labrador Sea (Topex/Poseidon, Jason-1/2/3, Track 72), to account for the underestimation of EKE derived from gridded SLA products at high latitudes (Zhang and Yan 2018). The SLA is low-pass filtered with a ∼40 km cutoff LOESS filter and EKE is calculated from the across-track geostrophic velocity, derived from the along-track SLA gradient. To compare the modeled EKE to this observational value, daily mean simulated SLA are sub-sampled with a nearest-neighbor lookup to the times and locations of the satellite-derived SLA and then treated identically.

To estimate the respective contribution of baroclinic and barotropic instabilities to the generation of EKE, the energy transfer terms are considered (Wright 1981; Böning and Budich 1992; Zhu et al. 2014). Baroclinic instability can be described in terms of the transfer from mean to Eddy Potential Energy:

$$T_2 = -\rho_0 (\frac{g}{N\rho_0})^2 (\overline{u'\rho'}\frac{\partial\bar{\rho}}{\partial x} + \overline{v'\rho'}\frac{\partial\bar{\rho}}{\partial y})$$

$\rho_0 = 1025$ kg m^3 is the reference density, N^2 is the annual mean Brunt-Väisälä-Frequency $N^2 = -(g/\rho_0)(\partial\sigma/\partial z)$ with σ being the simulated density and z the depth, u' and v' are the horizontal velocity anomalies with respect to (u, v) low-pass filtered with a boxcar window of length 100 days. Analogously, ρ' is the density anomaly. Barotropic transfer is expressed as the work of the Reynolds stresses against the mean shear:

$$T_4 = -\rho_0 (\overline{u'^2}\frac{\partial\bar{u}}{\partial x} + \overline{v'^2}\frac{\partial\bar{v}}{\partial y} + \overline{u'v'}(\frac{\partial\bar{u}}{\partial y} + \frac{\partial\bar{v}}{\partial x}))$$

Both terms, T_2 and T_4, must be considered approximations in this context, as they only represent energy conversions when integrated over a closed volume. When considering subregions as done in this study, advection of energy by the mean flow or the mean eddy advection and divergence of the pressure work can influence T_2 and T_4 (Böning and Budich 1992). Nevertheless, the two terms can be used to address the relative importance of baroclinic and barotropic instability, and their temporal and spatial variability is a useful measure to contrast times and regions of higher instability to those of lower instability.

Decadal changes of the circulation of the SPG are indicated by the SPG index calculated following Berx and Payne (2017) and Hátún and Chafik (2018) as the principal component of the first Empirical Orthogonal Function (EOF) of the Sea Surface Height in the subpolar North Atlantic between 40 and 65°N.

5.3 Results

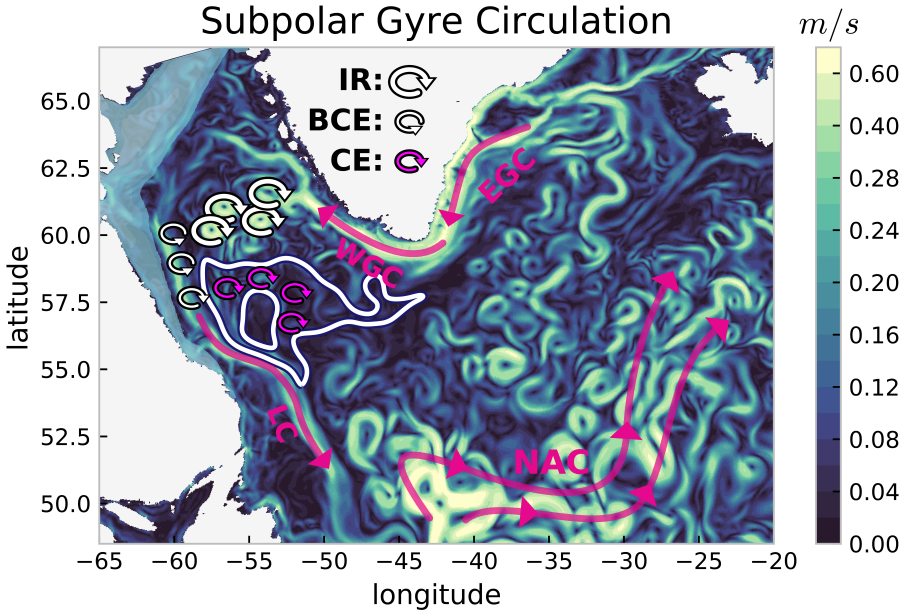

Figure 5.1: Snapshot (5-day mean field) of horizontal current speed at 94 m depth in the western subpolar North Atlantic. Arrows schematically indicate the positions of the major surface currents. Circular arrows illustrate the areas where Irminger Rings (large, white circular arrows), Boundary Current Eddies (small, white circular arrows), and Convective Eddies (small, pink circular arrows) occur. The white contours in the Labrador Sea indicate the 600 and 1000 m contours of the 2000 – 2009 mean March mixed layer depth.

The model simulation is well representing the features of the circulation in the subpolar North Atlantic. Figure 5.1 illustrates the geographical distribution of the near-surface currents in the region of interest. The North Atlantic Current (NAC) along with the Northwest Corner at ∼45°W, 50°N stands out as a swath of vigorous eddying motions. The boundary current system in the western subpolar gyre is comprised of the East Greenland Current (EGC), the WGC and the LC. Different types of eddies are expected to be found in the central LS: the Irminger Rings in the northern LS, the Convective Eddies in the central LS around the region of deep convection, and the Boundary Current Eddies. In the following sections the simulated characteristics of these three types of eddies are studied.

5.3.1 Irminger Rings

The 1/20° simulation is well resolving the large anticyclonic (negative relative vorticity) eddies originating in the WGC near Cape Desolation (Fig. 5.2). Relative vorticity is calculated from 5 day mean velocities as $\zeta = dv/dx - du/dy$. The WGC can be seen along the west coast of Greenland between Cape Farewell and 61°N with positive vorticity offshore of the current and negative vorticity towards the coast. Additionally, three IR can be clearly observed between 60 and 62°N. Relative vorticity in this snapshot is generally elevated between 48 − 58°W, 59 − 62°N with absolute values $> 0.4\ \mathrm{s}^{-1}$, while it is below $0.1\ \mathrm{s}^{-1}$ in the region where convection occurs (indicated by the March Mixed Layer Depth, MLD).

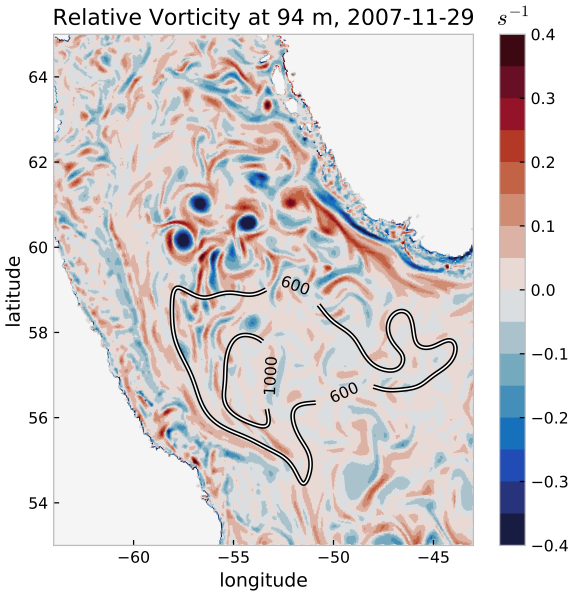

Figure 5.2: Snapshot (5-day mean) of simulated relative vorticity ζ (s^{-1}; shading) at 94 m depth in November 2007 in the Labrador Sea. Contours for 600 and 1000 m depict the 2000 − 2009 mean March Mixed Layer Depth, horizontally smoothed with a ∼300 km boxcar filter.

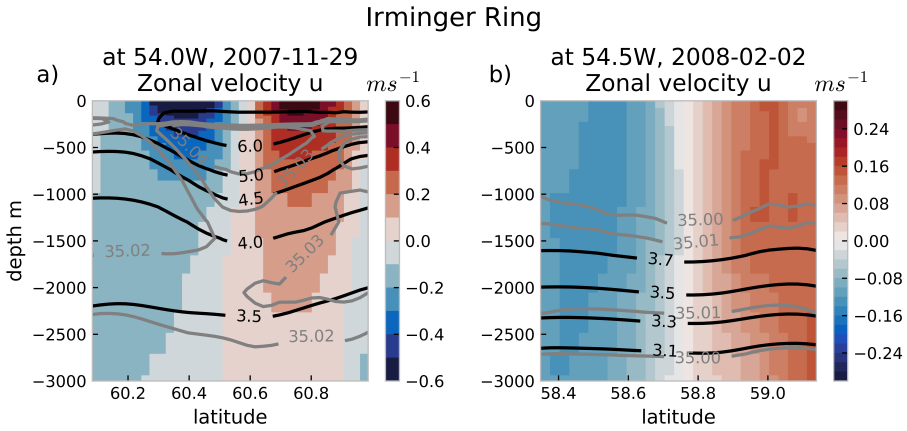

Figure 5.3: Meridional sections through an Irminger Ring, showing zonal velocity (shading) in m s^{-1}, temperature (black contours) in °C, and salinity (gray contours). (a) located at 56.5°W, 61.1°N on 29 November 2007 and (b) located at 54.5°W, 58.8°N on 02 February 2008

Sections through one of these IR at 56.5°W, 61.1°N in Fig. 5.2 are shown in Fig. 5.3a. It compares favorably with observations (Hátún et al. 2007; de Jong et al. 2014), exhibiting a surface intensified structure with velocities well above 0.4 m s^{-1} in the upper ocean, a warm and saline core with anomalies compared to the surroundings of up to 0.5°C and 0.02, respectively, and a fresh cap in the upper $100 - 200$ m. Another Irminger Ring (Fig. 5.3b) has significantly different properties in the upper ∼1000 m about 2 months later. While propagating further south (58.8°N) it has experienced convection and displays nearly homogeneous temperature and salinity in the upper 1000 m, as well as a weaker, more barotropic velocity structure (0.2 m s^{-1}). This compares well with observations of IR in the central LS, that do not show the fresh cap observed further north (Lilly et al. 2003).

The integrated effect of the IR is shown in Fig. 5.4a. An EKE (at 94 m depth) maximum of more than 250 cm^2s^{-2} near the coast of Greenland between 60 and 62°N is extending towards the west and southwest as a result of the IR propagation into the interior. The location of this maximum compares well with EKE calculated from gridded SLA data from satellite altimetry (Fig. 5.4b). The EKE in the model, however, is about twice as large as in observations. This discrepancy, at least partly, arises due to the inability of gridded SLA data to resolve mesoscale variability at high latitudes (Zhang and Yan 2018). When comparing EKE based on higher resolution along-track SLA data to the simulated EKE, the discrepancy is significantly reduced (Fig. S1).

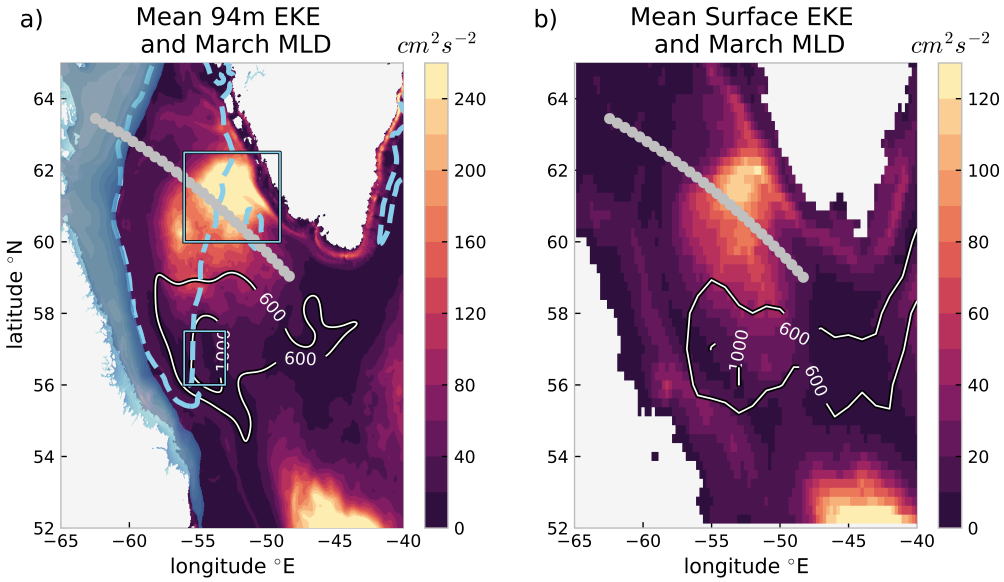

Figure 5.4: (a) Simulated $2000-2009$ mean 94 m Eddy Kinetic Energy (cm^2s^{-2}; shading), March mixed layer depth (contours at 600 and 1000 m), 250 W m^{-2} March heat loss contour(dotted, light blue), and March sea ice cover (light blue shading). The two boxes show the regions used for investigations of EKE in the WGC area and the central LS. (b) as (a) but for surface geostrophic EKE from altimetry and MLD from ARGO. Note the different color scales for (a) and (b).

The most important effect of the IR is the limitation of deep convection to the southern central LS. While winter heat loss is large over most of the central LS, deep convection, approximated by the mean March MLD, only occurs south of 59°N due to the stratifying effect of the IR further north. The location of the deepest MLD around 55°W, 57°N in the model also compares well to MLD from ARGO float observations (Fig. 5.4) for the period $2000-2009$, although the extent of the convective area appears to be overestimated, especially northwest of $55°W$, 58°N. For the MLD from ARGO, the variable threshold method is used (Holte et al. 2017) as a threshold method is also used in the model simulation.

The hypothesis that IR mainly affect the preconditioning is additionally supported by a sensitivity study that aims to reduce the number of IR shed from the WGC. A free-slip lateral boundary condition is implemented at the west coast of Greenland, whereas in the hindcast simulation a no-slip condition is used. Free-slip reduces the lateral shear near the boundary, and thus significantly weakens the EKE generation by the local instabilities in the WGC (Fig. 5.5a). As a result, almost no IR are shed in this simulation and in consequence a reduced stratification in the northern central LS can be seen, with the mean MLD of March 2008 up to 1000 m deeper than in the simulation with IR (Fig. 5.5b).

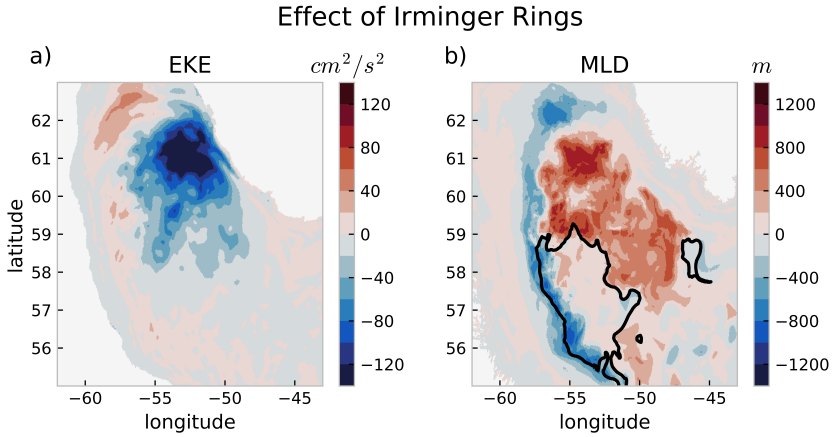

Figure 5.5: Differences between the simulation without IR (free-slip) and the one with IR (no-slip) for (a) Mean 2008 EKE (94 m depth) in $\mathrm{cm^2 s^{-2}}$ and (b) Mean March 2008 MLD. The black contour in (b) showing the area where the March 2008 MLD is greater than 989 m in the simulation with IR. See section 5.2 for a description of the two simulations.

Arguably, the elimination of all IR is not a realistic scenario. Nevertheless, Fig. 5.5 illustrates the impact of the IR on the lateral extent of deep convection in the central LS. It also shows that the response of the northern central LS MLD to a reduced number of IR is rather quick. Thus, a connection between the IR shed from the WGC and the MLD in the northern central LS can be expected even though the changes in EKE due to realistic variations in the forcing are much smaller compared to the sensitivity study above.

5.3.1.1 Temporal Variability

We first investigate the seasonal cycle of EKE in the WGC, as this is observationally well constrained and can be used to test the model's ability to simulate the temporal variability of the instability processes occurring near Cape Desolation. A box ranging from $49 - 56°\mathrm{W}$, $60 - 62°\mathrm{N}$ (cf. Fig. 5.4) is chosen to average the EKE maximum off the WGC. The simulated EKE peaks in February at 200 $\mathrm{cm^2 s^{-2}}$ and 140 $\mathrm{cm^2 s^{-2}}$ in the upper ($112 - 322$ m depth) and the deeper ($382 - 1655$ m depth) ocean respectively (Fig. 5.6), which compares well with observations (Brandt et al. 2004) and other model studies (Luo et al. 2011). The two energy conversion terms T_2 and T_4 described in section 5.2, averaged from $49.5 - 52.0°\mathrm{W}$ and $60.0 - 61.5°\mathrm{N}$, are used to approximate the baroclinic (BC) and barotropic (BT) instability processes. Both BC and BT

exhibit a similar seasonal variability in the upper and deeper ocean, peaking in winter. The BC in the deeper ocean is the largest of the instability processes and peaks in January at 4.6×10^{-5} kg m^{-1}s^{-3}, while BC in the upper ocean has its maximum of 2.6×10^{-5} kg m^{-1}s^{-3} in November. Barotropic instabilities in the upper ocean evolve similarly to BC in the deeper ocean with a maximum (3.0×10^{-5} kg m^{-1}s^{-3}) in January. BT in the deeper ocean is low ($0.5-1.0\times10^{-5}$ kg m^{-1}s^{-3}) throughout the year and does not show a pronounced seasonal cycle. Generally, BC in the deeper ocean appears as the major instability process at work, with BT in the upper ocean and BC in the deeper ocean combined exhibiting a similar magnitude. Of the two latter processes, BT in the upper ocean is the larger contributor, except for early winter, when BC in the upper ocean reaches similar values. These findings are in general agreement with previous idealized model studies (Katsman et al. 2004; Bracco et al. 2008) and more recent studies using OGCMs (Zhu et al. 2014), and deviate from earlier model studies (Eden and Böning 2002; Chanut et al. 2008).

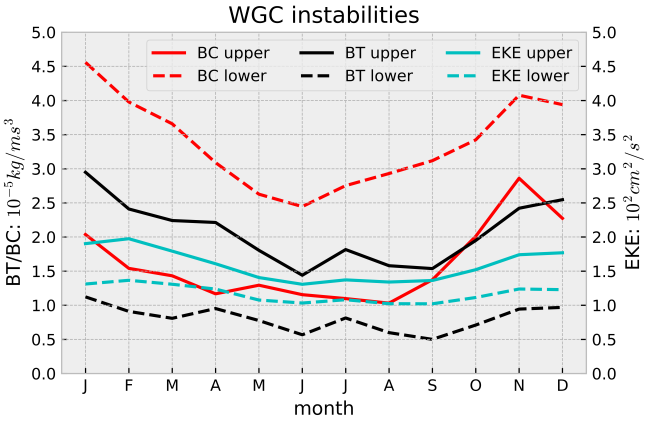

Figure 5.6: Mean simulated climatological seasonal cycle of EKE (cyan lines, 10^2 cm^{2}s^{-2}), BC (red, 10^{-5} kg m^{-1}s^{-3}), and BT (black, 10^{-5} kg m^{-1}s^{-3}) in the West Greenland Current ($49-56$°W, $60-62$°N for EKE and $49.5-52.0$°W, $60.0-61.5$°N for BC and BT). Solid lines depict the upper ocean ($112-322$ m), dashed lines the deeper ocean ($382-1655$ m).

After establishing the models ability to produce instabilities around Cape Desolation with a seasonal variability that supports the simulated and observed seasonal cycle of EKE, we now focus on variations on longer time scales. As the ocean integrates the high frequency atmospheric forcing into lower frequency variability of the general circulation, links between year-to-year variations in the atmosphere and large-scale ocean circulation are hard to detect. In fact, oceanic EKE variability is largely intrinsic, i.e. internally driven, in most regions on interannual time scales (Wilson et al. 2015; Rieck et al. 2018), which might explain the difficulties previous studies had relating the interannual EKE variability in the WGC to an external forcing (e.g. Luo et al. 2011). In the following, we thus focus on variations on decadal time scales.

A Subpolar Gyre (SPG) index is defined as described in section 5.2 to indicate periods of stronger and weaker circulation in the North Atlantic subpolar gyre (Fig. S2). Based on this index, the two periods $1966-1975$ and $1988-1997$ are chosen, representing weak (SPG-) and strong (SPG+) circulation in the SPG, respectively.

During SPG+, the boundary currents of the LS are significantly stronger compared to SPG- (Fig. 5.7a). The WGC is additionally more confined to the shelf. The current velocity averaged from $382-1655$ m depth reduces offshore, while the velocity closer to the shelf increases by more than 10 cm s^{-1}. A first assumption is that BT and BC increase in response to the increased strength of the boundary current. However, the interaction of velocity and instabilities is more complex. More precisely, BT in the upper ocean decreases by more than 5×10^{-5} kg $m^{-1}s^{-3}$ between 60.0 and 60.5°N, where the velocity increase is strongest, and increases by a similar amount further downstream, north of 60.5°N (Fig. 5.7d). Similarly, BC in the deeper ocean decreases by more than 5×10^{-5} kg $m^{-1}s^{-3}$ at the shelf between 60.0 and 60.5°N and increases by more than 10×10^{-5} kg $m^{-1}s^{-3}$ further downstream where the velocity increase is strongest in this depth range (Fig. 5.7c). The behaviour of the instability processes during SPG+ influences the generation of EKE. In accordance with BT and BC, EKE decreases by up to 40 cm^2s^{-2} during strong WGC circulation east of 50°W and south of 61°N, while it increases by more than 60 cm^2s^{-2} in a large area further downstream and offshore (Fig. 5.7).

Three boxes have been chosen to further investigate the processes in the WGC. Box 1 ($47.0-49.3$°W, $59.5-60.7$°N) encompasses the region where, despite stronger velocities, the instabilities are reduced during SPG+. Box 2 ($49.5-52.0$°W, $60.0-61.5$°N) is the area with stronger instabilities during SPG+ and Box 3 ($52.5-57.0$°W, $60.0-61.5$°N) is located offshore in the path of the IR to capture the variations of EKE in response to a stronger SPG. Generally, EKE and BT act in concert in one region, while BC has a larger influence on downstream EKE. For long time scales (timeseries are smoothed with a 5-year running mean), the EKE in Box 2 is positively correlated to BT in the same box (0.68) and to BC in the upstream Box 1 (0.72), all correlations are significant at the 95%-level. However, neither EKE and BT in Box 2, nor BC in Box 1 are correlated to the SPG index, indicating that, even at long time scales, much of the EKE generation is chaotic and only when averaging over decades, an effect can be seen (Fig. 5.7). Further downstream, BC in Box 2 is positively correlated to EKE offshore in Box 3 (0.86) and this EKE in Box 3 is correlated to the large-scale circula-

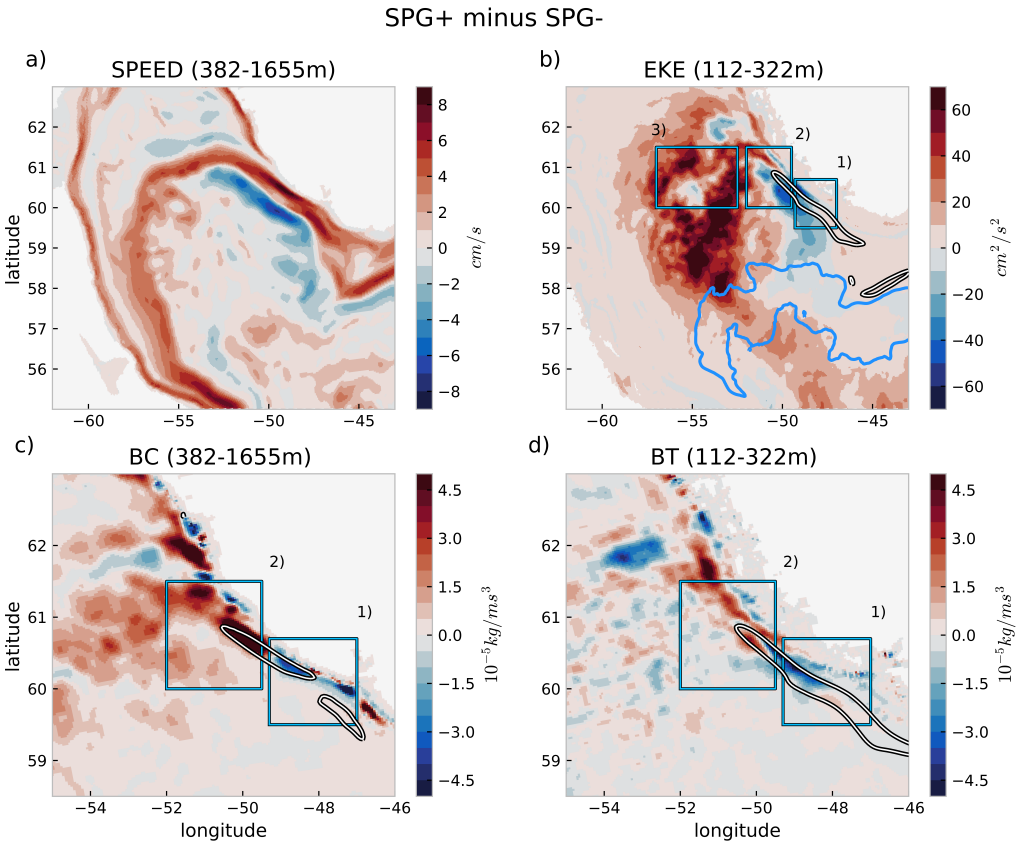

Figure 5.7: Difference between years with mostly positive Subpolar Gyre index (1988 – 1997) and with mostly negative SPG index (1966 – 1975) for (a) Ocean current speed averaged from 382 – 1655 m depth (cm s^{-1}), (b) EKE averaged from 112 – 322 m depth (cm^2s^{-2}), (c) Baroclinic instabilities (energy conversion term T_2) averaged from 382 – 1655 m depth (10^{-5} kg $m^{-1}s^{-3}$), and (d) Barotropic instabilities (energy conversion term T_4) averaged from 112 – 322 m depth (10^{-5} kg $m^{-1}s^{-3}$). Panels (b), (c), and (d) additionally show three boxes used for further investigation: 1) 47.0 – 49.3°W, 59.5 – 60.7°N; 2) 49.5 – 52.0°W, 60.0 – 61.5°N; 3) 52.5 – 57.0°W, 60.0 – 61.5°N; and a white contour representing the area of largest velocity difference, >6 cm s^{-1} in (c) and >9 cm s^{-1} in (b) and (d). The light blue contour in (b) shows the area where the difference in MLD between SPG+ and SPG- is larger than 150 m.

tion, i.e. the SPG index (0.90), as already indicated by Fig. 5.7. Thus, moving further downstream from the instabilities in the WGC has an integrating effect, organizing the intrinsic oceanic variations into longer time-scale variability. This complex pattern explains contradictory results with regard to the instability processes in earlier studies. Depending on the exact region and depth range chosen, the interannual and decadal variability of BC, BT, and EKE is different, and additionally does not always have a local expression.

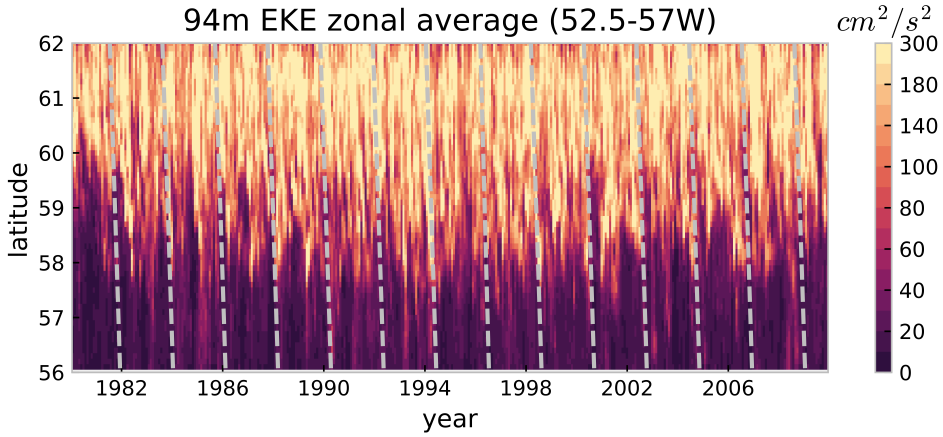

Figure 5.8: Zonally averaged, monthly mean 94 m EKE (from $52.5-57°$W, $\mathrm{cm^2 s^{-2}}$) plotted against time and latitude. Dashed, gray lines help identify propagation of EKE from north to south. The lines are slanted in a way, that an anomaly propagating along them, has a propagation velocity of $\sim$5 cm $\mathrm{s^{-1}}$.

As demonstrated above, the generation IR in the WGC is strongly connected to the large-scale circulation of the SPG. It controls the extent of the convection region to the north through the stratifying effect the IR exert on the northern central LS. Whether the IR variability is responsible for decadal changes of the northward extent of the convection region cannot be determined in a realistic scenario, because the area where deep convection occurs is to first order controlled by the local atmospheric forcing. Only in idealized cases, where EKE in the WGC is altered dramatically, an effect on the extent of the convection region can be observed (Fig. 5.5). Note, that there is a significant negative correlation of -0.39 of EKE off the WGC (i.e. IR) and the northward extent of the convection region (approximated by the area, where MLD $>$ 1000 m north of 57°N, between $50-60$°W) for $1958-1988$ (not shown), however, there is no significant correlation in the last 20 years.

In the following, we address the question whether IR also contribute to the rapid restratification of convected waters in spring, as suggested by previous studies (Eden and Böning 2002; Katsman et al. 2004; Gelderloos et al. 2011).

5.3.1.2 Impact on Restratification

A first hint at the role of IR on the restratification of the convection region in spring can be gleaned from Fig. 5.5. When the number of IR is drastically reduced, the effect on the MLD in the southern central LS is minimal. This suggests that, while the

effect on the northern central LS is large, only few IR propagate to south of 58°N and immediately affect the deep convection there. Additional support for this hypothesis is given by Fig. 5.8. The zonal mean EKE is observed to propagate southward from the generation region. This happens at a speed of $\sim$5 cm s^{-1}, in agreement with previous studies ranging from $3-4$ (Chanut et al. 2008) to 6 cm s^{-1} (Katsman et al. 2004). The southward propagating EKE can be interpreted as IR, however they only intermittently reach south of 58°N, where deep convection regularly occurs. The EKE variations in this region emerge instantaneously in the whole southern central LS, suggesting a local generation. While it is clear that IR that do reach the convection region in spring must in some form influence restratification, the model simulation does not support the idea that they represent a continuous source of restratification, acting in every year. Additionally, EKE off the WGC shows a maximum in winter and the IR need about half a year to reach the convection region (assuming a southward propagation of 5 cm s^{-1}). Thus, the largest impact of IR on the southern central LS is to be expected in late summer, and only for years where IR actually reach the convective area. In fact, in SPG+ years, the MLD in the central LS is deeper compared to SPG- years (Fig. 5.7b). As in the sensitivity study above (Fig. 5.5), the effect of IR is restricted to north of 58°N.

5.3.2 Convective Eddies

A second type of eddy in the LS is the Convective Eddy. CE are generated along the edge of the mixed patch in the central LS (e.g. Marshall and Schott 1999). Figure 5.9 illustrates this process exemplarily for the winter 2007/2008. In November, before the onset of deep convection, relative vorticity at 989 m depth in the central LS is below 0.05 s^{-1}, indicating no substantial mesoscale activity. At the end of March, however, small-scale vorticity structures $>$0.2 s^{-1} in amplitude can be seen at the rim of the convective area, indicating the generation of instabilities, while inside the mixed patch, vorticity is still low. In May, much of this variability is still visible, albeit organized in slightly larger structures. Furthermore, the mesoscale structures have populated the whole central LS in May, including the formerly convective region that did not exhibit mesoscale variability in March. Over the summer, the small-scale variations get eradicated and only few mesoscale features remain in October.

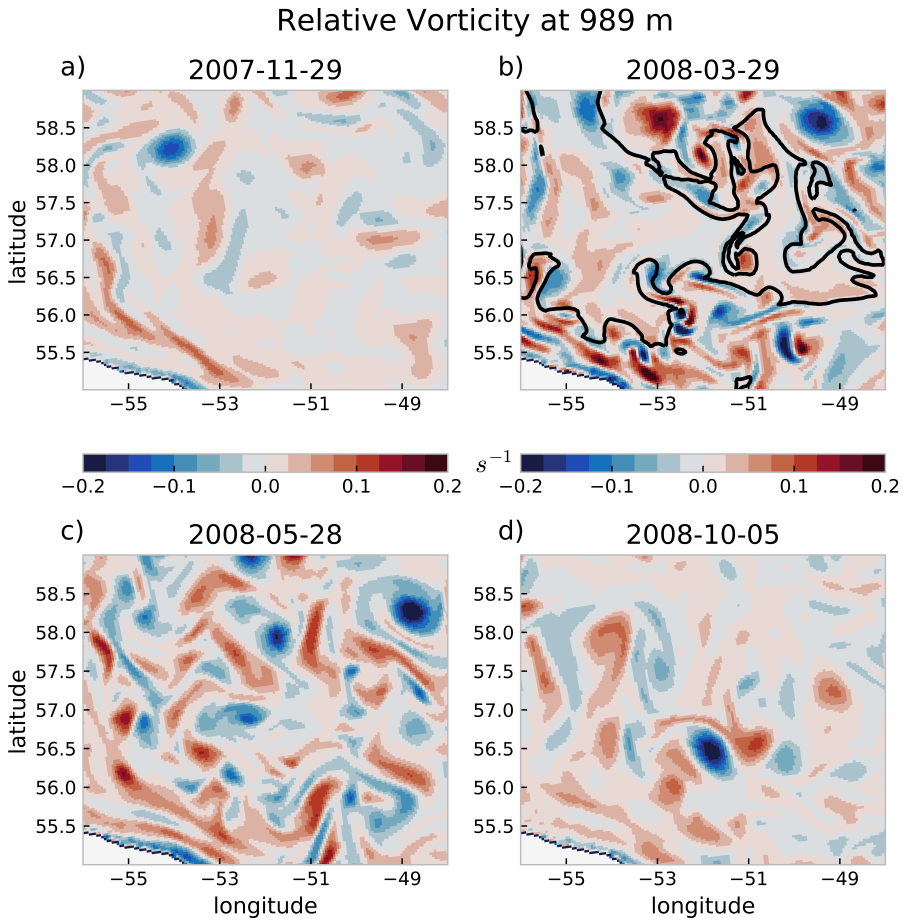

Figure 5.9: 5-day mean of simulated relative vorticity ζ (s^{-1}; shading) at 989 m depth in the central Labrador Sea on (a) 29 November 2007, (b) 29 March 2008, (c) 28 May 2008, and (d) 5 October 2008. The black contour encloses the area, where the mixed layer depth is larger than 989 m.

The distribution of relative vorticity in the vertical yields further insights into the generation of CE (Fig. 5.10). In November, before the onset of convection, relative vorticity away from the boundaries and the bottom is low. At the end of March, convection is at its height as indicated by the Ertel Potential Vorticity (PV $= d\rho/dz(f + \zeta)$) close to zero in large areas. Regarding the CE, the edge of the convective areas at depth is of particular interest. There are five locations in this snapshot (indicated by the black arrows), where large horizontal gradients of PV occur below 1000 m depth which can be identified as boundaries to convective patches. At all five locations, the relative vorticity shows clear maximums >0.1 s^{-1} at the bottom of the mixed layer, that extend to more than 500 m deeper. Additionally, there is a local minimum in PV at 56°N, 800 m depth, seemingly disconnected from the mixed patches to the south and north, which is associated with a relative vorticity minimum and further develops into the anticyclonic eddy in Fig. 5.11.

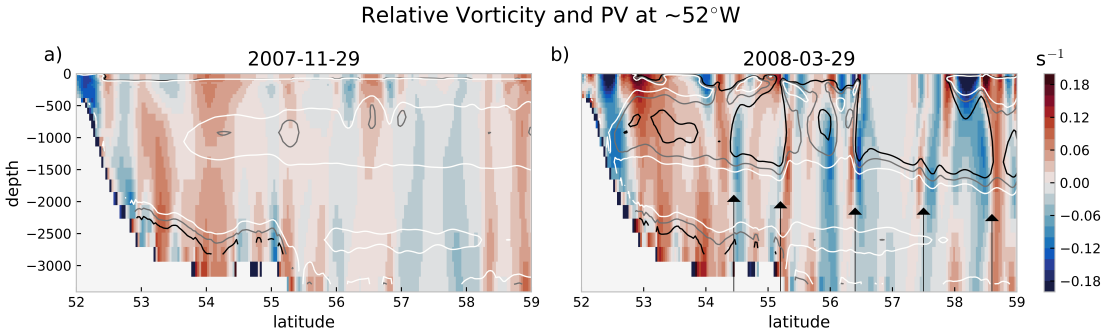

Figure 5.10: Zonal section of relative vorticity ζ (s^{-1}) through the central Labrador Sea at (a) 29 November 2007 and (b) 29 March 2008. Contours in both panels represent potential vorticity of 0.075 (black), 0.050 (gray), and 0.025 kg $m^{-4}s^{-1}$ (white) as an indicator of well-mixed water masses. The black arrows in (b) indicate the locations at the boundaries of the mixed patch where instabilities occur as described in the text.

Thus, some of these small-scale vorticity structures organize into coherent vortices, as observed by Lilly et al. (2003), although the horizontal and vertical resolutions of the model are probably not sufficient to capture the full range of instabilities at the rim of the mixed patch. The simulated CE have a diameter of about 30 km, which is on the upper end of the range given by observations (Lilly et al. 2003). Similarly to the observed lens-shaped vortices, the simulated velocity has a maximum of up to 0.2 m s^{-1} at depth, below 1000 m (Fig. 5.11a). The additional surface-intensified currents depicted in Fig. 5.11a are probably not part of the original CE, but rather stem from another mesoscale structure, merged with the CE. The exact depth of the core depends on the depth of the mixed layer, as can be seen in Fig. 5.10. The core of the CE has low PV and carries temperature and salinity characteristics of the mixed patch. In most cases, and also in the exemplary CE in Fig. 5.11, the core is cold and fresh compared to the surroundings, i.e. the waters outside the mixed patch.

5.3.2.1 Temporal Variability

To further manifest the importance of local instabilities for EKE in the central LS, its temporal variability is investigated in the following. The seasonal cycle of EKE in the central LS ($53.0 - 56.0°$W, $56.0 - 57.5°$N) exhibits April maximums of 20 cm^2s^{-2} for the upper (112 – 322 m) and 14 cm^2s^{-2} for the lower (382 – 1655 m) ocean (5.12). During spring, summer, and early autumn, EKE then decreases gradually toward its minimum of 12 (upper) and 7 cm^2s^{-2} (lower) in October/November, followed by an increase throughout winter. In contrast, the conversion term for barotropic instability does not show a seasonal cycle and remains negative and small at all depth in all

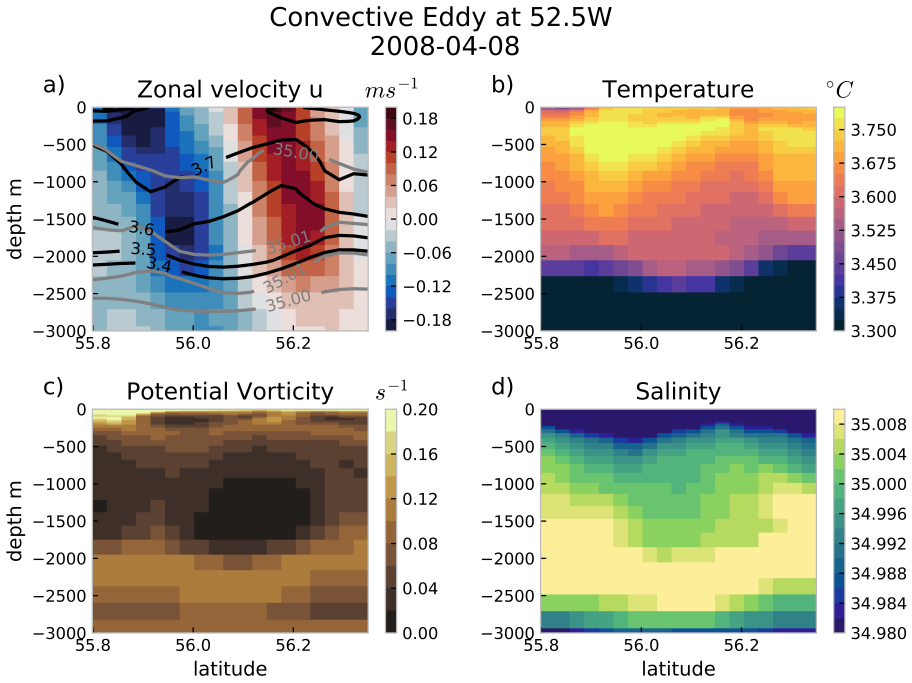

Figure 5.11: Meridional sections through a Convective Eddy at 52.5°W, 56.1°N on 8 April 2008. (a) Zonal velocity (shading) in m s^{-1}, temperature (black contours) in °C, and salinity (gray contours). (b) Temperature in °C. (c) Ertel Potential Vorticity in s^{-1}. (d) Salinity.

months. Also the conversion term for baroclinic instability in the upper ocean does not exhibit a clear seasonal cycle. Only BC in the deeper ocean has a pronounced maximum of 1.0×10^{-6} kg $m^{-1}s^{-3}$ in April, in phase with the EKE, indicating that local baroclinic instability at depth is the major source of EKE at all depths in the central LS, i.e. the convection region.

On longer time scales, a similar picture emerges (Fig. S3). The annual mean EKE in the central LS is significantly correlated to BC in the deeper ocean (correlation coefficient 0.86) and, to the local winter heat fluxes (0.55) responsible for deep convection (averaged over January, February, March). Stronger buoyancy loss in winter leads to stronger convection, which causes larger lateral density gradients responsible for stronger baroclinic instabilities and thus EKE. As with the seasonal variability, BT at all depths is small and mostly negative. Thus baroclinic instabilities at depth are also responsible for changes in central LS EKE at interannual time scales. In some years (e.g. 1985 and 2003), the baroclinic instabilities in the upper ocean are significantly stronger than in the deeper ocean and upper ocean EKE consequently reacts with an

increase. These years are years with weak convection and thus, the processes at work are most likely the same, just shifted toward the surface due to the reduced MLD. Indeed, the depth of the local maximum of BC varies depending on the depth of the mixed layer in each year (not shown).

At decadal time scales (the time-series are smoothed with a box-car window of 5 years length) EKE and BC at depth in the central LS are both significantly correlated to the SPG index (correlation coefficients 0.87 and 0.66 respectively) with $1-2$ years lag, as the SPG is driven by the same large scale atmospheric forcing as the local buoyancy fluxes in the LS. The IR and BCE, as discussed in section 5.3.3, are both forced by the same atmospheric pattern as the deep convection thus some influences of IR and BCE on the decadal variations of EKE in the central LS cannot be ruled out completely. However, the correlation of local BC and EKE points to the conclusion, that the variability of EKE in the central LS is mainly controlled by local forcing at all time scales from seasonal to decadal.

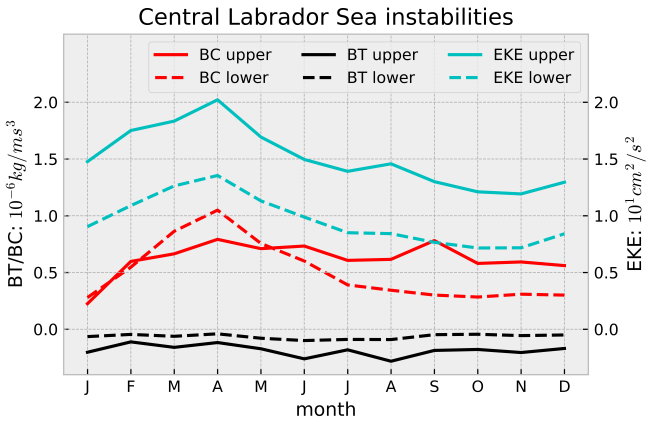

Figure 5.12: Mean simulated climatological seasonal cycle of EKE (cyan lines, 10^1 cm^{2}s^{-2}), BC (red, 10^{-6} kg m^{-1}s^{-3}), and BT (black, 10^{-6} kg m^{-1}s^{-3}) in the central Labrador Sea ($53.0-56.0°$W, $56.0-57.5°$N). Solid lines depict the upper ocean ($112-322$ m), dashed lines the deeper ocean ($382-1655$ m).

5.3.2.2 Impact on Restratification

Convective Eddies are the most promising mechanism for rapid restratification of the mixed patch in spring. CE are formed during the convection process directly along the convection area and thus inevitably lead to an exchange of the waters outside and inside the mixed patch. This is supported by a comparison of the seasonal evolution of the potential density (with reference to 1000 m) anomaly averaged over $500-3000$ m in the central LS between the simulation with $1/20°$ resolution and a short simulation with $1/12°$ (Fig. 5.13). At $1/12°$ (roughly 6 km in the central LS), CE are not well resolved and while instabilities still occur along the mixed patch (not shown), they are less energetic and the effect on restratification should be reduced. At the same time, IR are still

well resolved at 1/12° and a comparison of these two simulations can be used to approximate the effect of CE on restratification. Figure 5.13 shows that restratification is indeed much slower in spring right after the convection period, when the horizontal resolution is reduced. With 1/20°, the positive winter anomaly is halved just 1.5 months after the end of deep convection, compared to 4 months at 1/12°. Later in the year (from June/July on), the density decreases at a similar rate, independent of resolution. Toward the end of the year, the decrease in the 1/12° simulation is larger compared to 1/20°. This could be influenced by an overestimated convection in the 1/12° simulation, possibly due to the reduced mesoscale activity in the central LS.

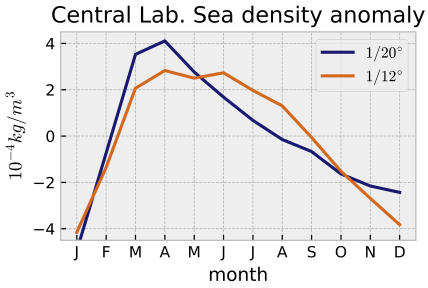

Figure 5.13: Climatological mean seasonal anomalies of density σ_1 (kg m^{-3}) in the central Labrador Sea (53.0−56.0°W, 56.0−57.5°N) averaged from 500 − 3000 m depth for the 1/20° simulation (blue line) and the 1/12° simulation (orange line).

5.3.3 Boundary Current Eddies

Boundary Current Eddies are generated along the boundary currents of the LS. While BCE exist along the WGC south of the region where IR are generated (not shown), this section is focused on the BCE of the LC, as they are more likely to influence convection due to their proximity to the area of deepest winter mixed layers (5.4). As shown by figure 5.14 for a typical BCE at the western boundary, these eddies are strongly surface intensified and do not reach as deep as the IR from the WGC. The velocity maximum of 0.2 m s^{-1} is found at the surface. The core of the BCE is highly stratified, with a combination of fresh and cold water on top of warm and saline water, similar to the IR shed from the eastern boundary. However, the more saline water below ∼200 m depth is still fresh compared to the surroundings.

To illustrate the seasonal cycle of BCE, the climatological seasonal evolution of EKE is shown with a focus on the LC in Fig. 5.15. Eddy Kinetic Energy has a maximum of $50 - 100$ cm^{2}s^{-2} in the LC in winter, and decreases throughout spring and summer to a minimum of $10 - 20$ cm^{2}s^{-2} and starts to increase again in autumn. This seasonal evolution is observed at all latitudes from $55 - 64$°N in the LC. Offshore of the LC, there is a distinct minimum of EKE in all seasons. Further toward the interior, EKE

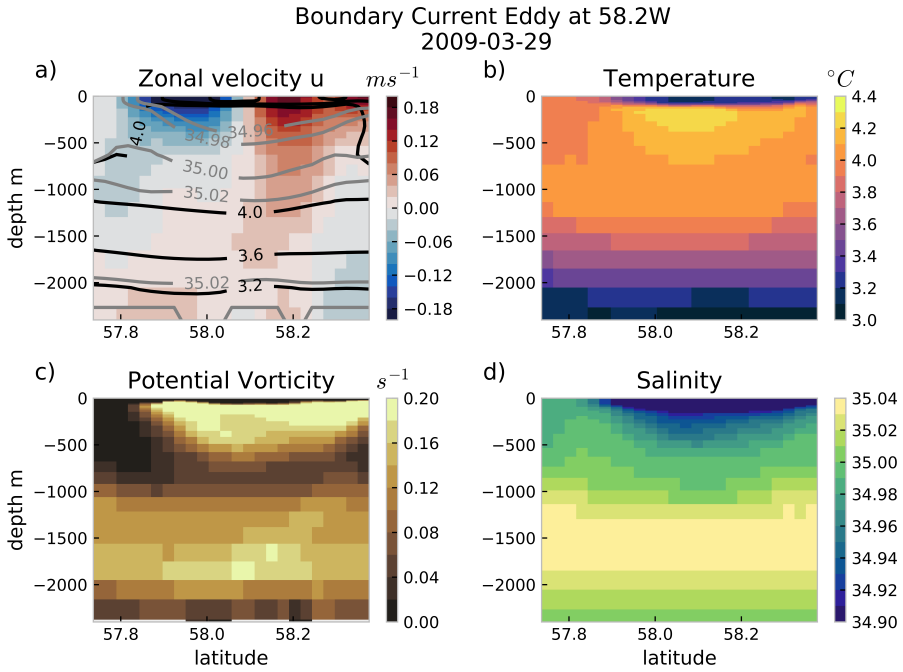

Figure 5.14: Meridional sections through a Boundary Current Eddy at 58.2°W, 58.1°N on 29 March 2009. (a) Zonal velocity (shading) in m s^{-1}, temperature (black contours) in °C, and salinity (gray contours). (b) Temperature in °C. (c) Ertel Potential Vorticity in s^{-1}. (d) Salinity.

increases again due to the IR in the north and locally generated EKE further south. Especially close to the convection region south of 58°N, the seasonal variations of EKE are confined to a narrow band along the shelf and are not observed to reach into the area of deep convection. Thus, BCE are most likely not contributing substantially to the restratification of the mixed patch in spring. Support for this hypothesis is found in Fig. 5.5. The reduction of IR in the sensitivity study yields an increased strength of the LC (not shown). This in turn causes more baroclinic instabilities and thus generation of EKE (light red area in Fig. 5.5a). However, an influence on the MLD of this increased EKE is only found in the far western part of the convection region. At this point it is unclear, whether this is due to the work of the BCE against preconditioning of this area or due to to an active restratification of the mixed layer during and after convection.

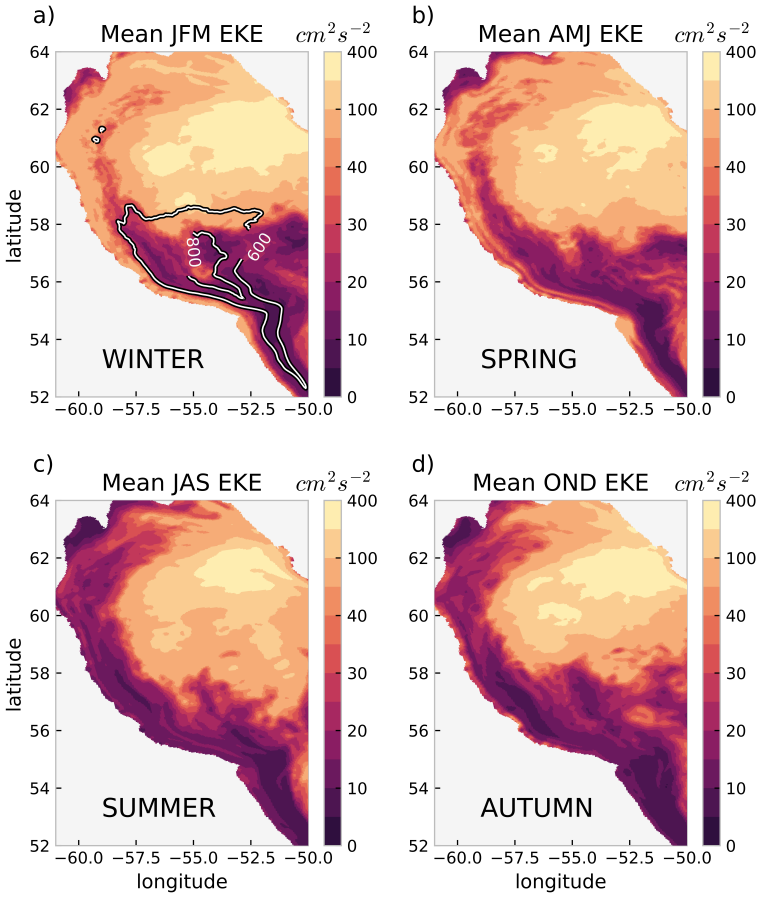

Figure 5.15: Mean 94 m EKE ($2000-2009$) in $\mathrm{cm^2 s^{-2}}$ in the Labrador Sea for (a) winter (January, February, March), (b) spring (April, May, June), (c) summer (July, August, September), and (d) autumn (October, November, December). Note the non-linear color scale used for the shading. Panel (a) features contours of MLD at 600 and 800 m to illustrate the region of deep convection in winter.

5.4 Summary and Conclusion

This study investigates different sources of Eddy Kinetic Energy in the Labrador Sea with the help of a 52-year long hindcast simulation of a $1/20°$ nested OGCM. Besides a good representation of the mean near-surface EKE and MLD in the LS (Fig. 5.4), the model also is able to simulate all three major types of eddies in the LS, Irminger Rings, Convective Eddies, and Boundary Current Eddies, with characteristics close to observational accounts (Fig. 5.3, 5.11, and 5.14).

Irminger Rings are generated between 60 and 62°N in the WGC along the west coast of Greenland by baroclinic instabilities at depth (below ∼400 m) with a smaller contribution of barotropic instabilities between $112 - 322$ m (Fig. 5.6). The observed seasonal cycle of EKE is well reproduced by the model and the associated instability processes are resolved. In concert with the strength of the WGC, the seasonal cycle peaks in winter. The instability processes reach their maximum in January, while EKE, as a resulting quantity, is highest in February.

On longer time scales, the generation of IR and the EKE in the northern central LS are connected to the large-scale circulation of the subpolar gyre, which appears to a large degree to be driven by atmospheric variability. A prevailing positive phase of the Arctic Oscillation facilitates a stronger subpolar gyre, and increases velocities in the boundary currents. In the WGC, this leads to a downstream (north-westward) shift of the occurrence of instabilities and also the generated EKE (Fig. 5.7). A sensitivity study with a switch from "no-slip" to "free-slip" as a lateral boundary condition along the west coast of Greenland results in a strong suppression of IR generation and demonstrates that their main effect is limited to the northern part of the LS (north of 58°N): under the same atmospheric forcing, a reduction in IR abundance thus alters the preconditioning and results in an extension of the area of deep convection to the north. In a realistic scenario where variations of the numbers of IR shed from the WGC are related to temporal changes in the atmospheric forcing, the consequences are more complex. A stronger forcing (positive AO) leads, simultaneously, to stronger convection due to the local heat loss in the central LS, and to weaker preconditioning due to more IR. As the convection is to first order related to local heat loss, the effect of the IR is only minor in a realistic setting.

Due to the limitation of the IR's effect to the northern central LS, no substantial impact on rapid restratification of the mixed patch in spring is expected. While occasionally there are IR arriving in the central LS in spring that are possibly contributing to the restratification of the freshly convected water masses, this does not occur annually, so that IR are just an additional, intermittent factor in the restratification of the deep winter mixed layer in some years.

The main source of EKE in the central LS and thus of rapid restratification in spring are the Convective Eddies. Convective Eddies emerge along the rim of the mixed patch, due to the baroclinic instabilities triggered by the large lateral buoyancy gradient

across the edge of the convection area (Fig. 5.9 and 5.12). In agreement with the time of deepest mixed layers at the end of winter/beginning of spring, the seasonal cycle of EKE in the central LS peaks in April. As derived from theoretical considerations (Jones and Marshall 1997; Dewar 2002), the strongest baroclinic instabilities occur near the bottom of the mixed layer. Another sensitivity study with a 1/12° configuration of the same model supports the CE's role in rapid restratification of the mixed patch. A resolution of 1/12° is not resolving CE and consequently, the restratification is significantly slower (Fig. 5.13).

The interannual to decadal variability of CE is controlled by the atmospheric forcing. Large buoyancy loss at the surface triggers deep convection and thus the baroclinic instabilities at depth. The local air-sea fluxes and the resulting convection and EKE generation are correlated to the large-scale atmospheric state as expressed, e.g. by the AO index.

The third class of eddies in the LS are the Boundary Current Eddies. They are not found to propagate far from the boundary currents, where they are generated by baroclinic instabilities. In the vicinity of the Labrador Current the BCE's impact is restricted to the far western part of the convection region. Furthermore, it could be overestimated by the model because deep convection appears to be simulated unrealistically close to the boundary current. In an earlier configuration of the model used here, Handmann et al. (2018) find the western boundary current in the LS to be too barotropic, compared to observations. We speculate, that a too barotropic boundary current is likely to produce insufficiently strong baroclinic instabilities and hence fewer BCE. A weak eddy field along the western boundary then partially fails to act against the preconditioning, facilitating strong convection close to the shelf. The complex interplay between the LC, BCE and deep convection needs further, detailed investigation.

In conclusion, the Irminger Rings in the northern central Labrador Sea and to a lesser extent the Boundary Current Eddies along the Labrador Current appear as vital components acting against the preconditioning for deep convection. In the mean, they limit the area of deep convection to the southern part of the central LS. During periods of favorable atmospheric conditions, a possible increase of deep convection in the northern central LS due to local air-sea buoyancy loss is counteracted by a strengthened limiting, stratifying effect of IR and BCE. The Convective Eddies in the

central LS, tightly linked to the strength of deep convection, are the main driver of the rapid restratification in spring.

As suggested by this study, a critical aspect of ocean model formulations to successfully simulate the Labrador Sea's mesoscale eddy field and its impact on deep convection is the combination of high resolution and a realistic location of the area of deep convection. The implementation of an adequate lateral boundary condition ("no-slip" in this study) in the WGC region is additionally necessary for a correct representation of the Irminger Rings. Idealized model configurations set up to study mesoscale variability in the LS generally fulfill the requirement for a high resolution and an adequate lateral boundary condition. However, deep convection is often represented by a circular mixed patch located rather centrally in the LS (e.g. Katsman et al. 2004). With the area of deep convection located too close to the westward path of the IR, their effect on restratification is likely to be overestimated. In OGCMs with realistic geometry and forcing, the horizontal resolution often is the limiting factor. Generally, a low resolution also implies a misrepresentation of the mixed patch's location and lateral extent. Without explicitly resolving the IR and BCE, the preconditioned area in the central LS is too large. Furthermore, CE are not resolved and thus do not counteract deep convection or restratify the mixed patch in spring. The combined effect is an overestimation of the extent and depth of deep convection (e.g. Rattan et al. 2010) in most OGCMs with coarse resolutions. Simulations at $1/20^\circ$ still exhibit biases in the hydrographic properties of the Labrador Sea (Handmann et al. 2018), however, the presented study shows $1/20^\circ$ to be sufficient to simulate most of the mesoscale dynamical features.

5.5 Supplemental Material to "The Nature of Eddy Kinetic Energy in the Labrador Sea: Different Types of Mesoscale Eddies, their Temporal Variability and Impact on Deep Convection"

This supplemental material includes 3 additional figures referenced in the main manuscript.

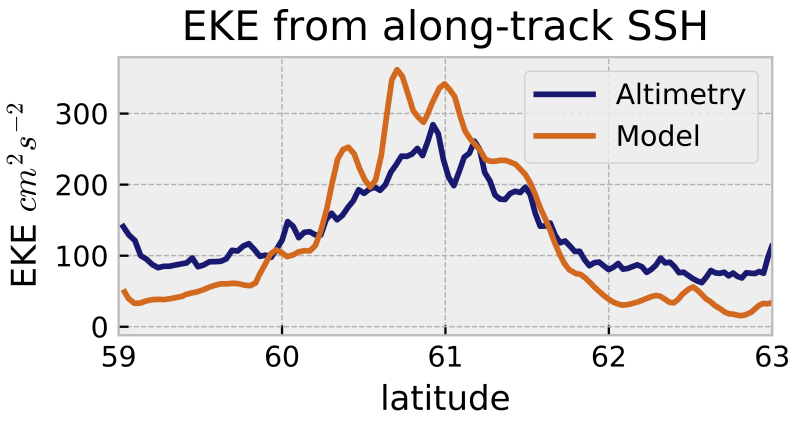

Figure 5.16: EKE derived from along-track satellite SLA data (blue) and EKE from sub-sampled SSH data from the model (orange) along the track displayed in Fig. 4 of the main manuscript. The observational estimate for EKE is derived from the gridded, delayed time geostrophic surface velocities (SEALEVEL_GLO_PHY_L4_REP_OBSERVATIONS_008_047) made available by E.U. Copernicus Marine Service (CMEMS) and calculated as described above. Additionally, 1 Hz along-track sea level anomaly (SLA) data developed, validated, and distributed by the CTOH/LEGOS, France (X-TRACK; Birol et al. 2017) are used in the Labrador Sea (Topex/Poseidon, Jason-1/2/3, Track 72), to account for the underestimation of EKE derived from gridded SLA products at high latitudes (Zhang and Yan 2018). Here, EKE is calculated from $EKE = V_x^2$ (isotropy is assumed), where $V_x = (g/f)(d\eta/dx_{dist})$ is the across-track geostrophic velocity. Here, g refers to the gravitational acceleration, f is the Coriolis parameter, η is the along-track SLA and x_{dist} is the distance between two ground points along the satellite track. The SLA η is low-pass filtered with a ∼40 km cutoff LOESS filter. To compare the modeled EKE to this observational value, daily mean simulated SLA are sub-sampled with a nearest-neighbor lookup to the times and locations of the satellite-derived SLA and then treated identically.

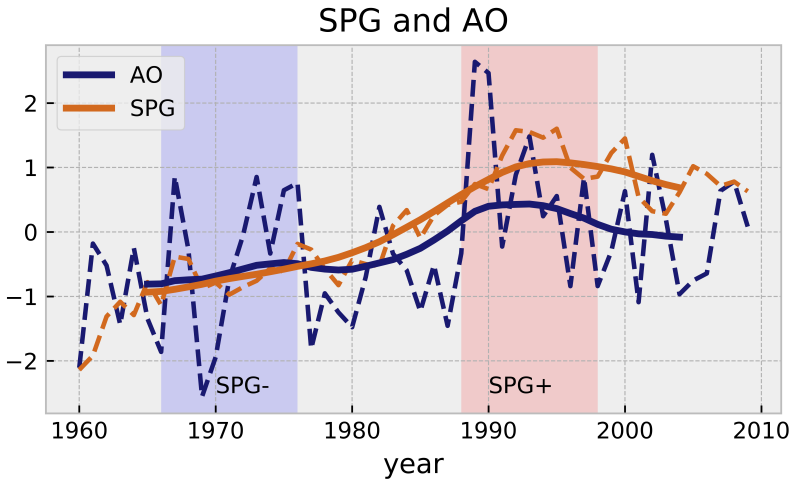

Figure 5.17: Subpolar Gyre index (blue) as described in section 5.2 of the main manuscript and Arctic Oscillation index (orange; Higgins et al. 2002). Solid lines depict annual mean values, dashed lines represent the smoothed time series (a 10-year boxcar filter is used). The shaded areas indicate the periods chosen for a weak SPG (SPG-) and a strong SPG (SPG+) in blue and red, respectively. This figure illustrates the integrating role of the ocean; the low-frequency variability of the simulated SPG and the observed AO are similar, with a slight increase throughout the 1960s and 1970s, a faster increase into the mid-1990s and a decrease thereafter until the end of the time series. Contrarily, the higher frequency variations in the AO are not reflected by the SPG.

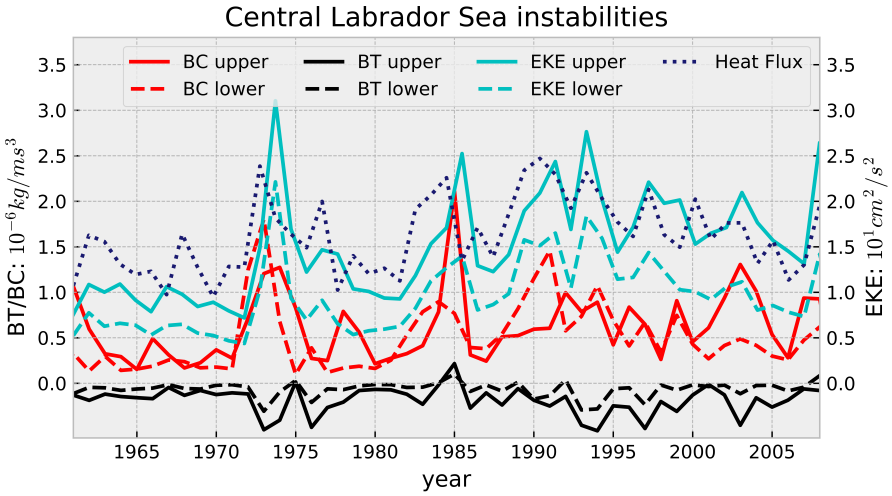

Figure 5.18: Simulated annual mean EKE (cyan lines, 10^2 cm^{2}s^{-2}), BC (red, 10^{-6} kg m^{-1}s^{-3}), and BT (black, 10^{-6} kg m^{-1}s^{-3}) in the central Labrador Sea ($53.0 - 56.0°$W, $56.0 - 57.5°$N). Solid lines depict the upper ocean ($112 - 322$ m), dashed lines the deeper ocean ($382 - 1655$ m). The dotted blue line shows the annual mean heat loss (2×10^2 W m^{-2}) of the ocean to the atmosphere in the central Labrador Sea. The annual mean EKE in the central LS is significantly correlated to BC in the deeper ocean (correlation coefficient 0.86) and, to the local winter heat fluxes (0.55) responsible for deep convection (averaged over January, February, March).

6 Summary and Conclusion

This thesis studies the nature of Eddy Kinetic Energy, its generation and temporal variability in two selected regions of the world ocean. The first region encompasses the Subtropical Countercurrent in the South Pacific, and the second region is focused on the Labrador Sea in the western subpolar North Atlantic. An Ocean General Circulation Model based on the NEMO code builds the foundation for these investigations.

A configuration with 1/4° horizontal resolution is used in section 3 to illustrate the ability of the eddy-permitting configuration to sufficiently simulate the oceanic mesoscale at subtropical latitudes. In order to achieve the best possible representation of the generation mechanisms of EKE, the viscosity parameter for the horizontal diffusion of momentum is reduced. It is shown, that the viscosity can be halved with respect to the "standard" value without increasing the grid-scale noise above an acceptable level. Although not all numerical constraints such as the viscous Courant-Friedrichs-Levy criterion, the threshold for the Grid-Reynolds number, and the Munk boundary layer criterion are strictly adhered to, the model integration does not blow up, probably due to the additional, unknown amount of numerical diffusion. While noise levels are only slightly increased compared to the reference simulation, the EKE in the STCC region is increased by ∼50%, approaching values that can otherwise only be achieved with higher-resolution configurations. At the same time, the large-scale hydrographic properties of the subtropical South Pacific are not significantly affected by the reduced viscosity. At a global scale, important circulation features such as the Atlantic Meridional Overturning Circulation and the Antarctic Circumpolar Current exhibit lowered transports, so that the conclusions obtained from the investigations in the South Pacific may not be applicable to all ocean basins. Nevertheless, advantage is taken of the improvements regarding the mesoscale in the subtropical South Pacific and the 1/4° configuration is used for the investigations in section 4, exploiting the fact that the eddy-permitting configuration allows to perform a variety of sensitivity studies at a relatively low computational cost.

The 1/4° configuration reproduces the observed salient features of EKE and baroclinic instability in the STCC at seasonal time scales, as well as the long-term variations of EKE simulated with a high-resolution model. In order to attribute an atmospheric cause to the decadal variations, as a first step, the ratio of intrinsic to total mesoscale variability on long time scales is investigated. In the STCC region (25°-33°S, 153°-

175°W), this ratio is indeed relatively small compared to the surroundings and the other subtropical gyres, indicating that the long-term variability of EKE is driven by variations in the atmosphere. The EKE exhibits substantial changes on decadal time scales, especially pronounced in the 1970s, when EKE is about twice as large as the mean. This peak is followed by a rapid decrease in the 1980s, and low EKE all through the 1990s. Towards the end of the simulated period, EKE then starts to increase again in the 2000s. Various sensitivity studies with varying wind and buoyancy forcing from the atmosphere reveal that these changes are wind-driven and strongly connected to the Interdecadal Pacific Oscillation. More specifically, the changes in wind stress curl associated with the large-scale atmospheric circulation during positive IPO phases (e.g. 1970s) lead to upwelling just south of the STCC and downwelling in the STCC region, effectively strengthening the meridional density gradient at the depth of the thermocline and thereby increasing the strength of the STCC, local baroclinic instability and the resulting EKE. Analogously, the meridional density gradient, the STCC and EKE are reduced during negative phases of the IPO (e.g. 1980s and 1990s) due to upwelling in the STCC and downwelling just south of it. An additional 30 to 40% of the local density gradient anomalies can be explained by long baroclinic Rossby waves propagating into the region from the east. These waves modulate the decadal signal of the IPO's influence in the STCC on interannual time scales. Considering the profound impact of the large-scale atmospheric circulation on the STCC, it is prone to also significantly react to future changes. Due to its proximity to regions of subduction and Mode Water formation (e.g. Li 2012), potential changes in the STCC and its EKE could also impact the Subtropical Cells and thereby the equatorial circulation (e.g. Yamanaka et al. 2015). The eddy-permitting configuration appears to be a reasonable basis for future investigations of these mechanisms, as it is well capable of simulating the mesoscale, its generation and temporal variability in the subtropical South Pacific, given an adequate choice of the viscosity parameter for the horizontal diffusion of momentum.

The second region of interest, the Labrador Sea in the western subpolar North Atlantic, requires a substantially higher horizontal resolution of the ocean model configuration to resolve the mesoscale due to its location at high latitudes. In order to limit the computational cost, the resolution is only regionally increased to $1/20°$ in the North Atlantic. Additionally, several other aspects of the model formulation are essential to the investigations of section 5. A realistic topography and atmospheric forcing, and a "no-slip" lateral boundary condition in the WGC are necessary to simulate the

generation of the different types of eddies and the locations of their occurrence. Furthermore, the long integration period of 52 years is needed to overcome the difficulties of attributing an atmospheric driver to the simulated changes in the ocean that arise due to the ocean's intrinsic variability. The VIKING20X simulation fulfills these requirements and shows three different types of eddies to be important in the LS. The anticyclonic, warm-core, stratified Irminger Rings are generated by a combination of baroclinic and barotropic instabilities in the WGC near Cape Desolation and propagate toward the West and Southwest, effectively counteracting the destratification of the water column by winter heat loss to the atmosphere, thus prohibiting deep convection in the northern central LS. Based on sensitivity studies and the intermittent occurrences of IR propagating to south of 58°N, it is found that IR only have a minor impact on restratification of the mixed patch. While their interannual variability is largely intrinsic, elevated (lowered) EKE in the IR path can be explained by increased (decreased) generation of EKE due to a stronger (weaker) WGC associated with a positive (negative) Subpolar Gyre Index on decadal time scales. The changes in strength of the Subpolar Gyre are ultimately driven by the large-scale atmospheric circulation. Similarly, the abundance of Boundary Current Eddies is associated with the strength of the Subpolar Gyre and thus the WGC and LC. The BCE are surface-intensified, baroclinically generated, small vortices all along the boundary currents of the LS that are found to have limited, yet not fully understood, impact on preconditioning and restratification of the central LS. Especially the rapid restratification of convected waters in spring is mainly a consequence of the stirring of the mixed patch with the surroundings by Convective Eddies. The CE have a mid-depth core containing waters from within the convective area, usually cold and fresh compared to their surroundings. Convective Eddies emerge from baroclinic instability of the rim-current along the edge of the mixed patch and their temporal variability is atmospherically driven. As a direct consequence of increased wind stress and heat loss from the ocean, deep convection, the associated rim-current and thus the generation of CE are strengthened. It should be noted that the 1/20° simulation is only capable of sufficiently resolving the larger CE (observed diameters are 10-36 km (Lilly et al. 2003)) and thus their impacts on the hydrography of the central LS are possibly underestimated. Additionally, the realism of the extent and location of the simulated area of deep convection is hard to assess, but is an important factor for the distribution of CE. In summary, the IR and CE are of profound importance to deep convection in the central LS. While IR play a vital role in stratifying large parts of the basin and thus suppressing deep convection, CE are the major driver of rapid restratification during and after deep convection.

In conclusion, the nature of Eddy Kinetic Energy, its generation, impacts and temporal variability can be successfully simulated by Ocean General Circulation Models with the right choice of parameters and resolution for the respective regions under investigation. While observations, though increasingly abundant, are still sparse compared to the vastness of the oceans and time series seldom reach lengths of several decades, OGCMs offer the required temporal and spatial resolution and extent to investigate the long-term variations of the mesoscale beyond the intrinsic time scales. Thus, ocean models are an important, inevitable tool to study the oceanic Eddy Kinetic Energy.

Bibliography

Arakawa, A., and Y.-G. Hsu, 1990: Energy conserving and potential-enstrophy dissipating schemes for the shallow water equations. *Monthly Weather Review*, **118**, 1960–1969.

Arbic, B. K., 2000: Generation of Mid-Ocean Eddies: The Local Baroclinic Instability Hypothesis. Ph.D. thesis, Massachusetts Institute of Technology and Woods Hole Oceanographic Institution.

Barnier, B., and Coauthors, 2006: Impact of partial steps and momentum advection schemes in a global ocean circulation model at eddy-permitting resolution. *Ocean Dynamics*, **56**, 543–567, doi:10.1007/s10236-006-0082-1.

Barrier, N., J. Deshayes, A.-M. Tréguier, and C. Cassou, 2015: Heat budget in the North Atlantic subpolar gyre: Impacts of atmospheric weather regimes on the 1995 warming event. *Progress in Oceanography*, **130**, 75–90, doi:10.1016/j.pocean.2014.10.001.

Beckmann, A., C. W. Böning, C. Köberle, and J. Willebrand, 1994: Effects of Increased Horizontal Resolution in a Simulation of the North Atlantic Ocean. *Journal of Physical Oceanography*, **24**, 326–344.

Behrens, E., K. Våge, B. Harden, A. Biastoch, and C. W. Böning, 2017: Composition and variability of the Denmark Strait Overflow Water in a high-resolution numerical model hindcast simulation. *Journal of Geophysical Research: Oceans*, **122**, 2830–2846, doi:10.1002/2016JC012158.

Berloff, P., I. Kamenkovich, and J. Pedlosky, 2009: A mechanism of formation of multiple zonal jets in the oceans. *Journal of Fluid Mechanics*, **628**, 395–425, doi:10.1017/S0022112009006375.

Berx, B., and M. R. Payne, 2017: The Sub-Polar Gyre Index - A community data set for application in fisheries and environment research. *Earth System Science Data*, **9**, 259–266, doi:10.5194/essd-9-259-2017.

Birol, F., and Coauthors, 2017: Coastal applications from nadir altimetry: Example of the X-TRACK regional products. *Advances in Space Research*, **59**, 936–953, doi:10.1016/j.asr.2016.11.005.

Blanke, B., and P. Delecluse, 1993: Variability of the Tropical Atlantic Ocean Simulated by a General Circulation Model with Two Different Mixed-Layer Physics. *Journal of Physical Oceanography*, **23**, 1363–1388.

Böning, C. W., E. Behrens, A. Biastoch, K. Getzlaff, and J. L. Bamber, 2016: Emerging impact of Greenland meltwater on deepwater formation in the North Atlantic Ocean. *Nature Geoscience*, **9**, 523–527, doi:10.1038/ngeo2740.

Böning, C. W., and R. G. Budich, 1992: Eddy Dynamics in a Primitive Equation Model: Sensitivity to Horizontal Resolution and Friction. *Journal of Physical Oceanography*, **22**, 361–381.

Böning, C. W., R. Döscher, and R. G. Budich, 1991: Seasonal Transport Variation

in the Western Subtropical North Atlantic: Experiments with an Eddy-resolving Model. *Journal of Physical Oceanography*, **21**, 1271–1289.

Bracco, A., J. Pedlosky, and R. S. Pickart, 2008: Eddy Formation near the West Coast of Greenland. *Journal of Physical Oceanography*, **38**, 1992–2002, doi:10.1175/2008JPO3669.1.

Brandt, P., F. A. Schott, A. Funk, and C. S. Martins, 2004: Seasonal to interannual variability of the eddy field in the Labrador Sea from satellite altimetry. *Journal of Geophysical Research*, **109**, C02 028, doi:10.1029/2002JC001551.

Breckenfelder, T., M. Rhein, A. Roessler, C. W. Böning, A. Biastoch, E. Behrens, and C. Mertens, 2017: Flow paths and variability of the North Atlantic Current: A comparison of observations and a high-resolution model. *Journal of Geophysical Research: Oceans*, **122**, 2686–2708, doi:10.1002/2016JC012444.

Bryan, K., S. Manabe, and R. C. Pacanowski, 1975: A Global Ocean-Atmosphere Climate Model. Part II. The Oceanic Circulation. *Journal of Physical Oceanography*, **5**, 30–46.

Callies, J., and R. Ferrari, 2013: Interpreting Energy and Tracer Spectra of Upper-Ocean Turbulence in the Submesoscale Range (1–200 km). *Journal of Physical Oceanography*, **43**, 2456–2474, doi:10.1175/JPO-D-13-063.1.

Chanut, J., B. Barnier, W. Large, L. Debreu, T. Penduff, J. M. Molines, and P. Mathiot, 2008: Mesoscale Eddies in the Labrador Sea and Their Contribution to Convection and Restratification. *Journal of Physical Oceanography*, **38**, 1617–1643, doi:10.1175/2008JPO3485.1.

Chelton, D. B., 1998: Geographical Variability of the First Baroclinic Rossby Radius of Deformation. *Journal of Physical Oceanography*, **28**, 433–460.

Chelton, D. B., and M. G. Schlax, 1996: Global Observaions of Oceanic Rossby Waves. *Science*, **272**, 234–238, doi:10.1126/science.272.5259.234.

Chin, T., R. Milliff, and W. Large, 1998: Basin-scale high-wavenumber sea surface wind fields from multiresolution analysis of scatterometer data. *Journal of Atmospheric and Oceanic Technology*, **15**, 741–763.

Combes, V., and E. Di Lorenzo, 2007: Intrinsic and forced interannual variability of the Gulf of Alaska mesoscale circulation. *Progress in Oceanography*, **75**, 266–286, doi:10.1016/j.pocean.2007.08.011.

Cox, M. D., 1985: An Eddy Resolving Numerical Model of the Ventilated Thermocline. *Journal of Physical Oceanography*, **15**, 1312–1324.

Czeschel, R., L. Stramma, F. U. Schwarzkopf, B. S. Giese, A. Funk, and J. Karstensen, 2011: Middepth circulation of the eastern tropical South Pacific and its link to the oxygen minimum zone. *Journal of Geophysical Research: Oceans*, **116**, 1–13, doi:10.1029/2010JC006565.

de Jong, M. F., A. S. Bower, and H. H. Furey, 2014: Two Years of Observations of Warm-Core Anticyclones in the Labrador Sea and Their Seasonal Cycle in Heat and Salt Stratification. *Journal of Physical Oceanography*, **44**, 427–444, doi:10.1175/

JPO-D-13-070.1.

de Jong, M. F., A. S. Bower, and H. H. Furey, 2016: Seasonal and Interannual Variations of Irminger Ring Formation and Boundary–Interior Heat Exchange in FLAME. *Journal of Physical Oceanography*, **46**, 1717–1734, doi:10.1175/JPO-D-15-0124.1.

Debreu, L., C. Vouland, and E. Blazo, 2008: AGRIF: Adaptive grid refinement in Fortran. *Computers and Geosciences*, **34**, 8–13, doi:10.1016/j.cageo.2007.01.009.

Delworth, T. L., and Coauthors, 2012: Simulated climate and climate change in the GFDL CM2.5 high-resolution coupled climate model. *Journal of Climate*, **25**, 2755–2781, doi:10.1175/JCLI-D-11-00316.1.

Dengler, M., F. A. Schott, C. Eden, P. Brandt, J. Fischer, and R. Zantopp, 2004: Break-up of the Atlantic deep western boundary current into eddies at 8°S. *Nature*, **432**, 1018–1020.

Deshayes, J., and Coauthors, 2013: Oceanic hindcast simulations at high resolution suggest that the Atlantic MOC is bistable. *Geophysical Research Letters*, **40**, doi:10.1002/grl.50534.

Dewar, W. K., 2002: Convection in Small Basins. *Journal of Physical Oceanography*, **32**, 2766–2788.

DRAKKAR Group, 2007: Eddy-permitting ocean circulation hindcasts of the past decades. *CLIVAR Exchanges*, **12 (42)**, 8–10.

DRAKKAR Group, 2014: DRAKKAR: developing high resolution ocean components for European Earth system models. *CLIVAR Exchanges*, **19 (65)**, 18–21.

Ducousso, N., J. Le Sommer, J.-M. Molines, and M. Bell, 2017: Impact of the "Symmetric Instability of the Computational Kind" at mesoscale- and submesoscale-permitting resolutions. *Ocean Modelling*, **120**, 18–26, doi:10.1016/j.ocemod.2017.10.006.

Eden, C., and C. Böning, 2002: Sources of Eddy Kinetic Energy in the Labrador Sea. *Journal of Physical Oceanography*, **32**, 3346–3363.

Farneti, R., S. Dwivedi, F. Kucharski, F. Molteni, and S. M. Griffies, 2014: On Pacific Subtropical Cell Variability over the Second Half of the Twentieth Century. *Journal of Climate*, **27**, 7102–7112, doi:10.1175/JCLI-D-13-00707.1.

Feng, M., C. W. Böning, A. Biastoch, E. Behrens, E. Weller, and Y. Masumoto, 2011: The reversal of the multi-decadal trends of the equatorial Pacific easterly winds, and the Indonesian Throughflow and Leeuwin Current transports. *Geophysical Research Letters*, **38**, L11 604, doi:10.1029/2011GL047291.

Fichefet, T., and M. a. M. Maqueda, 1997: Sensitivity of a global sea ice model to the treatment of ice thermodynamics and dynamics. *Journal of Geophysical Research*, **102 (C6)**, 12 609–12 646, doi:10.1029/97JC00480.

Fischer, J., J. Karstensen, M. Oltmanns, and S. Schmidtko, 2018: Mean circulation and EKE distribution in the Labrador Sea Water level of the subpolar North Atlantic. *Ocean Science*, **14**, 1167–1183, doi:10.5194/os-14-1167-2018.

Fischer, J., and Coauthors, 2015: Intra-seasonal variability of the DWBC in the western subpolar North Atlantic. *Progress in Oceanography*, **132**, 233–249, doi:10.1016/j.pocean.2014.04.002.

Frankignoul, C., N. Sennéchael, Y.-O. Kwon, and M. A. Alexander, 2011: Influence of the Meridional Shifts of the Kuroshio and the Oyashio Extensions on the Atmospheric Circulation. *Journal of Climate*, **24**, 762–777, doi:10.1175/2010JCLI3731.1.

Frenger, I., N. Gruber, R. Knutti, and M. Münnich, 2013: Imprint of Southern Ocean eddies on winds, clouds and rainfall. *Nature Geoscience*, **6**, 608–612, doi:10.1038/ngeo1863.

Fu, L.-L., 1983: Recent progress in the application of satellite altimetry to observing the mesoscale variability and general circulation of the oceans. *Reviews of Geophysics*, **21(8)**, 1657–1666.

Fu, L. L., 2009: Pattern and velocity of propagation of the global ocean eddy variability. *Journal of Geophysical Research*, **114**, C11 017, doi:10.1029/2009JC005349.

Gascard, J.-C., and R. A. Clarke, 1983: The Formation of Labrador Sea Water. Part 2: Mesoscale and Smaller-Scale Processes. *Journal of Physical Oceanography*, **13**, 1779–1797.

Gaspar, P., Y. Grégoris, and J.-M. Lefevre, 1990: A simple eddy kinetic energy model for simulations of the oceanic vertical mixing: Tests at station Papa and long-term upper ocean study site. *Journal of Geophysical Research*, **95 (C9)**, 16 179–16 193.

Gelderloos, R., C. A. Katsman, and S. S. Drijfhout, 2011: Assessing the Roles of Three Eddy Types in Restratifying the Labrador Sea after Deep Convection. *Journal of Physical Oceanography*, **41**, 2102–2119, doi:10.1175/JPO-D-11-054.1.

Gent, P. R., and J. C. Mcwilliams, 1990: Isopycnal Mixing in Ocean Circulation Models. *Journal of Physical Oceanography*, **20**, 150–155.

Gill, A. E., 1982: *Atmosphere-Ocean Dynamics*. International Geophysics Series, Acadamic Press, New York.

Grégorio, S., T. Penduff, G. Sérazin, J.-M. Molines, B. Barnier, and J. Hirschi, 2015: Intrinsic Variability of the Atlantic Meridional Overturning Circulation at Interannual-to-Multidecadal Time Scales. *Journal of Physical Oceanography*, **45**, 1929–1946, doi:10.1175/JPO-D-14-0163.1.

Griffies, S. M., and R. W. Hallberg, 2000: Biharmonic Friction with a Smagorinsky-Like Viscosity for Use in Large-Scale Eddy-Permitting Ocean Models. *Monthly Weather Review*, **128**, 2935–2946.

Griffies, S. M., and Coauthors, 2009: Coordinated Ocean-ice Reference Experiments (COREs). *Ocean Modelling*, **26**, 1–46, doi:10.1016/j.ocemod.2008.08.007.

Hallberg, R., 2013: Using a resolution function to regulate parameterizations of oceanic mesoscale eddy effects. *Ocean Modelling*, **72**, 92–103, doi:10.1016/j.ocemod.2013.08.007.

Handmann, P., J. Fischer, M. Visbeck, J. Karstensen, A. Biastoch, C. Böning,

and L. Patara, 2018: The Deep Western Boundary Current in the Labrador Sea From Observations and a High-Resolution Model. *Journal of Geophysical Research: Oceans*, **123**, 2829–2850, doi:10.1002/2017JC013702.

Hátún, H., and L. Chafik, 2018: On the recent ambiguity of the North Atlantic subpolar gyre index. *Journal of Geophysical Research: Oceans*, **123**, doi:10.1029/2018JC014101.

Hátún, H., C. C. Eriksen, and P. B. Rhines, 2007: Buoyant Eddies Entering the Labrador Sea Observed with Gliders and Altimetry. *Journal of Physical Oceanography*, **37**, 2838–2854, doi:10.1175/2007JPO3567.1.

Henley, B. J., J. Gergis, D. J. Karoly, S. Power, J. Kennedy, and C. K. Folland, 2015: A Tripole Index for the Interdecadal Pacific Oscillation. *Climate Dynamics*, **45**, 3077–3090, doi:10.1007/s00382-015-2525-1.

Heywood, K. J., E. L. McDonagh, and M. A. White, 1994: Eddy kinetic energy of the North Atlantic subpolar gyre from satellite altimetry. *Journal of Geophysical Research*, **99**, 22 525–22 539.

Higgins, R. W., A. Leetmaa, and V. E. Kousky, 2002: Relationships between climate variability and winter temperature extremes in the United States. *Journal of Climate*, **15**, 1555–1572.

Holland, W. R., and L. B. Lin, 1975: On the Generation of Mesoscale Eddies and their Contribution to the Oceanic General Circulation. I. A Preliminary Numerical Experiment. *Journal of Physical Oceanography*, **5**, 642–657.

Holte, J., L. D. Talley, J. Gilson, and D. Roemmich, 2017: An Argo mixed layer climatology and database. *Geophysical Research Letters*, **44**, 5618–5626, doi:10.1002/2017GL073426.

Huffman, G. J., and Coauthors, 1997: The Global Precipitation Climatology Project (GPCP) Combined Precipitation Dataset. *Bulletin of the American Meteorological Society*, **78**, 5–20.

Ilıcak, M., 2016: Quantifying spatial distribution of spurious mixing in ocean models. *Ocean Modelling*, **108**, 30–38, doi:10.1016/j.ocemod.2016.11.002.

Jia, F., L. Wu, J. Lan, and B. Qiu, 2011a: Interannual modulation of eddy kinetic energy in the southeast Indian Ocean by Southern Annular Mode. *Journal of Geophysical Research: Oceans*, **116**, C02 029, doi:10.1029/2010JC006699.

Jia, F., L. Wu, and B. Qiu, 2011b: Seasonal Modulation of Eddy Kinetic Energy and Its Formation Mechanism in the Southeast Indian Ocean. *Journal of Physical Oceanography*, **41**, 657–665, doi:10.1175/2010JPO4436.1.

Jochum, M., G. Danabasoglu, M. Holland, Y. O. Kwon, and W. G. Large, 2008: Ocean viscosity and climate. *Journal of Geophysical Research: Oceans*, **113**, C06 017, doi:10.1029/2007JC004515.

Jones, H., and J. Marshall, 1997: Restratification after Deep Convection. *Journal of Physical Oceanography*, **27**, 2276–2287.

Josey, S. A., E. C. Kent, and P. K. Taylor, 1998: The Southampton Oceanography Centre (SOC) Ocean - Atmosphere heat, momentum and freshwater flux atlas. *Report of the Southampton Oceanography Centre*, **(6)**, 1–30.

Kalnay, E., M. Kanamitsu, R. Kistler, W. Collins, D. Deaven, and L. Gandin, 1996: The NCEP / NCAR 40-Year Reanalysis Project. *Bulletin of the American Meteorological Society*, **77**, 437–471.

Kang, D., and E. N. Curchitser, 2017: On the Evaluation of Seasonal Variability of the Ocean Kinetic Energy. *Journal of Physical Oceanography*, **47**, 1675–1683, doi: 10.1175/JPO-D-17-0063.1.

Katsman, C. A., M. A. Spall, and R. S. Pickart, 2004: Boundary Current Eddies and Their Role in the Restratification of the Labrador Sea. *Journal of Physical Oceanography*, **34**, 1967–1983.

Kirtman, B. P., and Coauthors, 2012: Impact of ocean model resolution on CCSM climate simulations. *Climate Dynamics*, **39**, 1303–1328, doi:10.1007/s00382-012-1500-3.

Kobashi, F., and A. Kubokawa, 2012: Review on North Pacific Subtropical Countercurrents and Subtropical Fronts: role of mode waters in ocean circulation and climate. *Journal of Oceanography*, **68**, 21–43, doi:10.1007/s10872-011-0083-7.

Large, W. G., G. Danabasoglu, J. C. McWilliams, P. R. Gent, and F. O. Bryan, 2001: Equatorial Circulation of a Global Ocean Climate Model with Anisotropic Horizontal Viscosity. *Journal of Physical Oceanography*, **31**, 518–536.

Large, W. G., and S. G. Yeager, 2004: Diurnal to decadal global forcing for ocean and sea–ice models: The data sets and flux climatologies. *NCAR Tech. Note NCAR/TN–460+STR*, 111pp.

Large, W. G., and S. G. Yeager, 2009: The global climatology of an interannually varying air-sea flux data set. *Climate Dynamics*, **33**, 341–364, doi:10.1007/s00382-008-0441-3.

Le Traon, P. Y., and R. Morrow, 2001: *Satellite Altimetry and Earth Sciences*, L.-L. Fu, and A. Cazenave, Eds., San Diego; London, chap. Ocean Currents and Eddies, 171–216.

Li, Z., 2012: Interannual and decadal variability of the subtropical mode water formation in the South Pacific Ocean. *Ocean Modelling*, **47**, 96–112, doi:10.1016/j.ocemod.2012.02.001.

Lilly, J. M., P. B. Rhines, F. Schott, K. Lavender, J. Lazier, U. Send, and E. D'Asaro, 2003: Observations of the Labrador Sea eddy field. *Progress in Oceanography*, **59**, 75–176, doi:10.1016/j.pocean.2003.08.013.

Liu, C., and L. Wu, 2012: An intensification trend of South Pacific Mode Water subduction rates over the 20th century. *Journal of Geophysical Research: Oceans*, **117**, C07 009, doi:10.1029/2011JC.

Locarnini, R. A., and Coauthors, 2013: *World Ocean Atlas 2013, Volume 1: Temperature*. NOAA Atlas NESDIS 73, 40 pp.

Lorbacher, K., J. Dengg, C. W. Böning, and A. Biastoch, 2010: Regional Patterns of Sea Level Change Related to Interannual Variability and Multidecadal Trends in the Atlantic Meridional Overturning Circulation. *Journal of Climate*, **23**, 4243–4254, doi:10.1175/2010JCLI3341.1.

Lozier, M. S., V. Roussenov, M. S. C. Reed, and R. G. Williams, 2010: Opposing decadal changes for the North Atlantic meridional overturning circulation. *Nature Geoscience*, **3**, 728–734, doi:10.1038/ngeo947.

Lübbecke, J. F., C. W. Böning, and A. Biastoch, 2008: Variability in the subtropical-tropical cells and its effect on near-surface temperature of the equatorial pacific: a model study. *Ocean Science*, **4**, 73–88.

Luo, H., A. Bracco, and E. Di Lorenzo, 2011: The interannual variability of the surface eddy kinetic energy in the Labrador Sea. *Progress in Oceanography*, **91**, 295–311, doi:10.1016/j.pocean.2011.01.006.

Madec, G., 2008: NEMO Ocean Engine. *Note du Pôle de modélisation, Institut Pierre-Simon Laplace (IPSL)*, **27**, ISSN No 1288–1619.

Madec, G., P. Delecluse, M. Imbard, and C. Lévy, 1998: OPA 8.1 Ocean General Circulation Model Reference Manual. *Notes du Pôle de Modélisation, Institut Pierre Simon Laplace*, **(11)**, 97pp.

Maltrud, M. E., and J. L. McClean, 2005: An eddy resolving global 1/10° ocean simulation. *Ocean Modelling*, **8**, 31–54, doi:10.1016/j.ocemod.2003.12.001.

Marshall, J., and F. Schott, 1999: Open-ocean convection: Observations, theory, and models. *Reviews of Geophysics*, **37**, 1–64, doi:10.1029/98RG02739.

Megann, A., 2018: Estimating the numerical diapycnal mixing in an eddy-permitting ocean model. *Ocean Modelling*, **121**, 19–33, doi:10.1016/j.ocemod.2017.11.001.

Menezes, V. V., H. E. Phillips, A. Schiller, N. L. Bindoff, C. M. Domingues, and M. L. Vianna, 2014: South Indian Countercurrent and associated fronts. *Journal of Geophysical Research: Oceans*, **119**, 6763–6791, doi:10.1002/2014JC010076.

Menezes, V. V., H. E. Phillips, M. L. Vianna, and N. L. Bindoff, 2016: Interannual variability of the South Indian Countercurrent. *Journal of Geophysical Research: Oceans*, **121**, doi:10.1002/2015JC011417.

Merle, J., H. Rotschi, and B. Voituriez, 1969: Zonal Circulation in the Tropical Western South Pacific at 170E. *Bulletin of the Japanese Society Fisheries Oceanography*, Special Issue (Prof. Uda's Commemorative Papers), 91–98.

Mertens, C., M. Rhein, M. Walter, C. W. Böning, E. Behrens, D. Kieke, R. Steinfeldt, and U. Stöber, 2014: Circulation and transports in the Newfoundland Basin, western subpolar North Atlantic. *Journal of Geophysical Research: Oceans*, **119**, 7772–7793, doi:10.1002/2014JC010019.

Mesinger, F., and A. Arakawa, 1976: Numerical Methods used in Climate Models. GARP Publication Series No. 17.

Minobe, S., A. Kuwano-Yoshida, N. Komori, S. P. Xie, and R. J. Small, 2008:

Influence of the Gulf Stream on the troposphere. *Nature*, **452**, 206–209, doi: 10.1038/nature06690.

MODE Group, 1978: The Mid-Oceans Dynamics Experiment. *Deep-Sea Research*, **25**, 859–910.

Morris, M., D. Roemmich, and B. Cornuelle, 1996: Observations of Variability in the South Pacific Subtropical Gyre. *Journal of Physical Oceanography*, **26**, 2359–2380.

Munk, W., 1950: On the wind-driven ocean circulation. *Journal of Meteorology*, **7**, 79–93.

Nishikawa, S., H. Tsujino, K. Sakamoto, and H. Nakano, 2010: Effects of Mesoscale Eddies on Subduction and Distribution of Subtropical Mode Water in an Eddy-Resolving OGCM of the Western North Pacific. *Journal of Physical Oceanography*, **40**, 1748–1765, doi:10.1175/2010JPO4261.1.

O'Kane, T. J., R. J. Matear, M. A. Chamberlain, J. S. Risbey, B. M. Sloyan, and I. Horenko, 2013: Decadal variability in an OGCM Southern Ocean: Intrinsic modes, forced modes and metastable states. *Ocean Modelling*, **69**, 1–21, doi: 10.1016/j.ocemod.2013.04.009.

Penduff, T., B. Barnier, W. K. Dewar, and J. J. O'Brien, 2004: Dynamical Response of the Oceanic Eddy Field to the North Atlantic Oscillation: A Model–Data Comparison. *Journal of Physical Oceanography*, **34**, 2615–2629, doi:10.1175/JPO2618.1.

Penduff, T., M. Juza, B. Barnier, J. Zika, W. K. Dewar, A.-M. Tréguier, J.-M. Molines, and N. Audiffren, 2011: Sea Level Expression of Intrinsic and Forced Ocean Variabilities at Interannual Time Scales. *Journal of Climate*, **24**, 5652–5670, doi: 10.1175/JCLI-D-11-00077.1.

Penduff, T., M. Juza, L. Brodeau, G. C. Smith, B. Barnier, J.-M. Molines, A.-M. Tréguier, and G. Madec, 2010: Impact of global ocean model resolution on sea-level variability with emphasis on interannual time scales. *Ocean Science*, **6**, 269–284, doi:10.5194/os-6-269-2010.

Qiu, B., 1999: Seasonal Eddy Field Modulation of the North Pacific Subtropical Countercurrent: TOPEX/Poseidon Observations and Theory. *Journal of Physical Oceanography*, **29**, 2471–2486.

Qiu, B., and S. Chen, 2004: Seasonal Modulations in the Eddy Field of the South Pacific Ocean. *Journal of Physical Oceanography*, **34**, 1515–1527.

Qiu, B., and S. Chen, 2006: Decadal Variability in the Large-Scale Sea Surface Height Field of the South Pacific Ocean: Observations and Causes. *Journal of Physical Oceanography*, **36**, 1751–1762, doi:10.1175/JPO2943.1.

Qiu, B., and S. Chen, 2010: Interannual Variability of the North Pacific Subtropical Countercurrent and Its Associated Mesoscale Eddy Field. *Journal of Physical Oceanography*, **40**, 213–225, doi:10.1175/2009JPO4285.1.

Qiu, B., S. Chen, and P. Hacker, 2007: Effect of Mesoscale Eddies on Subtropical Mode Water Variability from the Kuroshio Extension System Study (KESS). *Journal of Physical Oceanography*, **37**, 982–1000, doi:10.1175/JPO3097.1.

Radko, T., 2016: On the generation of large-scale eddy-driven patterns: The average eddy model. *Journal of Fluid Mechanics*, **809**, 316–344, doi:10.1017/jfm.2016.668.

Rattan, S., P. G. Myers, A.-M. Tréguier, S. Theetten, A. Biastoch, and C. Böning, 2010: Towards an understanding of Labrador Sea salinity drift in eddy-permitting simulations. *Ocean Modelling*, **35**, 77–88, doi:10.1016/j.ocemod.2010.06.007.

Rieck, J. K., C. W. Böning, and R. J. Greatbatch, 2018: Decadal Variability of Eddy Kinetic Energy in the South Pacific Subtropical Countercurrent in an Ocean General Circulation Model. *Journal of Physical Oceanography*, **48**, 757–771, doi:10.1175/JPO-D-17-0173.1.

Rieck, J. K., C. W. Böning, R. J. Greatbatch, and M. Scheinert, 2015: Seasonal variability of eddy kinetic energy in a global high-resolution ocean model. *Geophysical Research Letters*, **42**, doi:10.1002/2015GL066152.

Roemmich, D., J. Gilson, P. Sutton, and N. Zilberman, 2016: Multidecadal Change of the South Pacific Gyre Circulation. *Journal of Physical Oceanography*, **46**, 1871–1883, doi:10.1175/JPO-D-15-0237.1.

Rühs, S., K. Getzlaff, J. V. Durgadoo, A. Biastoch, and C. W. Böning, 2015: On the suitability of North Brazil Current transport estimates for monitoring basin-scale AMOC changes. *Geophysical Research Letters*, **42**, 8072–8080, doi:10.1002/2015GL065695.

Saenko, O. A., F. Dupont, D. Yang, P. G. Myers, I. Yashayaev, and G. C. Smith, 2014: Role of Resolved and Parameterized Eddies in the Labrador Sea Balance of Heat and Buoyancy. *Journal of Physical Oceanography*, **44**, 3008–3032, doi:10.1175/JPO-D-14-0041.1.

Sasaki, Y. N., S. Minobe, N. Schneider, T. Kagimoto, M. Nonaka, and H. Sasaki, 2008: Decadal Sea Level Variability in the South Pacific in a Global Eddy-Resolving Ocean Model Hindcast. *Journal of Physical Oceanography*, **38**, 1731–1747, doi:10.1175/2007JPO3915.1.

Sato, K., and T. Suga, 2009: Structure and Modification of the South Pacific Eastern Subtropical Mode Water. *Journal of Physical Oceanography*, **39**, 1700–1714, doi:10.1175/2008JPO3940.1.

Scharffenberg, M. G., and D. Stammer, 2010: Seasonal variations of the large-scale geostrophic flow field and eddy kinetic energy inferred from the TOPEX/Poseidon and Jason-1 tandem mission data. *Journal of Geophysical Research*, **115**, C02 008, doi:10.1029/2008JC005242.

Schubert, R., A. Biastoch, M. F. Cronin, and R. J. Greatbatch, 2018: Instability-Driven Benthic Storms Below the Separated Gulf Stream and the North Atlantic Current in a High-Resolution Ocean Model. *Journal of Physical Oceanography*, 2283–2303, doi:10.1175/JPO-D-17-0261.1.

Schütte, F., J. Karstensen, G. Krahmann, H. Hauss, B. Fiedler, P. Brandt, M. Visbeck, and A. Körtzinger, 2016: Characterization of "dead-zone" eddies in the eastern tropical North Atlantic. *Biogeosciences*, **13**, 5865–5881, doi:10.5194/bg-13-5865-2016.

Schwarzkopf, F. U., 2016: Ventilation pathways in the tropical Atlantic and Pacific Oceans with a focus on the Oxygen Minimum Zones: Development and application of a nested high-resolution global model system. Ph.D. Thesis, Christian-Albrechts-Universität zu Kiel, 259 pp., Kiel.

Scott, R. B., and F. Wang, 2005: Direct Evidence of an Oceanic Inverse Kinetic Energy Cascade from Satellite Altimetry. *Journal of Physical Oceanography*, **35**, 1650–1666, doi:10.1175/JPO2771.1.

Send, U., J. Marshall, U. Send, and J. Marshall, 1995: Integral Effects of Deep Convection. *Journal of Physical Oceanography*, **25**, 855–872.

Sérazin, G., B. Meyssignac, T. Penduff, L. Terray, B. Barnier, and J.-M. Molines, 2016: Quantifying uncertainties on regional sea level change induced by multidecadal intrinsic oceanic variability. *Geophysical Research Letters*, **43**, doi:10.1002/2016GL069273.

Sérazin, G., T. Penduff, S. Grégorio, B. Barnier, J.-M. Molines, and L. Terray, 2015: Intrinsic Variability of Sea Level from Global Ocean Simulations: Spatiotemporal Scales. *Journal of Climate*, **28**, 4279–4292, doi:10.1175/JCLI-D-14-00554.1.

Sérazin, G., and Coauthors, 2017: A global probabilistic study of the Ocean Heat Content low-frequency variability: atmospheric forcing versus oceanic chaos. *Geophysical Research Letters*, **44**, 5580–5589, doi:10.1002/2017GL073026.

Serreze, M. C., and C. M. Hurst, 2000: Representation of mean arctic precipitation from NCEP-NCAR and ERA reanalyses. *Journal of Climate*, **13**, 182–201.

Small, R. J., R. A. Tomas, and F. O. Bryan, 2014: Storm track response to ocean fronts in a global high-resolution climate model. *Climate Dynamics*, **43**, 805–828, doi:10.1007/s00382-013-1980-9.

Smith, R. D., M. E. Maltrud, F. O. Bryan, and M. W. Hecht, 2000: Numerical Simulation of the North Atlantic Ocean at 1/10°. *Journal of Physical Oceanography*, **30**, 1532–1561.

Spall, M. A., 2000: Generation of strong mesoscale eddies by weak ocean gyres. *Journal of Marine Research*, **58**, 97–116, doi:10.1357/002224000321511214.

Srokosz, M., M. Baringer, H. Bryden, S. Cunningham, T. Delworth, S. Lozier, J. Marotzke, and R. Sutton, 2012: Past, present, and future changes in the atlantic meridional overturning circulation. *Bulletin of the American Meteorological Society*, **93**, 1663–1676, doi:10.1175/BAMS-D-11-00151.1.

Stammer, D., and C. W. Böning, 1996: Generation and Distribution of Mesoscale Eddies in the North Atlantic Ocean. *The Warmwatersphere of the North Atlantic Ocean*, W. Krauss, Ed., Gebrüder Borntraeger, Berlin, Stuttgart, 159–193.

Stammer, D., C. Wunsch, and K. Ueyoshi, 2006: Temporal Changes in Ocean Eddy Transports. *Journal of Physical Oceanography*, **36**, 543–550, doi:10.1175/JPO2858.1.

Steele, M., R. Morley, and W. Ermold, 2001: PHC: A global ocean hydrography with a high quality Arctic Ocean. *Journal of Climate*, **14**, 2079–2087.

Taguchi, B., B. Qiu, M. Nonaka, H. Sasaki, S. P. Xie, and N. Schneider, 2010: Decadal variability of the Kuroshio Extension: mesoscale eddies and recirculations. *Ocean Dynamics*, **60**, 673–691, doi:10.1007/s10236-010-0295-1.

Travis, S., and B. Qiu, 2017: Decadal Variability in the South Pacific Subtropical Countercurrent and Regional Mesoscale Eddy Activity. *Journal of Physical Oceanography*, **47**, 499–512, doi:10.1175/JPO-D-16-0217.1.

Tsubouchi, T., T. Suga, and K. Hanawa, 2007: Three Types of South Pacific Subtropical Mode Waters: Their Relation to the Large-Scale Circulation of the South Pacific Subtropical Gyre and Their Temporal Variability. *Journal of Physical Oceanography*, **37**, 2478–2490, doi:10.1175/JPO3132.1.

Ummenhofer, C. C., F. U. Schwarzkopf, G. Meyers, E. Behrens, A. Biastoch, and C. W. Böning, 2013: Pacific Ocean Contribution to the Asymmetry in Eastern Indian Ocean Variability. *Journal of Climate*, **26**, 1152–1171, doi:10.1175/JCLI-D-11-00673.1.

van Sebille, E., J. Sprintall, F. U. Schwarzkopf, A. S. Gupta, A. Santoso, M. H. England, A. Biastoch, and C. W. Böning, 2014: Pacific-to-Indian Ocean connectivity: Tasman leakage, Indonesian Throughflow, and the role of ENSO. *Journal of Geophsical Research: Oceans*, **119**, 1365–1382, doi:doi:10.1002/2013JC009525.

Vancoppenolle, M., T. Fichefet, H. Goosse, S. Bouillon, G. Madec, and M. A. M. Maqueda, 2009: Simulating the mass balance and salinity of Arctic and Antarctic sea ice. 1. Model description and validation. *Ocean Modelling*, **27**, 33–53, doi:10.1016/j.ocemod.2008.10.005.

von Storch, J.-S., C. Eden, I. Fast, H. Haak, D. Hernández-Deckers, E. Maier-Reimer, J. Marotzke, and D. Stammer, 2012: An Estimate of the Lorenz Energy Cycle for the World Ocean Based on the 1/10° STORM/NCEP Simulation. *Journal of Physical Oceanography*, **42**, 2185–2205.

Wilson, C., C. W. Hughes, and J. R. Blundell, 2015: Forced and intrinsic variability in the response to increased wind stress of an idealized Southern Ocean. *Journal of Geophysical Research: Oceans*, **120**, 113–130, doi:10.1002/2014JC010315.

Wright, D. G., 1981: Baroclinic Instability in Drake Passage. *Journal of Physical Oceanography*, **11**, 231–246.

Wunsch, C., 1997: The Vertical Partition of Oceanic Horizontal Kinetic Energy. *Journal of Physical Oceanography*, **27**, 1770–1794.

Xie, P., and P. A. Arkin, 1996: Analyses of global monthly precipitation usin gauge observations, satellite estimates, and numerical model predictions. *Journal of Climate*, **9**, 840–858.

Xu, C., X.-D. Shang, and R. X. Huang, 2011: Estimate of eddy energy generation/dissipation rate in the world ocean from altimetry data. *Ocean Dynamics*, **61**, 525–541, doi:10.1007/s10236-011-0377-8.

Yamanaka, G., H. Tsujino, H. Nakano, and M. Hirabara, 2015: Decadal variability of the Pacific Subtropical Cells and its relevance to the sea surface height in the

western tropical Pacific during recent decades. *Journal of Geophysical Research: Oceans*, **120**, 201–224, doi:10.1002/2014JC010190.

Yang, D., 1999: An improved precipitation climatology for the Arctic Ocean. *Geophysical Research Letters*, **26**, 1625–1628.

Yang, Y., X. San Liang, B. Qiu, and S. Chen, 2017: On the Decadal Variability of the Eddy Kinetic Energy in the Kuroshio Extension. *Journal of Physical Oceanography*, **47**, 1169–1187, doi:10.1175/JPO-D-16-0201.1.

Zalesak, S. T., 1979: Fully multidimensional flux-corrected transport algorithms for fluids. *Journal of Computational Physics*, **31**, 335–362.

Zhai, X., and D. P. Marshall, 2013: Vertical Eddy Energy Fluxes in the North Atlantic Subtropical and Subpolar Gyres. *Journal of Physical Oceanography*, **43**, 95–103, doi:10.1175/JPO-D-12-021.1.

Zhang, W., and X.-H. Yan, 2014: Lateral Heat Exchange after the Labrador Sea Deep Convection in 2008. *Journal of Physical Oceanography*, **44**, 2991–3007, doi:10.1175/JPO-D-13-0198.1.

Zhang, W., and X.-H. Yan, 2018: Variability of the Labrador Sea Surface Eddy Kinetic Energy Observed by Altimeter From 1993 to 2012. *Journal of Geophysical Research: Oceans*, **123**, 601–612, doi:10.1002/2017JC013508.

Zhang, Y., 2004: Calculation of radiative fluxes from the surface to top of atmosphere based on ISCCP and other global data sets: Refinements of the radiative transfer model and the input data. *Journal of Geophysical Research*, **109**, D19 105, doi:10.1029/2003JD004457.

Zhu, J. S., E. Demirov, Y. Zhang, and A. Polomska-Harlick, 2014: Model simulations of mesoscale eddies and deep convection in the Labrador Sea. *Advances in Atmospheric Sciences*, **31**, 743–754, doi:DOI10.1007/s00376-013-3107-y.

Zweng, M., and Coauthors, 2013: *World Ocean Atlas 2013, Volume 2: Salinity*. NOAA Atlas NESDIS 74, 39 pp.

Author Contributions

The contributions to the manuscript *Rieck, J. K., C. W. Böning, and R. J. Greatbatch, 2018: Decadal Variability of Eddy Kinetic Energy in the South Pacific Subtropical Countercurrent in an Ocean General Circulation Model, Journal of Physical Oceanography, **48**, 757–771, doi:10.1175/JPO-D-17-0173.1.* presented in **section 4**:

- **Jan Klaus Rieck** contributed to the design of the study, performed all model simulations but the ones named CLIM and TROPAC01, performed the analysis, produced all figures and wrote the manuscript.
- **Claus W. Böning** contributed to the design of the study and commented on the manuscript.
- **Richard J. Greatbatch** contributed to the design of the study and commented on the manuscript.

The contributions to the manuscript *Rieck, J. K., C. W. Böning, and K. Getzlaff, 2019: The Nature of Eddy Kinetic Energy in the Labrador Sea: Different Types of Mesoscale Eddies, their Temporal Variability and Impact on Deep Convection, submitted to Journal of Physical Oceanography.* presented in **section 5**:

- **Jan Klaus Rieck** contributed to the design of the study, performed the analysis, produced all the figures and wrote the manuscript.
- **Claus W. Böning** contributed to the design of the study and commented on the manuscript.
- **Klaus Getzlaff** performed all simulations and commented on the manuscript.

Acknowledgments

First of all, I want to thank my supervisor Claus Böning for his continuous support and the many instructive sketches throughout the years. I also thank Klaus Getzlaff, Lavinia Patara and Franziska Schwarzkopf, as well as Markus Scheinert and Willi Rath for providing model output from their simulations and/or helping with technical issues with my own simulations and all the tools needed to get something useful out of them. Thanks to Richard Greatbatch for fruitful discussions and to the rest of TM (soon to be OD) for the many answered questions... and also for the posed ones! I thank B.R. and R.S. for checking on my skills in writing and explaining. I warmheartedly thank the people supporting me outside the work environment, getting my mind off the thesis – thanks to the Fjord.

Erklärung

Hiermit erkläre ich, dass ich die vorliegende Dissertation, abgesehen von der Beratung durch meinen Betreuer Prof. Dr. Claus Böning, selbstständig verfasst und keine anderen als die angegebenen Hilfsmittel verwendet habe. Beiträge anderer Wissenschaftler habe ich kenntlich gemacht. Diese Arbeit hat weder ganz noch in Teilen an einer anderen Stelle im Rahmen eines Prüfungsverfahrens vorgelegen. Ich erkläre, dass die vorliegende Arbeit gemäß der Grundsätze zur Sicherung guter wissenschaftlicher Praxis der Deutschen Forschungsgemeinschaft erstellt wurde. Desweiteren erkläre ich, dass mir kein akademischer Grad entzogen wurde.

Kiel, 2019

Jan Klaus Rieck